

Complex Berry phase and steady-state geometric amplification in non-Hermitian systems

: J.R. Lane¹†, C. Guria¹†, J. Höller², T.D. Montalvo¹, Y.S.S. Patil¹, J.G.E. Harris^{1,3,4*}

¹ Department of Physics, Yale University, New Haven, CT, USA

² Howard Hughes Medical Institute, Janelia Research Campus, Ashburn, VA, USA

³ Department of Applied Physics, Yale University, New Haven, CT, USA

⁴ Yale Quantum Institute, Yale University, New Haven, CT, USA

* Corresponding author. Email: jack.harris@yale.edu

† These authors contributed equally to this work.

Abstract

Understanding and controlling the dynamics of coupled oscillators is important for a wide range of scientific and technological endeavors. Two concepts that have generated new insights into this topic are Berry phase (oscillators' memory of how they have been tuned) and non-Hermiticity (damping and its often counter-intuitive consequences). Here we describe measurements of the interplay between these two phenomena that highlight the qualitative changes they induce in each other. In particular, non-Hermiticity changes the Berry phase from a real to a complex number, opening new avenues for controlling the flow of energy in oscillators. We illustrate this by demonstrating a broadly applicable means for converting a system's intrinsic damping into a novel form of amplification.

Geometric phase is a fundamental feature of classical and quantum oscillatory dynamics (1,2,3,4,5,6) and plays an important role in photonics (1,7,8), crystalline materials (9,10,11,12), quantum information (13,14), and many-body physics (15,16,17). Qualitatively, it can be viewed as an oscillating system’s “memory” of how its parameters have been varied. More precisely, geometric phase is defined when: (i) the system’s parameters are varied smoothly around a closed path (a loop) \mathcal{C} in the space of these parameters, and (ii) at the end of this variation the system’s state has changed by an overall phase factor $e^{-i\phi}$. Under these conditions, ϕ includes a contribution ϕ_B (known as the geometric or Berry phase (18)) that is determined solely by the shape of \mathcal{C} (i.e., it is independent of the duration of the traversal and the manner in which \mathcal{C} is traversed). This robust relationship – between the shape of a loop and the effect of transporting a system around it – arises in many physical settings (19,20).

These aspects of geometric phase are independent of whether or not the system includes loss. However, there are many dramatic differences between Hermitian systems (which do not include loss) and their non-Hermitian counterparts (which do). Notable examples include the topology of their spectra (21,22,23), their response to perturbations (24,25,26,27,28), and their performance in applications related to sensing and control (29,30,31).

The geometric phase is also expected to differ qualitatively between Hermitian and non-Hermitian systems. Perhaps the most striking difference is that the Hermitian ϕ_B is a real number, while the non-Hermitian ϕ_B is complex-valued (32). This is an important distinction, as the real ϕ_B only affects the oscillations’ phase, while the imaginary part of ϕ_B influences their magnitude. Thus, in addition to its interest as a fundamental aspect of the dynamics of coupled oscillators, access to non-Hermitian ϕ_B would open the possibility of developing novel geometric schemes to control the flow of energy in oscillator systems.

To date, most experiments on non-Hermitian systems have focused on their static properties (21,22,23,33,34), or on non-geometric features in the dynamics of the system’s energy (35,36,37). In contrast, phase evolution has been measured only in systems with access to a limited range of \mathcal{C} , which has precluded the observation of many non-Hermitian features of ϕ_B (38,39,40). Here, we present measurements of the complex-valued geometric phase in a non-Hermitian system with access to arbitrary \mathcal{C} . These measurements demonstrate a number of uniquely non-Hermitian features, including the (gauge-invariant) geometric gain for \mathcal{C} that are open paths (i.e., non-loops) (41), and the existence of an adiabatic limit for only one eigenmode (42,43).

We also demonstrate a highly counterintuitive result: that lossy linear elements can produce useful gain if their properties are modulated very slowly. This mechanism is fundamentally distinct from other forms of amplification, as it results specifically from the presence of loss in the system and from the geometric character of the dynamics. We show that this novel form of amplification does not require fine-tuning, and in fact is generic to non-Hermitian systems.

Experimental setup

In these measurements, the oscillators are two vibrational modes of a Si_3N_4 membrane ($500\ \mu\text{m} \times 500\ \mu\text{m} \times 150\ \text{nm}$) whose parameters can be tuned by laser light. As shown in Fig. 1A, the membrane is in an optical cavity (linewidth $\kappa/2\pi = 2.32\ \text{MHz}$) that is driven by a laser with wavelength $\lambda_{\text{opt}} = 1549.9\ \text{nm}$. The optomechanical interaction (44) between the

membrane and the cavity includes both radiation pressure and photothermal effects (45). The modes' bare eigenvalues (i.e., in the absence of any optomechanical effects) are $\lambda_1^{(0)}/2\pi = (2,423,969 - 1.8i)$ Hz and $\lambda_2^{(0)}/2\pi = (3,076,488 - 8.1i)$ Hz. Their radiation pressure and photothermal coupling rates ($g_{1,2}$ and $A_{1,2}$) are in Table S1.

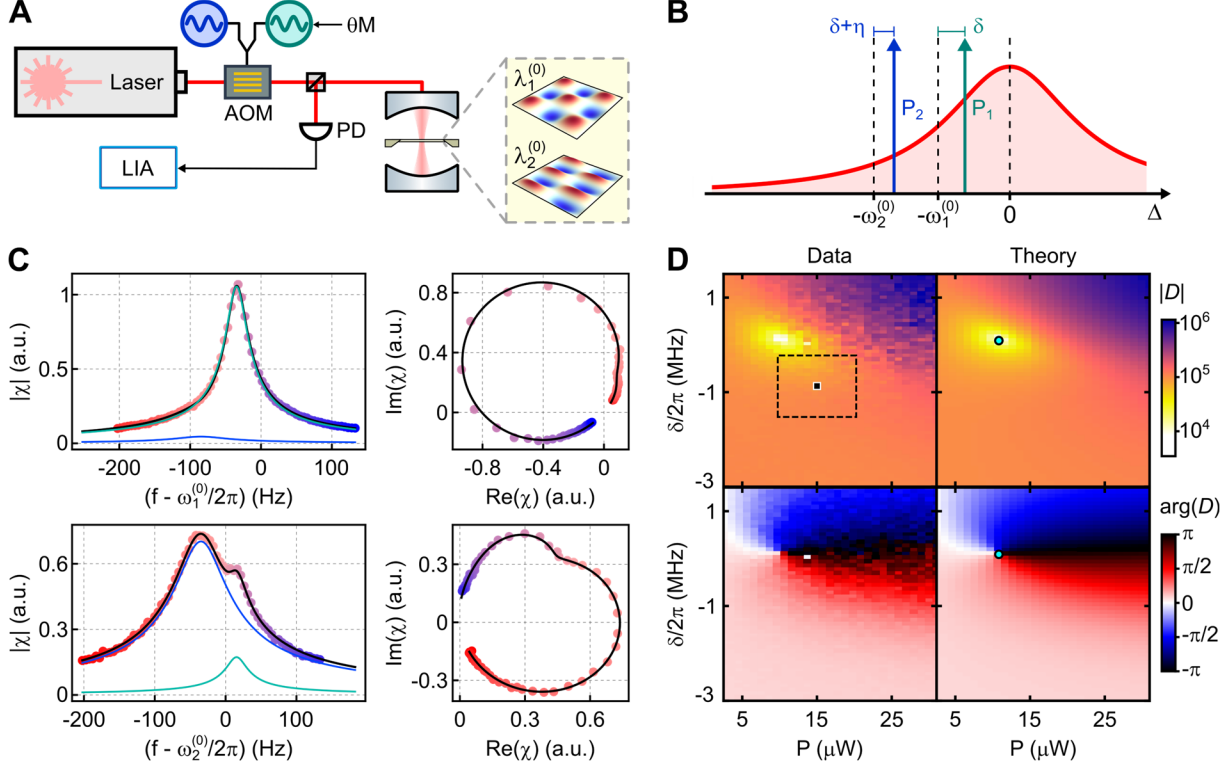


Fig. 1. Experimental setup and static characterization. (A) Gray: Si_3N_4 membrane and optical cavity mirrors. Yellow box: two vibrational modes of the membrane. These are tuned by laser tones from an acousto-optic modulator (AOM) driven by rf sources (blue and green). θM : phase modulation; PD: photodetector; LIA: lock-in amplifier. (B) Optical spectrum. Blue and green: control tones; red: cavity mode; P_i : power of i^{th} tone; δ : common detuning of the tones, η : detuning offset. (C) Mechanical susceptibility χ vs. frequency f for $P_{1,2} = P = 21.8 \mu\text{W}$, $\delta/2\pi = -1.2$ MHz. Left: $|\chi(f)|$ data (circles) and fit (black curve). Blue and green curves show the magnitude of each mode's contribution. Right: Parametric plot of $\chi(f)$ (circles: data, black curve: fit). Each data point's color indicates f . (D) $D(P, \delta)$. Left column: data. Right column: fit (45). Cyan circle: predicted location of an exceptional point (EP). Top row: $|D|$ (units: $(2\pi \times \text{Hz})^2$), bottom row: $\arg(D)$ (units: radians). Dashed box: the region over which ϕ_B is measured in Fig. 3. Black square: parameters used in Fig. 4. In (C) and (D), $\eta/2\pi = -50$ Hz.

The cavity is driven by two laser tones (Fig. 1B) with powers $P_{1,2}$ and detunings $\Delta_1 = -\omega_1^{(0)} + \delta$ and $\Delta_2 = -\omega_2^{(0)} + \delta + \eta$ where $\omega_{1,2}^{(0)} = \text{Re}(\lambda_{1,2}^{(0)})$. We set $|\eta|$ to a small value ($< 2\pi \times 100$ Hz) so that the frequency of these tones' beatnote $|\Delta_2 - \Delta_1| \approx |\omega_2^{(0)} - \omega_1^{(0)}|$. Qualitatively, this arrangement allows each laser tone to vary the mechanical modes' stiffness

and damping, while the intracavity beatnote provides tunable coupling between the modes (45,46,23).

In the standard description of cavity optomechanics (44,45), the time evolution of the mechanical system is governed by the equation of motion for two oscillators:

$$\dot{\vec{c}} = -iH\vec{c} \quad (1)$$

Here $\vec{c}(t) = (c_1(t), c_2(t))^T$ and the modes' amplitudes are $c_{1,2}$. The non-Hermitian 2×2 matrix H can be tuned via the control parameters $\vec{X} \equiv (P_1, P_2, \delta, \eta, \theta_{12})$ where θ_{12} is the phase of the intracavity beatnote. In a frame rotating with the beatnote, H depends on time only via $\vec{X}(t)$.

The membrane's motion is measured using standard heterodyne techniques which produce two signals $V_{1,2}(t) \propto c_{1,2}(t)$ (45). The mechanical modes are characterized by measuring their response to an oscillating force. Fig. 1C shows such a measurement for a typical choice of \vec{X} . The data is fit to determine $\lambda_{+,-}$ (the eigenvalues of H). Similar measurements and fits are made over a range of δ and $P_1 = P_2 = P$, and are converted to the discriminant $D = (\lambda_+ - \lambda_-)^2$ (Fig. 1D). Fitting this data to $D(\delta, P)$ as calculated from $H(\vec{X})$ (45) returns the values of $g_{1,2}$, $A_{1,2}$, and κ in Table S1.

Visualizing non-Hermitian control loops

In a Hermitian two-mode system, H can be represented as a three-vector \vec{B} (up to its trace) defined via $H = \vec{B} \cdot \vec{\sigma}$, where $\vec{\sigma}$ is the Pauli vector, and so control loops simply correspond to loops in \mathbb{R}^3 . This convenient picture can be extended to the non-Hermitian case by representing H as a pair of three-vectors: $H = (\vec{B}_{\text{re}} + i\vec{B}_{\text{im}}) \cdot \vec{\sigma}$. A non-Hermitian control loop then corresponds to $\vec{B}_{\text{re,im}}$ each tracing out a loop in \mathbb{R}^3 (Fig. 2A).

In our setup $\vec{B}_{\text{re,im}}$ are set by \vec{X} , and a loop \mathcal{C} is defined parametrically via $\vec{X}(s)$, where $0 \leq s \leq 1$ and $\vec{X}(0) = \vec{X}(1)$ (45). A traversal of \mathcal{C} is given by choosing a duration T and a function $s(t/T)$, with $s(0) = 0$ and $s(1) = 1$.

A particularly simple class of loops consists of holding P_1, P_2, δ, η constant while $\theta_{12} = 2\pi s$ and $s = t/T$ (this is a loop because θ_{12} is defined modulo 2π). Such a ‘‘simple’’ loop is illustrated in Fig. 2B. It consists of $\vec{B}_{\text{re,im}}$ rotating at a constant rate once around the z axis (45).

Measuring the geometric phase

In Hermitian systems, the adiabatic theorem ensures that condition (ii) is satisfied in the large- T limit for any loop \mathcal{C} for which the eigenvalues remain nondegenerate. However, in non-Hermitian systems the adiabatic theorem applies only to a state that is the least-damped eigenmode of H throughout \mathcal{C} (42,43). This requirement is met by all the \mathcal{C} used here.

To measure the geometric phase, we use the procedure sketched in Fig. 2C (the corresponding data is in Fig. 2D). In the first step, the membrane is driven at frequency $\omega_d \approx$

$\omega_1^{(0)}$ (or $\omega_2^{(0)}$) until it reaches its steady state $\vec{c}(0)$. Then the drive is turned off at $t = 0$. The membrane's subsequent motion is recorded and the data is fit (45) to determine $\vec{c}(0)$. In the second step, the membrane is initialized in the same way, but after the drive is turned off, a time-dependent phase shift is applied to one of the laser tones so that $\theta_{12}(t) = 2\pi t/T$, thereby meeting condition (i). For $t > T$, θ_{12} is held constant at 2π . The membrane's motion is recorded, and $\vec{c}(T)$ is determined by fitting the data (45) for $t > T$ (Fig. 2D).

If the initial state $\vec{c}(0)$ is the least-damped eigenmode of $H(0)$ (denoted as $\vec{\psi}_+$; the more-damped eigenmode is $\vec{\psi}_-$) then condition (ii) is met for large T . Specifically, in this case Eq. 1 predicts that $\vec{c}(T) = e^{-i\phi(T)}\vec{c}(0)$ with

$$\phi(T) = q_D T - \phi_B + q_1 T^{-1} + q_2 T^{-2} + \dots \quad (2)$$

where the q_i are complex constants (42,43,45). We refer to the first term $q_D T = \phi_D$ as the dynamical phase. For a simple loop $q_D = \lambda_+$ (the eigenvalue associated with $\vec{\psi}_+$); for a non-simple loop, q_D is the time-average of λ_+ . In practice, Eq. 2 is expected to hold when the adiabatic condition $T \gtrsim T_{\text{ad}}$ is satisfied, where T_{ad} equals the largest value of $|\lambda_+(s) - \lambda_-(s)|^{-1}$ along \mathcal{C} [42,47].

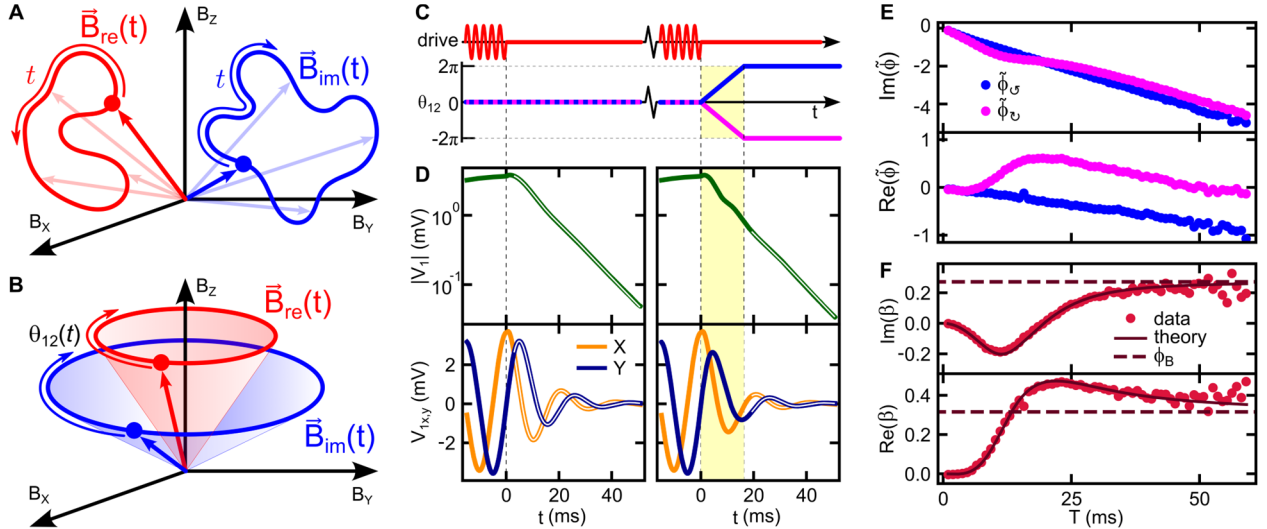


Fig. 2. Control loops and membrane dynamics. (A) A generic control loop. Circles: the start and stop of the loop (at $t = 0, T$); curves: $\vec{B}_{re,im}(t)$; arrows are a guide to the eye. (B) A “simple” control loop. (C) The timing of the experiment. Upper: the drive that initializes the membrane’s state. Lower: $\theta_{12}(t)$. In the first part of a measurement (left half), $\theta_{12} = 0$. In the second part (right half), θ_{12} is ramped to $+2\pi$ to traverse \mathcal{C}_\cup (blue) or to -2π to traverse \mathcal{C}_\cap (magenta). The loop duration ($0 < t < T$) is yellow. (D) The signal $V_1(t)$ produced by the membrane’s motion. Here $T = 16.3$ ms. White lines: fit to the evolution at constant H (45). V_1 reaches the measurement noise floor for $t > 50$ ms. (E) The complex phase $\tilde{\phi}(T)$ for \mathcal{C}_\cup (blue) and \mathcal{C}_\cap (magenta). The other elements of $U(T)$ are in Ref. (45). (F) $\beta(T)$. Solid line: theory; dashed line: predicted ϕ_B for \mathcal{C}_\cup (both without fit parameters). For (D) to (F), $P_{1,2} = P = 15 \mu W$, $\delta/2\pi = -1.0$ MHz, $\eta/2\pi = -50$ Hz.

To acquire a complete picture of the evolution resulting from a control loop, we measure the modes' propagator matrix $U(T)$ for the loop (45). We do this by performing the procedure in Fig. 2C twice: once each for two linearly independent choices of $\vec{c}(0)$. As shown in Ref. (45), when $U(T)$ is written in the basis of $(\vec{\psi}_+, \vec{\psi}_-)$, the matrix element $U_{++}(T)$ dominates at large T . If we define $U_{++}(T) = e^{-i\tilde{\Phi}(T)}$, then $\tilde{\Phi}(T)$ is expected to approach $\Phi(T)$ for large T (42,43).

Figure 2E shows $\text{Im}[\tilde{\Phi}(T)]$ and $\text{Re}[\tilde{\Phi}(T)]$ determined in this way. At large T , the amplitude of the motion decays roughly exponentially (Fig. 2E, upper panel) while its phase evolves roughly linearly (Fig. 2E, lower panel); this reflects the dominance of Φ_D in the large T limit of Eq. 2.

To isolate Φ_B , we also performed measurements that were identical except that $\theta_{12}(t) = -2\pi t/T$. Loosely speaking, this corresponds to traversing the same loop with the opposite sense; however, formally these loops are inequivalent, and we denote them as \mathcal{C}_\cup (for $\dot{\theta}_{12} > 0$) and \mathcal{C}_\cap (for $\dot{\theta}_{12} < 0$). The odd-order terms in Eq. 2 are expected to be identical for these two loops (e.g., $q_{D,\cup} = q_{D,\cap}$ and $q_{1,\cup} = q_{1,\cap}$), while the even-order terms are expected to differ by a sign (e.g., $\Phi_{B,\cup} = -\Phi_{B,\cap}$ and $q_{2,\cup} = -q_{2,\cap}$) (45). Consistent with this, measurements of $\tilde{\Phi}_\cup(T)$ and $\tilde{\Phi}_\cap(T)$ show similar trends at large T , but are clearly offset from each other (Fig. 2E).

This difference is quantified in Fig. 2F, which shows $\beta(T) = \frac{1}{2}(\tilde{\Phi}_\cap(T) - \tilde{\Phi}_\cup(T))$, which is expected to approach $\Phi_{B,\cup}$ for large T . Also shown are the no-free-parameter prediction for $\beta(T)$ and $\Phi_{B,\cup}$ (the geometric phase for \mathcal{C}_\cup) (45), which agree well with the data.

Varying the control loop

To demonstrate the geometric dependence of Φ_B , we alter \mathcal{C} by performing the same real-time variation of $\theta_{12}(t) = \pm 2\pi t/T$ as shown in Fig. 2C, but for different (P, δ) . This corresponds to loops as in Fig. 2B but with different $\vec{B}_{\text{re,im}}(0)$. Measurements of $\beta(T)$ are shown in Figs. 3, A and B, with each color corresponding to different (P, δ) . The no-free-parameter prediction of $\beta(T)$ and $\Phi_{B,\cup}$ are shown as solid lines and hollow stars.

While the data agree well with theory, the decay of the normal modes during the loop (Fig. 2D, top) places a practical upper limit on T (beyond which the membrane's motion is indistinguishable from measurement noise). Since the geometric phase corresponds to the $T \rightarrow \infty$ limit of $\beta(T)$, for each (P, δ) we fit the data at large T to the asymptotic form of Eq. 2: $\beta(T) = \Phi_{B,\cup} - q_{2,\cup}/T^2$ (45). The values of $\Phi_{B,\cup}$ (which we refer to as Φ_B from here on) returned by these fits are the solid stars in Fig. 3, A and B.

Figure 3C shows the results of a similar analysis over a wider range of (P, δ) . The left-hand panels show $\text{Re}(\Phi_B)$ and $\text{Im}(\Phi_B)$ determined by fitting $\beta(T)$ for large T as just described. The right-hand panels show the no-free-parameter prediction for $\text{Re}(\Phi_B)$ and $\text{Im}(\Phi_B)$ calculated from P, δ and the quantities in Table S1.

The geometric character of Φ_B is also evident in measurements using more complicated control loops. These include \mathcal{C} in which P_2, δ , and θ_{12} are all varied (corresponding to generic loops as in Fig. 2A), and \mathcal{C} that are traversed with $\theta_{12}(t)$ that are nonlinear in t . These are presented in (45), (along with measurements using different values of η and different normal modes of the membrane), and show good agreement with the no-free-parameters calculation over

the full range of T . In particular, they show that $\beta(T)$ approaches the predicted ϕ_B at large T .

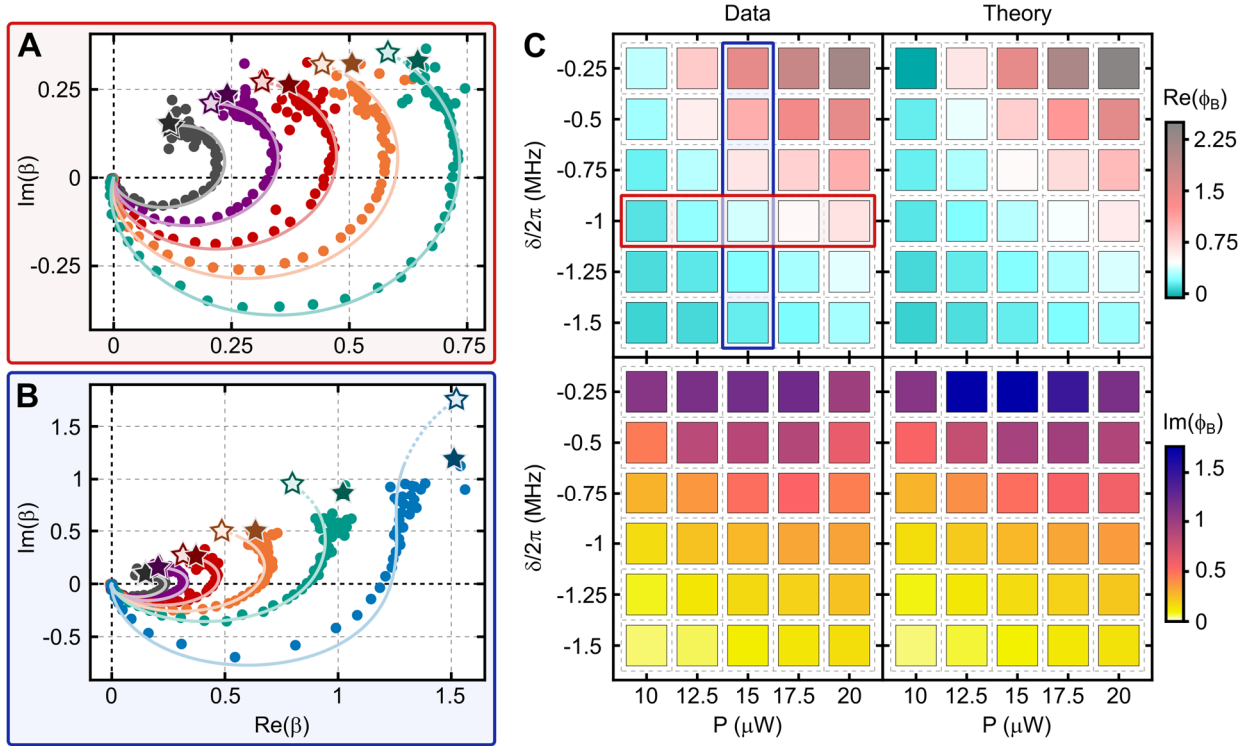


Fig. 3. Measurements of the complex geometric phase. (A) Parametric plots of $\beta(T)$. Data nearest the origin corresponds to $T = 0$. Here $\delta/2\pi = -1$ MHz and $P_{1,2} = P = (10, 12.5, 15, 17.5, 20) \mu\text{W}$ (gray, purple, red, orange, teal). Solid line: predicted $\beta(T)$. Hollow star: predicted ϕ_B . Solid star: measured ϕ_B . (B) As in (A), but with $P_{1,2} = P = 15 \mu\text{W}$ and $\delta/2\pi = (-1.5, -1.25, -1, -0.75, -0.5, -0.25)$ MHz (gray, purple, red, orange, teal, blue). (C) The value of ϕ_B from measurements as in (A) and (B) for a range of (P, δ) . Data in the red (blue) box corresponds to measurements in (A) ([B]). For all measurements, $\eta/2\pi = -50$ Hz.

Imaginary geometric phase on open paths

The phase of an oscillator is only defined relative to a reference or gauge, which may vary within the space of control parameters. As a result, the accumulated phase has a gauge-invariant definition only if \mathcal{C} is a loop. In contrast, an oscillator's amplitude does not depend on a gauge choice, and so $\text{Im}(\phi_B)$ is well-defined even if \mathcal{C} is not a loop (41,45).

Figure 4 shows measurements of $\text{Im}(\phi_B)$ for a family of paths, some of which are not loops. They are realized by fixing P and δ , and ramping θ_{12} from 0 to $\pm(N/5)2\pi t/T$ for $N = 0, 1, 2, 3, 4, 5$ (Fig. 4A), resulting in non-loop paths for $1 \leq N \leq 4$. Fig. 4B shows $\text{Im}(\beta(T))$ for each N (data and theory) and Fig. 4C shows $\text{Im}(\phi_B)$ determined by fitting $\beta(T)$ as described previously.

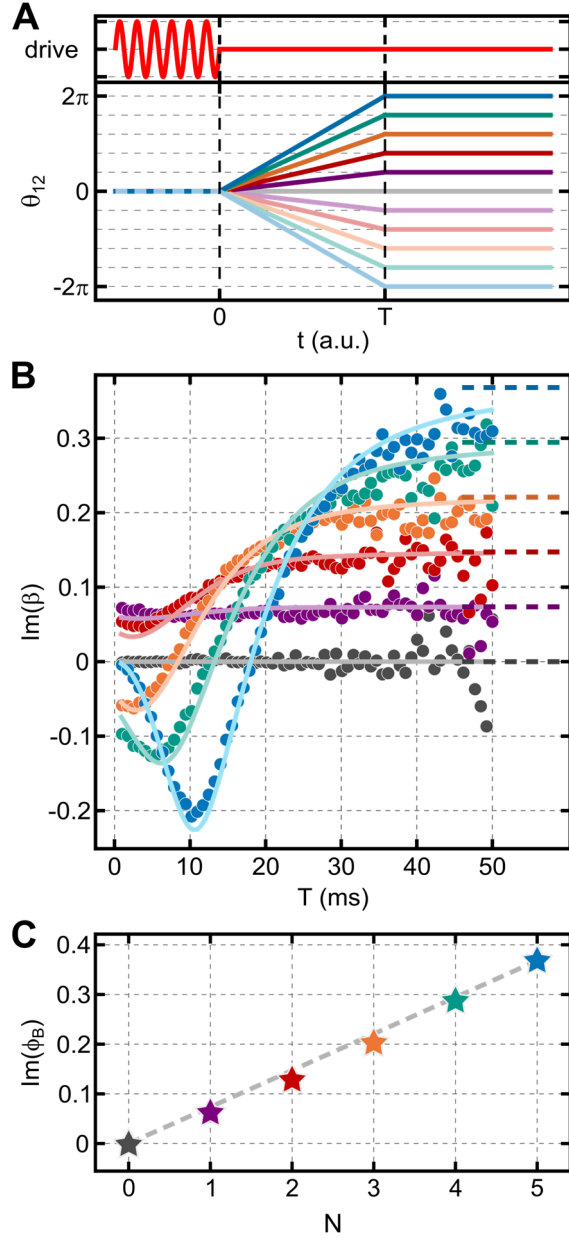


Fig. 4. Imaginary geometric phase on open paths. (A) Control paths in which θ_{12} is ramped from 0 to $\pm(N/5)2\pi$, for $N = 0, 1, 2, 3, 4, 5$ (gray, purple, red, orange, teal, blue). Here $P_{1,2} = P = 15 \mu W$, $\delta/2\pi = -0.87$ MHz and $\eta/2\pi = -50$ Hz. Solid (pale) lines correspond to positive (negative) $\dot{\theta}_{12}$. (B) $\text{Im}(\beta(T))$ as measured (circles) and predicted (curves) for each N . Dashed lines: predicted $\text{Im}(\phi_B)$ for each N . (C) Stars: measured $\text{Im}(\phi_B)$; Line: predicted $\text{Im}(\phi_B)$.

Steady-state geometric gain

For a loop with $\text{Im}(\phi_B) < 0$, the geometric phase contributes gain to the normal mode. In the measurements described so far, this geometric gain is overwhelmed by the mode's intrinsic damping. This is evident in Fig. 2E (top panel, magenta), where the amplitude of motion always decreases during \mathcal{C}_ν loops, even though $\text{Im}(\phi_{B,\nu}) < 0$.

In contrast, the amplitude of motion should actually increase if the loop's geometric gain exceeds the dynamical loss (i.e. $\text{Im}(\phi_B) < \text{Im}(\phi_D) < 0$). For any given \mathcal{C} , it is impossible to meet this condition in the large- T limit, as $\text{Im}(\phi_B) \propto T^0$ while $\text{Im}(\phi_D) \propto T^1$ (Eq. 2). However, we have found that for any given T , it is possible to find \mathcal{C} such that the geometric gain amplifies the normal mode's motion regardless of how large T is.

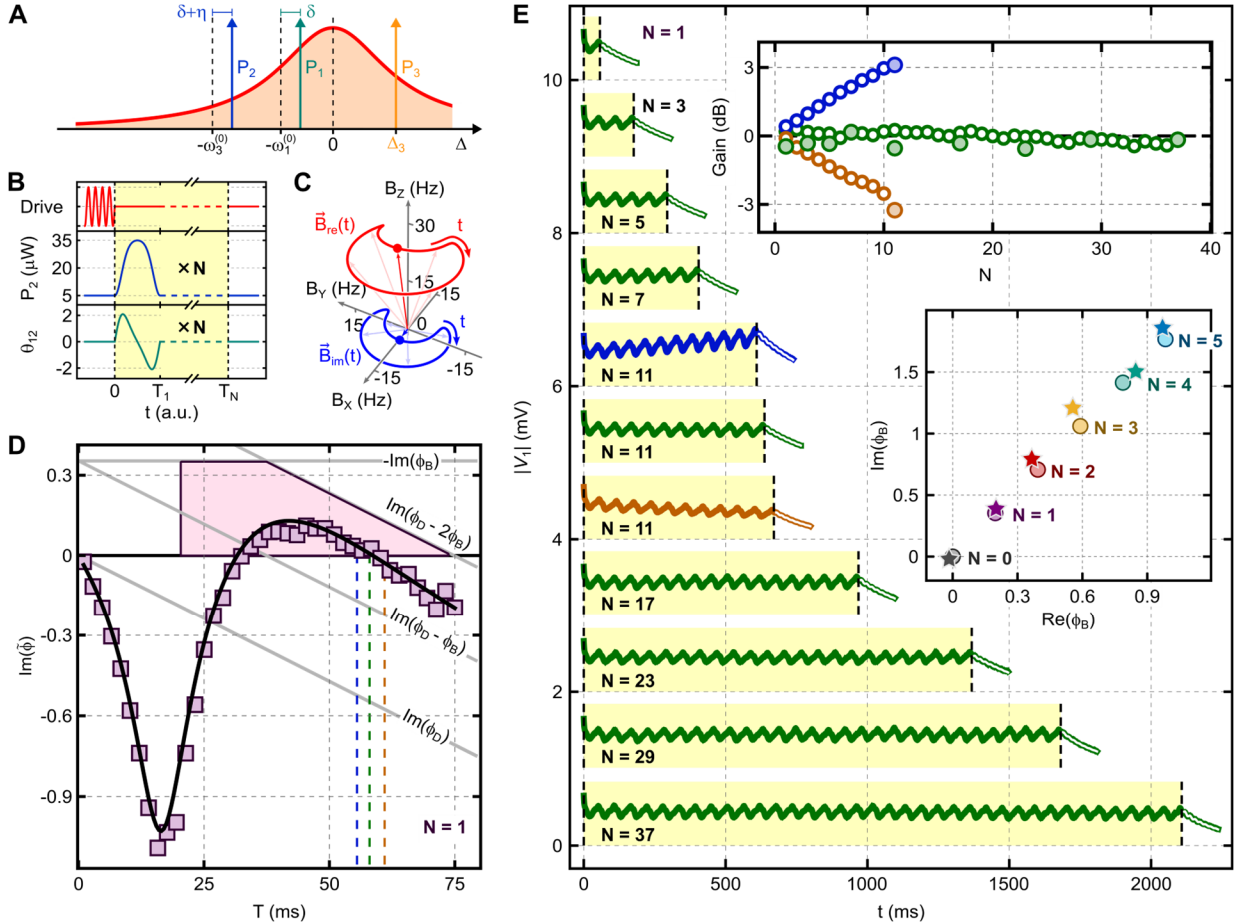


Fig. 5. Steady-state geometric gain. (A) The control tones. (B) $P_2(t)$ and $\theta_{12}(t)$ during a loop $\mathcal{C}_{\text{amp}}^{(N)}$. (C) The loop $\mathcal{C}_{\text{amp}}^{(1)}$ visualized as $\vec{B}_{\text{re,im}}(t)$. (D) The normal mode's gain $\text{Im}[\tilde{\phi}]$ when $\mathcal{C}_{\text{amp}}^{(1)}$ is traversed once in time T . Squares: data; black curve: theory. Pink: the region Γ that results in SSGG. Blue, green, orange lines: values of T used in (E). (E) Green: the amplitude of the membrane's motion during loops $\mathcal{C}_{\text{amp}}^{(N)}$ for $T = 58$ ms; blue and orange: the same, but for $T = 55.5$ ms (blue) and $T = 61$ ms (orange). Each curve is offset by 1 mV, so that $|V_1| = 0$ corresponds to the bottom of the yellow band. White curves: fit to the evolution at constant H after $\mathcal{C}_{\text{amp}}^{(N)}$ ends. Upper inset: a summary of the gain resulting from these loops. Filled circles: the gain from each $\mathcal{C}_{\text{amp}}^{(N)}$ in the main panel; green hollow circles: the gain after each circuit of the $N = 37$ loop; blue and orange hollow circles: the same, but for the $N = 11$ loop with $T_1 = 55.5$ ms (blue) and $T = 61$ ms (orange). For (D) and (E), $P_1 = 26 \mu\text{W}$, $P_3 = 28 \mu\text{W}$, $\Delta_3/2\pi = 3.38$ MHz, $\delta/2\pi = -0.911$ MHz, $\eta/2\pi = -50$ Hz. Lower inset: predicted ϕ_B (circles); measured ϕ_B (stars) for $\mathcal{C}_{\text{amp}}^{(N)}$.

To demonstrate this, we use the same measurement sequence (Fig. 2C) and setup (Fig. 1A), except that the $\lambda_2^{(0)}$ mechanical mode is replaced by a mode with bare resonance frequency $\lambda_3^{(0)}/2\pi = (3,331,064 - 1.92 i)$ Hz (see Table S1 for its parameters). In addition, a third laser tone is added (Fig. 5A) to allow access to a greater range of $\vec{B}_{\text{re,im}}(t)$.

The system is varied around a loop \mathcal{C}_{amp} in which P_2 and θ_{12} are varied as shown in Fig. 5 B and C while all the other parameters are fixed. Figure 5D shows the gain of the normal mode when it is transported around \mathcal{C}_{amp} in time T . Despite the loss contributed by $\text{Im}(\phi_D)$ (the gray line), the gain is positive for $32 \text{ ms} < T < 58 \text{ ms}$.

As expected, the dynamical loss dominates for large T (resulting in net loss for $T > 58$ ms). However, it is possible to achieve net gain at arbitrarily large times (i.e., in the steady state) simply by repeating the loop. This is demonstrated in Fig. 5E, which shows the mode’s amplitude of motion while \mathcal{C}_{amp} is repeated up to $N = 37$ times (total duration > 2 s). The amplitude varies slightly during each repetition, but always returns to its initial value. This “break-even” condition occurs because the duration of each repetition ($T = 58$ ms) provides near-exact balance between the dynamical loss and the gain that results from traversing \mathcal{C}_{amp} (Fig. 5D, green dashed line). If a slightly different value of T is chosen, each repetition of \mathcal{C}_{amp} results in positive (or negative) gain, and the mode’s motion grows (or shrinks) accordingly. This is shown by the blue and orange data in Fig. 5E.

The steady-state geometric gain (SSGG) demonstrated in Fig. 5E does not contradict the prediction that dynamical phase should dominate at large T . This is because Eq. 2 applies to any given loop \mathcal{C} , while each sequence used in Fig. 5E (i.e., each choice of N) formally corresponds to a distinct loop. If we denote these loops by $\mathcal{C}_{\text{amp}}^{(N)}$ (with $\mathcal{C}_{\text{amp}}^{(1)} = \mathcal{C}_{\text{amp}}$), then SSGG results from traversing $\mathcal{C}_{\text{amp}}^{(N)}$ in time $T_N = NT$, with T chosen so that $\mathcal{C}_{\text{amp}}^{(1)}$ has net gain ($\text{Im}[\tilde{\phi}(T)] > 0$) and with no limit on how large N may be.

Lastly, we note that the membrane’s motion remains phase-coherent throughout the operations used in Fig. 5D and E. This is demonstrated in the lower inset of Fig. 5E, which compares the geometric phase measured for $\mathcal{C}_{\text{amp}}^{(N)}$ with $N\phi_{\text{B,amp}}$ where $\phi_{\text{B,amp}}$ is the predicted geometric phase for \mathcal{C}_{amp} .

Discussion

We emphasize that the results presented here are not limited to cavity optomechanics, but rather are generic features of the non-Hermitian geometric phase, and can be realized in any physical system governed by Eq. 1. To illustrate this broad applicability, we present a platform-agnostic description of SSGG, the class of control loops that produce it, and a measure of how common such loops are.

The key feature of SSGG is that an excitation in a lossy mode grows in amplitude as a result of the geometric phase, and that the rate of this growth is maintained indefinitely (48). If we consider a loop \mathcal{C} that is repeatedly traversed, with each traversal using the same time-dependence $s(t/T)$ and duration T , then SSGG occurs when four conditions are met: (a) adiabaticity is relevant (i.e., Eq. 2 applies); (b) the gain at the end of the loop is positive; (c) the gain would be negative without the contribution from ϕ_B ; and (d) ϕ_B accounts for the majority

of the difference between the dynamical loss and the measured gain. This last condition ensures that the gain is not attributable to higher-order terms [$\mathcal{O}(T^{-1})$] in Eq. 2. When these conditions are met, repeating the loop will result in SSGG (as in Fig. 5E).

Conditions (a) through (d) can be represented by the inequalities $T > T_{\text{ad}}$ and $0 < \text{Im}[\tilde{\phi}(T)] < \{-\text{Im}[\phi_B], \text{Im}[\phi_D] - 2\text{Im}[\phi_B]\}$. For a given \mathcal{C} and s , these inequalities define a region Γ in the plane of T and $\text{Im}[\tilde{\phi}]$ (Fig. 5D) with a simple interpretation: if $\text{Im}[\tilde{\phi}(T)]$ passes through Γ , then \mathcal{C} and s can produce SSGG. Specifically, choosing T such that $\text{Im}[\tilde{\phi}(T)]$ lies within Γ ensures that conditions (a – d) are met.

A convenient measure of how common these loops are could be provided if, for example, loops satisfying (a – d) were distinguished by some simple feature. Lacking such a proxy, we can instead consider families of \mathcal{C} and s that are parameterized by a few variables. As described in Ref. (45), this approach shows that a wide range of “simple” loops (as in Fig. 2B) produce SSGG, as do loops with more complicated shapes.

Thus, SSGG is a broadly applicable scheme for realizing an amplifier that differs from other amplifiers in its underlying principle and in its practical aspects. It arises only if the geometric phase is complex, which occurs only if there is loss in the system. As a result, SSGG can be viewed as the direct conversion of a system’s loss into gain (via the slow modulation of its parameters). This is distinct from other amplifiers, in which the gain mechanism may overcome the system’s intrinsic loss, but does not require loss for its operation.

To give a specific comparison, we note that conventional parametric amplification (PA) and SSGG both add gain to a mode by modulating the system’s parameters (49). However, as a practical matter, the modulation frequency required for SSGG is lower than that of PA by a factor $\sim Q$, the mode’s quality factor. This is because the typical modulation rate required for SSGG is $\sim \gamma$ (the mode’s intrinsic decay rate) (50), while PA operates by non-adiabatically modulating parameters at rates comparable to the mode’s oscillation frequency. In addition to this important practical difference, these schemes differ fundamentally, as PA does not involve either geometric phase or non-Hermiticity.

The work presented here opens a route to exploring other non-Hermitian aspects of geometric phase, such as cases in which ϕ_B is set by the topology of \mathcal{C} , rather than its shape. Such topological phases are predicted to occur when the system’s eigenvectors are degenerate throughout \mathcal{C} (43); in the present system this can be realized by choosing (P, δ) corresponding to an exceptional point (EP; one is indicated in Fig. 1D) and then ramping θ_{12} by $2N\pi$ (for integer N). In this case, ϕ_B is predicted to be determined by the loop’s homotopy class within the topologically nontrivial space of EPs (43). Topological ϕ_B is also predicted for \mathcal{C} that encircles an EP an even number of times (21). Such loops cannot be carried out adiabatically, as they necessarily cause eigenmodes to swap between least-damped and most-damped. However, they may be realized using more sophisticated control schemes (51,52) that are inspired by Hermitian shortcuts-to-adiabaticity (53).

Acknowledgments

We acknowledge helpful discussions with C. D. Brown, V. Chavva, S. M. Girvin, J. Kim, K. W. Lehnert, K. Murch, A. Neely, A. J. Pillai, N. Read, H. Ribeiro, C. C. Wilson, and Y. Zhang. This work was supported by the Air Force Office of Scientific Research (grant FA9550-21-1-0152), the Vannevar Bush Faculty Fellowship (N00014-20-1-2628), the Air Force Office of Scientific Research Multidisciplinary University Research Initiative (FA9550-21-1-0202), and the Yale Mossman Prize Fellowship in Physics.

References and Notes

1. S. Pancharatnam, Generalized theory of interference, and its applications. *Proceedings of the Indian Academy of Science A* **44**, 247 – 262 (1956).
2. M. V. Berry, Quantal phase factors accompanying adiabatic changes. *Proceedings of the Royal Society of London Series A* **392**, 45 – 57 (1984).
3. B. Simon, Holonomy, the Quantum Adiabatic Theorem, and Berry's Phase. *Physical Review Letters* **51**, 2167 – 2170 (1984).
4. J. Hannay, Angle variable holonomy in adiabatic excursion of an integrable Hamiltonian. *Journal of Physics A* **18**, 221–30 (1985).
5. F. Wilczek, A. Zee, Appearance of gauge structure in simple dynamical systems. *Physical Review Letters* **52**, 2111 – 2114 (1984).
6. Y. Aharonov, J. Anandan, Phase change during a cyclic quantum evolution. *Physical Review Letters* **58**, 1593 (1987).
7. R. Y. Chiao, Y.-S. Wu, Manifestations of Berry's Topological Phase for the Photon. *Physical Review Letters* **57**, 933 – 936 (1986).
8. C. P. Jisha, S. Nolte, A. Alberucci, Geometric phase in optics: from wavefront manipulation to waveguiding. *Laser and Photonics Reviews* **15**, 2100003 (2021).
9. R. Resta, Macroscopic polarization in crystalline dielectrics: the geometric phase approach. *Review of Modern Physics* **66**, 899 – 915 (1994).
10. M. Z. Hasan, C. L. Kane. Colloquium: Topological insulators. *Review of Modern Physics* **82**, 3045–3067 (2010).
11. X.-L. Qi, S.-C. Zhang, Topological insulators and superconductors. *Review of Modern Physics* **83**, 1057–1110 (2011).
12. D. Xiao, M.-C. Chang, Q. Niu, Berry phase effects on electronic properties. *Review of Modern Physics* **82**, 1959–2007 (2010).
13. P. Zinardi, M. Rasetti, Holonomic quantum computation. *Physics Letters A* **264**, 94 – 99 (1999).

-
14. E. Sjöqvist, D. M. Tong, L. Mauritz Andersson, B. Hessmo, M. Johansson, K. Singh. Non-adiabatic holonomic quantum computation. *New Journal of Physics* **14**, 103035 (2012).
 15. D. Arovas, J. Schrieffer, F. Wilczek, Fractional statistics and the quantum Hall effect. *Physical Review Letters* **53**, 722 – 723 (1984).
 16. G. Moore and N. Read, Nonabelions in the fractional quantum hall effect. *Nuclear Physics B* **360**, 362 – 396 (1991).
 17. V. Gritsev, A. Polkovnikov, Dynamical quantum Hall effect in the parameter space. *Proceedings of the National Academy of Science* **109**, 6457 – 6462 (2012).
 18. M. V. Berry, Geometric Phase Memories. *Nature Physics* **6**, 148 – 150 (2010).
 19. F. Wilczek, A. Shapere, Eds., *Geometric Phases in Physics* (World Scientific, 1989).
 20. E. Cohen, H. Larocque, F. Bouchard, F. Nejdassattari, Y. Gefen, E. Karimi, *Nature Reviews Physics* **1**, 437 – 449 (2019).
 21. O. Latinne, N. J. Kylstra, M. Dörr, J. Purvis, M. Terao-Dunseath, C. J. Joachain, P. G. Burke, C. J. Noble, Laser-Induced Degeneracies Involving Autoionizing States in Complex Atoms. *Physical Review Letters* **74**, 46 (1995).
 22. C. Dembowski, H.-D. Gräf, H. L. Harney, A. Heine, W. D. Heiss, H. Rehfeld, A. Richter, Experimental Observation of the Topological Structure of Exceptional Points. *Physical Review Letters* **86**, 787 – 790 (2001).
 23. Y.S.S. Patil, J. Höller, P.A. Henry, C. Guria, Y. Zhang, L. Jiang, N. Kralj, N. Read, J.G.E. Harris, Measuring the knot of non-Hermitian degeneracies and non-commuting braids. *Nature* **607**, 271–275 (2022).
 24. T. E. Lee, Anomalous Edge State in a Non-Hermitian Lattice. *Physical Review Letters* **116**, 133903 (2016).
 25. V. M. Martinez Alvarez, J. E. Barrios Vargas, L. E. F. Foa Torres, Non-Hermitian robust edge states in one dimension: Anomalous localization and eigenspace condensation at exceptional points. *Physical Review Letters* **97**, 121401(R) (2018).
 26. F. K. Kunst, E. Edvardsson, J. C. Budich, E. J. Bergholtz, Biorthogonal Bulk-Boundary Correspondence in Non-Hermitian Systems. *Physical Review Letters* **121**, 026808 (2018).
 27. S. Yao, Z. Wang, Edge States and Topological Invariants of Non-Hermitian Systems. *Physical Review Letters* **121**, 086803 (2018).
 28. A. Hashemi, K. Busch, D. N. Christodoulides, S. K. Ozdemir, R. El-Ganainy, Linear response theory of open systems with exceptional points. *Nature Communications* **13**, 3281 (2022).
 29. H.-K. Lau, A. A. Clerk, Fundamental limits and non-reciprocal approaches in non-Hermitian quantum sensing. *Nature Communications* **9**, 4320 (2018).

-
30. J. Wiersig, Review of exceptional point-based sensors. *Photonics Research* **8**, 1457 – 1467 (2020).
 31. C. Wang, W. R. Sweeney, A. D. Stone, L. Yang, Coherent perfect absorption at an exceptional point. *Science* **373**, 1261–1265 (2021).
 32. J. C. Garrison, E. M. Wright, Complex geometrical phases for dissipative systems. *Physics Letters A* **128**, 177 – 181 (1988).
 33. C. E. Rüter, K. G. Makris, R. El-Ganainy, D. N. Christodoulides, M. Segev, D. Kip, Observation of parity–time symmetry in optics. *Nature Physics* **6**, 192 – 195 (2010).
 34. B. Dietz, H. L. Harney, O. N. Kirillov, M. Miski-Oglu, A. Richter, and F. Schäfer, Exceptional Points in a Microwave Billiard with Time-Reversal Invariance Violation. *Physical Review Letters* **106**, 150403 (2011).
 35. H. Xu, D. Mason, Luyao Jiang, J. G. E. Harris, Topological energy transfer in an optomechanical system with an exceptional point, *Nature* **537**, 80 – 83 (2016).
 36. J. Doppler, A. Mailybaev, J. Böhm, U. Kuhl, A. Girschik, F. Libisch, T.J. Milburn, P. Rabl, N. Moiseyev, S. Rotter, Dynamically encircling an exceptional point for asymmetric mode switching. *Nature* **537** 76 – 79 (2016).
 37. Y. Choi, J. W. Yoon, J. K. Hong, Y. Ryu, S. H. Song, Direct observation of time-asymmetric breakdown of the standard adiabaticity around an exceptional point. *Communications Physics* **3**, 140 (2020).
 38. W. Chen, M. Abbasi, Y. N. Joglekar, K. W. Murch, Quantum Jumps in the Non-Hermitian Dynamics of a Superconducting Qubit. *Physical Review Letters* **127**, 140504 (2021).
 39. Y. Singhal, E. Martello, S. Agrawal, T. Ozawa, H. Price, B. Gadway, Measuring the adiabatic non-Hermitian Berry phase in feedback-coupled oscillators. *Physical Review Research* **5**, L032026 (2023).
 40. M. Abbasi, W. Chen, M. Naghiloo, Y. N. Joglekar, K. W. Murch, Topological Quantum State Control through Exceptional-Point Proximity. *Physical Review Letters* **128**, 160401 (2022).
 41. S. Massar, Applications of the complex geometric phase for metastable systems, *Physical Review A* **54**, 4770 (1996).
 42. G. Nenciu, G. Rasche, On the adiabatic theorem for nonself-adjoint Hamiltonians. *Journal of Physics A* **25**, 5741 – 5751 (1992).
 43. J. Höller, N. Read, J.G.E. Harris, Non-Hermitian adiabatic transport in the space of exceptional points. *Physical Review A* **102**, 032216 (2020).
 44. M. Aspelmeyer, T. J. Kippenberg, F. Marquardt, Cavity optomechanics. *Reviews of Modern Physics* **86**, 1391 – 1452 (2014).
 45. Materials and methods are available as supplementary materials.

-
46. L. F. Buchmann, D.M. Stamper-Kurn, Nondegenerate multimode optomechanics. *Physical Review A* **92**, 013851 (2015).
47. M. S. Sarandy, D. A. Lidar, Adiabatic approximation in open quantum systems. *Physical Review A* **71**, 012331 (2005).
48. A somewhat broader definition is discussed in Ref. (45).
49. In its simplest form, PA occurs for a single mode governed by $\ddot{x} + \gamma\dot{x} + \omega_0^2(1 + \epsilon\cos(\omega_{\text{mod}}t))x = 0$. In such systems, gain is achieved most readily for $\omega_{\text{mod}} = 2\omega_0$.
50. This follows from assuming that traversing a generic loop \mathcal{C} in time T results in dynamical loss $\text{Im}(\phi_{\text{D}}) \approx -\gamma T$ and geometric gain (assuming \mathcal{C} is traversed in the appropriate direction) $\text{Im}(\phi_{\text{B}}) \approx -1$. These cancel for $\gamma \approx T^{-1}$.
51. Ibáñez, S., Martínez-Garaot, S., Chen, X., Torrontegui, E. & Muga, J. G. Shortcuts to adiabaticity for non-Hermitian systems. *Physical Review A* **84**, 023415 (2011).
52. A. Baksic, R. Belyansky, H. Ribeiro, A. A. Clerk, Shortcuts to adiabaticity in the presence of a continuum: Applications to itinerant quantum state transfer. *Physical Review A* **96**, 021801(R) (2017).
53. M. V. Berry, Transitionless quantum driving. *Journal of Physics A* **42**, 365303 (2009).

Supplementary Materials

§0 Table of Contents

1	Details of the experimental setup	3
1.1	The cavity optomechanical system	3
1.2	Laser control and readout	3
2	Optomechanical model	5
2.1	The Hamiltonian	5
2.2	The rotating frame \mathcal{R}	8
3	System characterization	10
3.1	Undriven motion	11
3.2	Characterization using a single control tone	11
3.3	Characterization using two control tones	11
4	Measuring the propagator matrix for a control path	12
4.1	Protocol for measuring $\beta(T)$	12
4.2	Extracting the state vector from ringdown measurements	15
4.3	Measuring the propagator matrix $U(T)$	18
5	The propagator matrix and the geometric phase	21
5.1	The asymptotic form of the accumulated phase	21
5.2	Criteria for fitting the data	24
6	Calculating the geometric phase	25
6.1	Geometric phase for “simple” control loops	25
6.2	Geometric intuition for the complex Berry phase	26
6.3	Numerical method for calculating the geometric phase	29
7	Gauge-invariance of the imaginary part of the Berry connection	29
8	Steady-state geometric gain	30
8.1	Defining SSGG	31
8.2	Identifying control loops that produce SSGG	32
8.3	SSGG with simple loops	33
8.4	SSGG with non-simple loops	36
9	Extended data	38
9.1	Additional measurements using “simple” control loops	39
9.2	Control loops with non-constant speed	40
9.3	“Non-simple” control loops	40
9.4	Measurements using a different mechanical mode	44

§1 Details of the experimental setup

This section provides a detailed description of the experimental apparatus and methods. This includes the optical and electronic components, as well as the various schemes used to stabilize the apparatus.

§1.1 The cavity optomechanical system

The device consists of a $500\ \mu\text{m} \times 500\ \mu\text{m} \times 150\ \text{nm}$ silicon nitride membrane inside an optical Fabry-Pérot cavity. The membrane is mounted near to the cavity's waist, and with the cavity's axis normal to the membrane.

The cavity is formed by two mirrors separated by 7 mm, each having a radius of curvature 10 mm. The mirrors are specified to have reflectivity $R = 0.99975$, and loss (due to scattering and absorption) ~ 50 ppm for 1550 nm light. With the membrane inside the cavity, the finesse $\mathcal{F} = 10,500$.

The mirrors are mounted on piezo elements, which are used to ensure that the membrane is located roughly midway between a node and an antinode of the cavity optical mode (this maximizes the linear coupling between the cavity mode and the membrane's motion). The laser drives a TEM₀₀ mode of the cavity, with input coupling rate $\kappa_{\text{in}}/\kappa = 0.346$.

The experiment is housed in a room-temperature vacuum chamber with pressure less than 6×10^{-8} mBar. To minimize drifts in the device's parameters, it is mounted on a thermoelectric cooler that stabilizes the device's temperature to within 1 mK.

The membrane's normal vibrational modes are indexed as (m, n) where m and n are the number of antinodes in the x and y directions, respectively. We use the (3,3), (5,2) and (5,3) modes, which we refer to as “mode 1”, “mode 2”, and “mode 3”. Their bare resonant frequencies $\omega_1^{(0)}, \omega_2^{(0)}, \omega_3^{(0)}$ and bare decay rates $\gamma_1^{(0)}, \gamma_2^{(0)}, \gamma_3^{(0)}$ are given in Table S1.

For all of the measurements described here, both the optomechanically-induced shift in the mechanical modes' resonance frequencies and the optomechanically-induced damping rate are $\lesssim 2\pi \times 10^2$ Hz.

§1.2 Laser control and readout

All of the laser tones are generated from an NKT Adjustik laser, which is detuned by -83 MHz from the cavity mode of interest (Fig. S1). The laser is split into several tones that are recombined before being sent to the cavity. The first tone (“probe”) is shifted $+83$ MHz by an acousto-optic modulator (pAOM, Gooch and Housego FiberQ) driven by function generator FG1 (RIGOL DG4162). This tone is locked to the cavity resonance using standard Pound-Drever-Hall (PDH) techniques with phase modulation sidebands at ± 32.5 MHz that are created by driving an electro-optic modulator (EOM, Thorlabs LN65S-FC) with the RF output of a laser lock box (MOKU:Lab).

This tone is recombined with the unshifted laser, which serves as a local oscillator (LO) for the heterodyne measurements (described below) before being sent to one arm of a polarizing beam splitter (Thorlabs PBS PFC1550A). To prevent low-frequency power fluctuations, both the

probe and LO beams are stabilized by monitoring the power of each beam and sending the result to the input of a PID controller (New Focus LB10005), which tunes an optical attenuator (VOA) (Thorlabs V1550A and V1550PA for the probe and LO, respectively).

We also optimize the polarization of each beam with fiber paddle tensioners (Thorlabs FPC032), and pass the combined LO and probe beam through an in-line polarizer (Thorlabs ILP1550PM-APC) to optimize the input to the polarizing beam splitter.

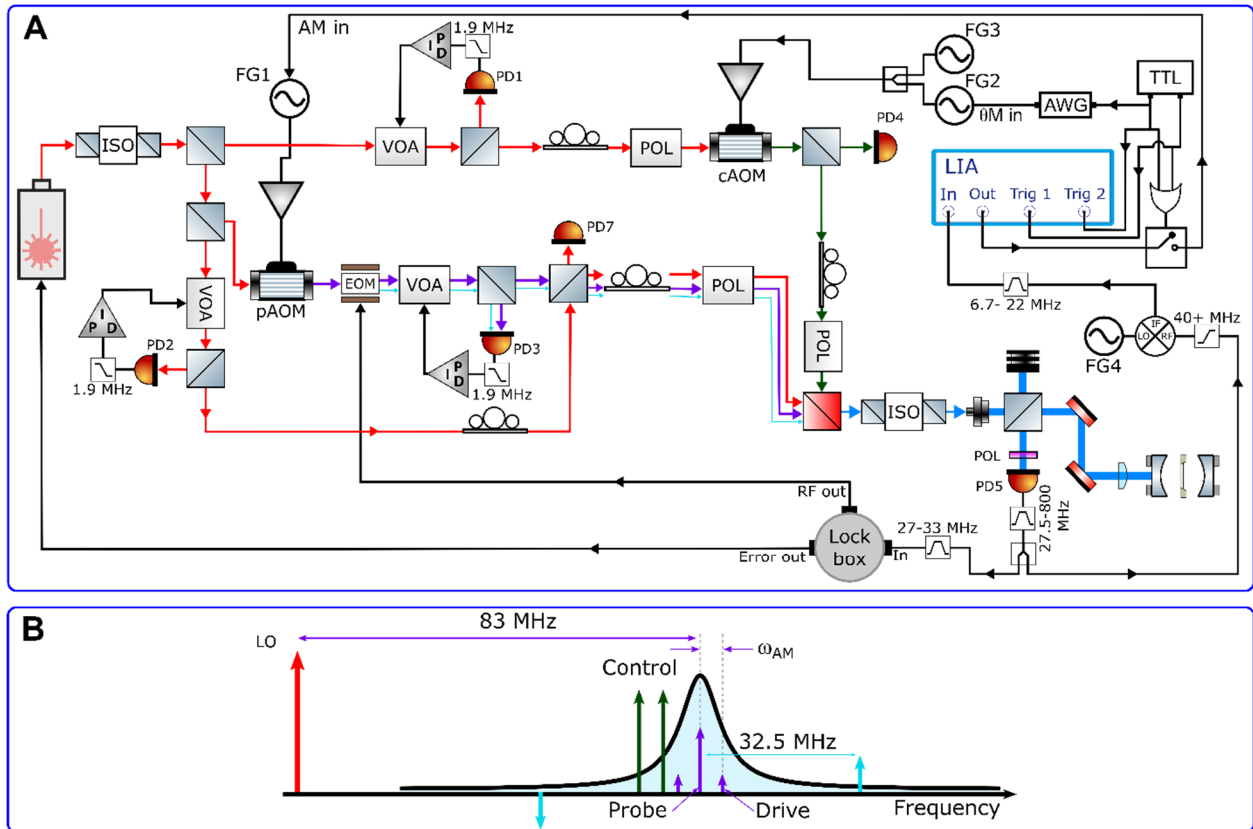


Figure S1: (A) Detailed experimental setup. ISO: isolator, VOA: variable optical attenuator, POL: polarizer, AOM: acousto-optic modulator, EOM: electro-optic modulator, PD: photodiode, FG: function generator, AWG: arbitrary waveform generator, LIA: lock in amplifier. Black lines: electronic paths, colored lines: optical paths. (B) Frequency space diagram showing all the optical tones (arrows) and the optical cavity resonance (black curve). Red: local oscillator. Dark green: control tones. Purple: probe beam and its AM sidebands (used to drive the membrane). Blue: the probe beam’s FM sidebands, used for the PDH lock.

Another tone (“control”) is power-stabilized and sent through a second acousto-optic modulator (cAOM, Gooch and Housego Fiber-Q) which is driven by two microwave tones at $83 \text{ MHz} - \omega_1^{(0)}/(2\pi) + \delta/(2\pi)$ and $83 \text{ MHz} - \omega_2^{(0)}/(2\pi) + \delta/(2\pi) - \eta/(2\pi)$ produced by FG2 and FG3 respectively (RIGOL DG4162). The amplitude and frequency of these microwave tones define the control parameters $\{P_1, P_2, \delta, \eta\}$ in the experiment. The microwave tone from FG2 is phase modulated by an arbitrary waveform generator (AWG, RIGOL DG4162) to control the phase of the intracavity beatnote θ_{12} , one of the parameters used to define the control paths

described in the main text.

The control tone is again polarization optimized and sent to the other arm of the polarizing beam splitter (PBS), which ensures that the probe and LO have orthogonal polarization from the control tone, preventing the control tone from contaminating the heterodyne signal. This also prevents spurious driving of the membrane that would result from beating between the control tones and the probe tone.

The output of this PBS is sent to a collimator (Thorlabs CFC2A-C), and is mode matched into a TEM₀₀ mode of the optical cavity. The light reflected off the cavity is sent through a 50:50 beam splitter (Thorlabs BS015), and passes through a polarizer (Thorlabs LPNIR050-MP2) to remove the control tone prior to being recorded by a high frequency photodetector (PD5, Thorlabs PDA10CF). The electrical signal from this photodetector is split, filtered, and sent into the lock box, where the PDH signal at 32.5 MHz is mixed down to DC to generate a lock error signal, which is fed to the laser's piezo driver.

When the membrane oscillates at a frequency ω , it imparts phase modulation sidebands on the probe tone. The intensity beatnote between the probe and the LO is detected by PD5 which converts it to an electrical signal at $83 \text{ MHz} \pm \omega/(2\pi)$, which is then mixed with a tone at 99.354 MHz (FG4, Vaunix LMS-451D-13) and bandpass filtered to isolate the heterodyne signal at $16.354 \text{ MHz} \pm \omega/(2\pi)$. This signal is sent to the LIA, where it is mixed down by two demodulation oscillators: one at frequency $16.354 \text{ MHz} + \omega_1^{\text{mod}}/(2\pi)$ and one at $16.354 \text{ MHz} + \omega_2^{\text{mod}}/(2\pi)$, with $\omega_1^{\text{mod}} \approx \omega_1^{(0)}$ and $\omega_2^{\text{mod}} \approx \omega_2^{(0)}$. In this manner, each quadrature of the beatnote at $16.354 \text{ MHz} + \omega/(2\pi)$ is converted to a voltage signal, which we use to extract the complex motional amplitudes.

To drive the membrane's motion, we use a tone with frequency $\omega_d/(2\pi) \sim \omega_i^{(0)}/(2\pi)$ generated by the lock in amplifier (LIA, Zurich Instrument HF2) to amplitude modulate (AM) the 83 MHz tone that drives the pAOM. The AM tone is gated using a fast microwave switch (Minicircuits ZASWA-2-50DRA+) which is toggled by a TTL signal. The falling edge of this TTL signal triggers the start of the control loop.

§2 Optomechanical model

This section describes the theoretical model of the optomechanical system. This model includes the interactions between the membrane and the optical cavity, as well as the manner in which the laser tones appear as control parameters in the mechanical modes' dynamical matrix (which is commonly referred to as its "Hamiltonian").

§2.1 The Hamiltonian

We consider a system of two mechanical modes coupled to a single optical cavity mode. The classical Hamiltonian function for the full system is given by:

$$H_{\text{full}} = \hbar \left(\Omega - i \frac{\kappa}{2} \right) a^* a + \sum_{j=1}^2 \hbar \left(\omega_j^{(0)} - i \frac{\gamma_j^{(0)}}{2} \right) \tilde{c}_j^* \tilde{c}_j + \sum_{j=1}^2 \hbar g_j (\tilde{c}_j + \tilde{c}_j^*) a^* a + \sum_{j=1}^2 \hbar (A_j a^* a) \tilde{c}_j^* \tilde{c}_j \quad (\text{S1})$$

Where Ω is the resonance frequency of the optical mode, a is the complex-valued amplitude of the optical mode driven by the control laser, \tilde{c}_j are the complex-valued amplitudes of the two mechanical modes, and $*$ denotes complex conjugation. The first two terms correspond to the uncoupled optical and mechanical oscillators respectively. The third term corresponds to radiation pressure coupling between the two with coupling strengths g_j . The last term (which we refer to as photothermal) describes the temperature-dependence of the mechanical modes' resonance frequencies and the heating of the membrane by the control laser. We note that the appearance of the reduced Planck's constant \hbar serves only to conform with the broader literature on optomechanics, where the coupling strengths g_j are usually given as single-photon rates. For consistency, the thermal response coefficients A_j are also given as single-photon rates. Values of these parameters (as determined by measurements described in §3) are provided in Table S1.

The dynamics of a and c_j are governed by Hamilton's equations of motion. In particular, the optical mode a is driven by two control laser tones (with input coupling κ_{in}) as given below:

$$a_{\text{in}} = e^{-i\Omega t} \sum_{n=1}^2 \sqrt{\frac{P_n}{\hbar(\Omega + \Delta_n)}} e^{-i(\Delta_n t + \theta_n)} \quad (\text{S2})$$

where P_n, Δ_n, θ_n are the power, detuning (from the cavity resonance) and phase of the n^{th} control tone, respectively. For our system, $\kappa \gg \{g_j, \gamma_j, A_j\}$, so we can linearize the optomechanical coupling term and adiabatically eliminate the optical field.

Furthermore, the intensity beatnote between the two control tones is at frequency $|\Delta_{12}| = |\Delta_1 - \Delta_2| \approx |\omega_1^{(0)} - \omega_2^{(0)}|$, which provides coupling between the two mechanical modes. Under the rotating wave approximation (54,55) the resulting effective equation of motion for the two mechanical modes is given by:

$$i \dot{\vec{c}}_{\text{lab}}(t) = H_{\text{lab}}(t) \vec{c}_{\text{lab}}(t) \quad (\text{S3})$$

in the lab frame, where $\vec{c}_{\text{lab}}(t) = (\tilde{c}_1(t), \tilde{c}_2(t))^T$ denotes the mechanical modes' complex-valued amplitudes and

$$H_{\text{lab}}(t) = \begin{pmatrix} \omega_1^{(0)} - \frac{i\gamma_1^{(0)}}{2} + \sum_{n=1}^2 \sigma_{nn,1}(t) + A_1 n_{\text{op}}(t) & \sigma_{12}(t) e^{i(\Delta_{12}(t)t + \theta_{12}(t))} \\ \sigma_{21}(t) e^{-i(\Delta_{12}(t)t + \theta_{12}(t))} & \omega_2^{(0)} - \frac{i\gamma_2^{(0)}}{2} + \sum_{n=1}^2 \sigma_{nn,2}(t) + A_2 n_{\text{op}}(t) \end{pmatrix} \quad (\text{S4})$$

where

$$\sigma_{nn,j}(t) = -i\kappa_{\text{in}} g_j^2 \frac{P_n(t)}{\hbar\Omega} |\chi_c(\Delta_n(t))|^2 \left(\chi_c(\omega_j^{(0)} + \Delta_n(t)) - \chi_c(\omega_j^{(0)} - \Delta_n(t)) \right)$$

$$\begin{aligned} \sigma_{12}(t) = & -i\kappa_{\text{in}} g_1 g_2 \frac{\sqrt{P_1(t)P_2(t)}}{\hbar\Omega} \chi_c^*(\Delta_1(t)) \chi_c(\Delta_2(t)) \left(\chi_c(\omega_1^{(0)} + \Delta_1(t)) \right. \\ & \left. - \chi_c(\omega_1^{(0)} - \Delta_2(t)) \right) \end{aligned}$$

$$\begin{aligned} \sigma_{21}(t) = & -i\kappa_{\text{in}} g_1 g_2 \frac{\sqrt{P_1(t)P_2(t)}}{\hbar\Omega} \chi_c^*(\Delta_2(t)) \chi_c(\Delta_1(t)) \left(\chi_c(\omega_2^{(0)} + \Delta_2(t)) \right. \\ & \left. - \chi_c(\omega_2^{(0)} - \Delta_1(t)) \right) \end{aligned}$$

$$n_{\text{op}}(t) = \kappa_{\text{in}} \left(\frac{P_1(t)}{\hbar\Omega} |\chi_c(\Delta_1(t))|^2 + \frac{P_2(t)}{\hbar\Omega} |\chi_c(\Delta_2(t))|^2 \right)$$

$$\Delta_{12}(t) = \Delta_1(t) - \Delta_2(t)$$

$$\theta_{12}(t) = \theta_1(t) - \theta_2(t) \quad (\text{S5})$$

and $\chi_c(\omega) = (\kappa/2 - i\omega)^{-1}$ is the optical cavity susceptibility.

§2.2 The rotating frame \mathcal{R}

We note that H_{lab} is explicitly time dependent even if all of its parameters are constant, owing to the intracavity beatnote that appears in its off-diagonal terms, $e^{\pm i(\Delta_{12}t)}$. For simplicity, we remove this time dependence (but not the time dependence resulting from variations of the control parameters P_n, Δ_n, θ_n) by applying a unitary transformation S_R :

$$S_R(t) = \begin{pmatrix} e^{i(-\Delta_{12} + \omega_1^{(0)} + \omega_2^{(0)})t/2} & 0 \\ 0 & e^{i(\Delta_{12} + \omega_1^{(0)} + \omega_2^{(0)})t/2} \end{pmatrix} \quad (\text{S6})$$

Equivalently,

$$S_R(t) = \begin{pmatrix} e^{i(\omega_1^{(0)} + \frac{\eta}{2})t} & 0 \\ 0 & e^{i(\omega_2^{(0)} - \frac{\eta}{2})t} \end{pmatrix} \quad (\text{S7})$$

where $\eta = \omega_2^{(0)} - \omega_1^{(0)} - \Delta_{12}$. In this frame \mathcal{R} , the equations of motion are:

$$i\dot{\vec{c}}(t) = H(t)\vec{c}(t) \quad (\text{S8})$$

where

$$\vec{c}(t) = \begin{pmatrix} c_1(t) \\ c_2(t) \end{pmatrix} = S_R(t)\vec{c}_{\text{lab}}(t) \quad (\text{S9})$$

and

$$H(t) = S_R(t)H_{\text{lab}}(t)S_R(t)^{-1} + i\dot{S}_R(t)S_R(t)^{-1} \quad (\text{S10})$$

Under this simplification, the time-dependence of $H(t)$ is solely contained in the time dependence of the control parameters $P_n(t), \Delta_n(t), \theta_n(t)$:

$$H(t) = \begin{pmatrix} -\frac{\eta}{2} - \frac{i\gamma_1^{(0)}}{2} + \sum_{n=1}^2 \sigma_{nn,1}(t) + A_1 n_{\text{op}}(t) & \sigma_{12}(t) e^{i\theta_{12}(t)} \\ \sigma_{21}(t) e^{-i\theta_{12}(t)} & \frac{\eta}{2} - \frac{i\gamma_2^{(0)}}{2} + \sum_{n=1}^2 \sigma_{nn,2}(t) + A_2 n_{\text{op}}(t) \end{pmatrix} \quad (\text{S11})$$

Upon diagonalization of H , we obtain its eigenvalues $\vec{\Lambda} = (\lambda_+, \lambda_-)$ in the frame \mathcal{R} . In the lab frame, the mechanical susceptibility will contain components near both $\omega_1^{(0)}$ and $\omega_2^{(0)}$ (23). Thus, it is convenient to define the quantities

$$\begin{aligned} \vec{\Lambda}_1 &= (\Lambda_{1+}, \Lambda_{1-}) = \left(\omega_1^{(0)} + \frac{\eta}{2} + \lambda_+, \omega_1^{(0)} + \frac{\eta}{2} + \lambda_- \right) = \omega_1^{(0)} + \frac{\eta}{2} + \vec{\Lambda} \\ \vec{\Lambda}_2 &= (\Lambda_{2+}, \Lambda_{2-}) = \left(\omega_2^{(0)} - \frac{\eta}{2} + \lambda_+, \omega_2^{(0)} - \frac{\eta}{2} + \lambda_- \right) = \omega_2^{(0)} - \frac{\eta}{2} + \vec{\Lambda} \end{aligned} \quad (\text{S12})$$

which will be useful when considering the mechanical response in the lab frame. In the absence of any control tones, the magnitude of (the real part of) the non-degeneracy is $|\eta|$. Note that $\vec{\Lambda}$ is independent of θ_{12} .

Equation S11 may conveniently be written as:

$$H(t) = \begin{pmatrix} L(t) & M(t) e^{i\theta_{12}(t)} \\ N(t) e^{-i\theta_{12}(t)} & -L(t) \end{pmatrix} + \frac{\mathcal{T}(t)}{2} I \quad (\text{S13})$$

While a constant θ_{12} can always be set to zero by a time-independent change of coordinates, this is not possible for time-varying θ_{12} . Here I is the 2×2 identity matrix, and

$$\mathcal{T}(t) = -i \left(\frac{\gamma_1^{(0)} + \gamma_2^{(0)}}{2} \right) + \sum_{n=1}^2 \left(\sigma_{nn,1}(t) + \sigma_{nn,2}(t) \right) + (A_1 + A_2) n_{\text{op}}(t) \quad (\text{S14})$$

$$L(t) = -\frac{\eta}{2} - i \left(\frac{\gamma_1^{(0)} - \gamma_2^{(0)}}{4} \right) + \sum_{n=1}^2 \left(\frac{\sigma_{nn,1}(t) - \sigma_{nn,2}(t)}{2} \right) + \left(\frac{A_1 - A_2}{2} \right) n_{\text{op}}(t) \quad (\text{S15})$$

$$M(t) = \sigma_{12}(t) \quad N(t) = \sigma_{21}(t) \quad (\text{S16})$$

While \mathcal{T} (i.e., the trace of H) is irrelevant for the geometric phase of a control loop, it still impacts the measured signals. For example, $\text{Im}(\mathcal{T})$ sets the modes' overall damping, which in

turn sets a practical upper limit on the duration of control loops. Also, as discussed in §8, $\text{Im}(\mathcal{T})$ also plays an important role in producing steady-state geometric gain.

§3 System characterization

This section describes the measurements used to validate the model described in §2, and to determine the values of the relevant parameters.

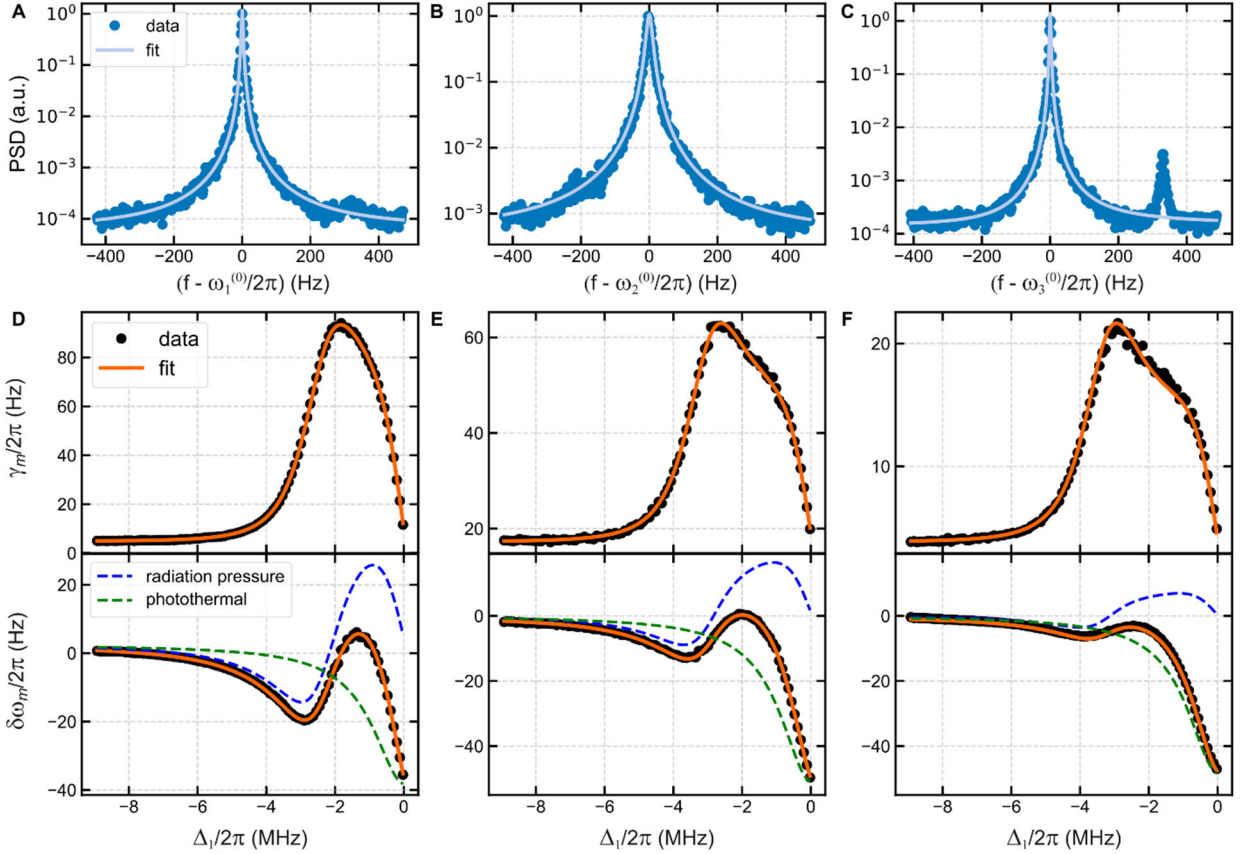


Figure S2: Characterizing the membrane modes and their optomechanical coupling. **(A – C)** Representative spectra of the membrane’s undriven motion at frequencies near the resonance of each of the three modes used in this work. **(A)** The membrane’s (3,3) mode: $\omega_1^{(0)}/2\pi = 2.423969$ MHz. **(B)** The membrane’s (5,2) mode: $\omega_2^{(0)}/2\pi = 3.076488$ MHz. **(C)** The membrane’s (5,3) mode: $\omega_3^{(0)}/2\pi = 3.331064$ MHz. In **(C)**, the small peak near 325 Hz is an aliasing artifact due to the motion of the (3,5) mode. **(D – F)** The dynamical back-action in the presence of a single laser tone with $P_1 = 17 \mu\text{W}$ and detuning Δ_1 (relative to the optical cavity resonance) for the (3,3) mode **(D)**, the (5,2) mode **(E)**, and the (5,3) mode **(F)**. Upper (lower) panels: the shift in the mode’s damping (frequency). Orange curve: fit to the optomechanical model. This model includes only radiation pressure for $\delta\gamma_i$, while for $\delta\omega_i$ it includes both radiation pressure (blue dashed curve) and the photothermal effect (green dashed curve).

§3.1 Undriven motion

To extract the bare membrane parameters $\omega_i^{(0)}, \gamma_i^{(0)}$ (the frequencies and damping rates of the i^{th} mode in the absence of dynamical back action), we turn the control tones off and measure the spectrum of the membrane's Brownian motion. We fit the power spectral density of these fluctuations in the vicinity of each resonance to the expected form (the square modulus of a Lorentzian plus a constant), which returns the best-fit value of each mode's complex eigenfrequency $\lambda_i^{(0)} = \omega_i^{(0)} - i\gamma_i^{(0)}/2$. A representative measurement for each mode is shown in Fig. S2, A – C.

§3.2 Characterization using a single control tone

In presence of a single control tone, H is diagonal, and its eigenvalues (i.e. H_{11} and H_{22}) encode the change in damping rate (imaginary part) and resonance frequency (real part) for each mechanical mode. The damping rate is tuned via radiation pressure-induced dynamical back-action (DBA) (44), while the resonance frequency is tuned by both DBA and the photothermal effect defined above.

To illustrate this, we apply a single control tone with power $P_1 = 17 \mu\text{W}$ and measure the membrane's mechanical susceptibility as a function of the control beam's detuning $\Delta_1/2\pi$. From these measurements, we extract the shift in mechanical frequency $\delta\omega_i$ and the damping γ_i . This data, along with a least-squares fit (using the eigenvalues of H as fit parameters) is show in Fig. S2, D – F.

These fits include an additional parameter Δ_{off} that represents the offset between the laser lock and the cavity resonance. For all the measurements described in this paper, we find $\Delta_{\text{off}}/2\pi < 50 \text{ kHz}$. While this offset is essentially negligible for the analysis presented here, for consistency we replace $\Delta \rightarrow \Delta + \Delta_{\text{off}}$ in all expressions when comparing them with data.

§3.3 Characterization using two control tones

Here, we provide details of the susceptibility measurements shown in Fig. 1C of the main text. These measurements are similar to those described in §3.2, except we now apply two control tones, resulting in coupling between the two mechanical modes. As described in the main text, we measure two copies of the mechanical susceptibility near $\omega_1^{(0)}$ and $\omega_2^{(0)}$ while varying $P_1 = P_2 = P$ and δ on a rectangular grid with a fixed value of η . Each copy of the mechanical susceptibility is fit to the sum of two complex Lorentzians (plus a complex constant to account for feed-through from the drive) to obtain the system's eigenvalues in the rotating frame \mathcal{R} . In particular, the mechanical susceptibility near $\omega_1^{(0)}$ ($\omega_2^{(0)}$) is fit to extract the complex eigenfrequencies $\vec{\Lambda}_1 = (\Lambda_{1+}, \Lambda_{1-})$ ($\vec{\Lambda}_2 = (\Lambda_{2+}, \Lambda_{2-})$), as illustrated in Fig. 1C of the main text.

This fit provides λ_+, λ_- , from which we calculate $D = (\lambda_+ - \lambda_-)^2$ and $\mathcal{T} = \lambda_+ + \lambda_-$ at each point $\{P, \delta\}$ on the grid. D and \mathcal{T} are simple functions of H :

$$D = \mathcal{T}^2 - 4\det(H)$$

$$\mathcal{T} = \text{tr}(H) \quad (\text{S17})$$

where tr is the trace, \det is the determinant, and D is the discriminant of the matrix's characteristic polynomial. Using the above relations, we fit the measured D and \mathcal{T} to obtain the best-fit values of $\kappa, g_1, g_2, A_1, A_2, \Delta_{\text{off}}$, which define the optomechanical Hamiltonian of our system. These values are given in Table S1.

Parameter	Best fit value	Drift range
$\omega_1^{(0)}/2\pi$	2.423969 MHz	20 Hz
$\omega_2^{(0)}/2\pi$	3.076488 MHz	20 Hz
$\omega_3^{(0)}/2\pi$	3.331064 MHz	20 Hz
$\gamma_1^{(0)}/2\pi$	3.6 Hz	0.5 Hz
$\gamma_2^{(0)}/2\pi$	16.2 Hz	0.5 Hz
$\gamma_3^{(0)}/2\pi$	3.35 Hz	0.5 Hz
$\kappa/2\pi$	2.32 MHz	0.1 MHz
$g_1/2\pi$	4.4 Hz	0.1 Hz
$g_2/2\pi$	3.9 Hz	0.1 Hz
$g_3/2\pi$	2.64 Hz	0.1 Hz
$A_1/2\pi$	-2.8 μHz	0.5 μHz
$A_2/2\pi$	-4.0 μHz	0.5 μHz
$A_3/2\pi$	-3.58 μHz	0.5 μHz
$\Delta_{\text{off}}/2\pi$	-10 kHz	10 kHz

Table S1: The best-fit values of the parameters appearing in the optomechanical Hamiltonian. For all quantities, the subscript denotes the mechanical mode: $1 \rightarrow (3,3)$, $2 \rightarrow (5,2)$, $3 \rightarrow (5,3)$. The best-fit values are given for a typical day. Small drifts in these parameters are tracked throughout the measurements prescribed here, and are included in all comparisons with theory. The rightmost column gives the extent of the parameters' drift over several months.

§4 Measuring the propagator matrix for a control path

This section gives a detailed description of the protocol used to measure the phase accumulated by the membrane's oscillations when its control parameters are varied along a path.

§4.1 Protocol for measuring $\beta(T)$

In this section, we provide additional information on measuring $\beta(T)$ for a given control path. The process of measuring $\beta(T)$ is summarized in the following steps:

1. The optomechanical control parameters $\{P_1, P_2, \delta, \eta, \theta_{12}\}$ are tuned to their values at the beginning of the loop, setting the Hamiltonian of the mechanical system to its initial value $H(0)$.
2. A drive is applied at frequency ω_d to ring the membrane up to its initial state vector $\vec{c}^{(a)}(0)$.
3. The drive is turned off. This defines $t = 0$.
4. While the membrane rings down (i.e. evolves under the time independent Hamiltonian $H(0)$), we record the heterodyne signal demodulated by two oscillators at frequencies $\omega_1^{\text{mod}} = \omega_d$ and ω_2^{mod} . This measurement corresponds to the left column of main text Fig. 2, C and D.
5. Steps 2 – 3 are repeated. After the drive is turned off, the control parameters are tuned along some control path for a duration T (e.g., by setting $\theta_{12}(t) = 2\pi t/T$) such that the system evolves under a time dependent Hamiltonian $H(t)$. For $t > T$ the membrane is allowed to ring down (i.e. evolve under constant $H(T)$), and we record the heterodyne signal demodulated by the same two oscillators at ω_1^{mod} and ω_2^{mod} . This measurement corresponds to the right column of main text Fig. 2, C and D.
6. We repeat the measurements described above, alternating between free ringdown (step 4) and the control path (step 5). Typically 50 – 500 measurements of each type are averaged to increase the signal to noise ratio (SNR).
7. We fit the “free ringdown” data to extract the initial state vector $\vec{c}^{(a)}(0)$ immediately after the drive is turned off, and the “control path” data to extract the state vector $\vec{c}^{(a)}(T)$ after a control path of duration T is performed (see §4.2 for details).
8. In order to determine the four complex components of the propagator matrix $U(T)$ (defined by $\vec{c}(T) = U(T)\vec{c}(0)$), we measure the evolution of two linearly independent initial state vectors. Thus, we repeat steps 2 – 7 above, choosing a different value for the drive frequency ω_d , which rings the membrane up to an initial state vector $\vec{c}^{(b)}(0)$ that is linearly independent of $\vec{c}^{(a)}(0)$. The vectors $\{\vec{c}^{(a)}(0), \vec{c}^{(b)}(0), \vec{c}^{(a)}(T), \vec{c}^{(b)}(T)\}$ yield sufficient information to determine the propagator in the “forwards” direction $U_{\mathcal{U}}(T)$ (see §4.3 for details).
9. We repeat the entire series of measurements described in steps 2 – 8, varying the control path duration T to determine $U_{\mathcal{U}}(T)$ as a function of T .
10. We repeat the series of measurements described in steps 1 – 9, except that we apply the “time reversed” version of the control path from the above measurements. For example, if the “forward” circuit was defined by $\theta_{12}(t) = 2\pi t/T$, the “time reversed” circuit would be defined by $\theta_{12}(t) = -2\pi t/T$ (see main text Fig. 2C, magenta line). This measurement gives the “time reversed” propagator $U_{\mathcal{V}}(T)$.

11. From these data, we calculate $\beta(T) = -i \log(U_{++,\sigma}/U_{++,\nu})/2$ which (up to a choice of the branch of the logarithm, see discussion in §5.1) tends to the complex geometric phase $\Phi_{B,\nu}$ at large T . Here the least-damped mode is indexed by the subscript $+$. This sequence constitutes the measurement of $\beta(T)$ for a given control path.

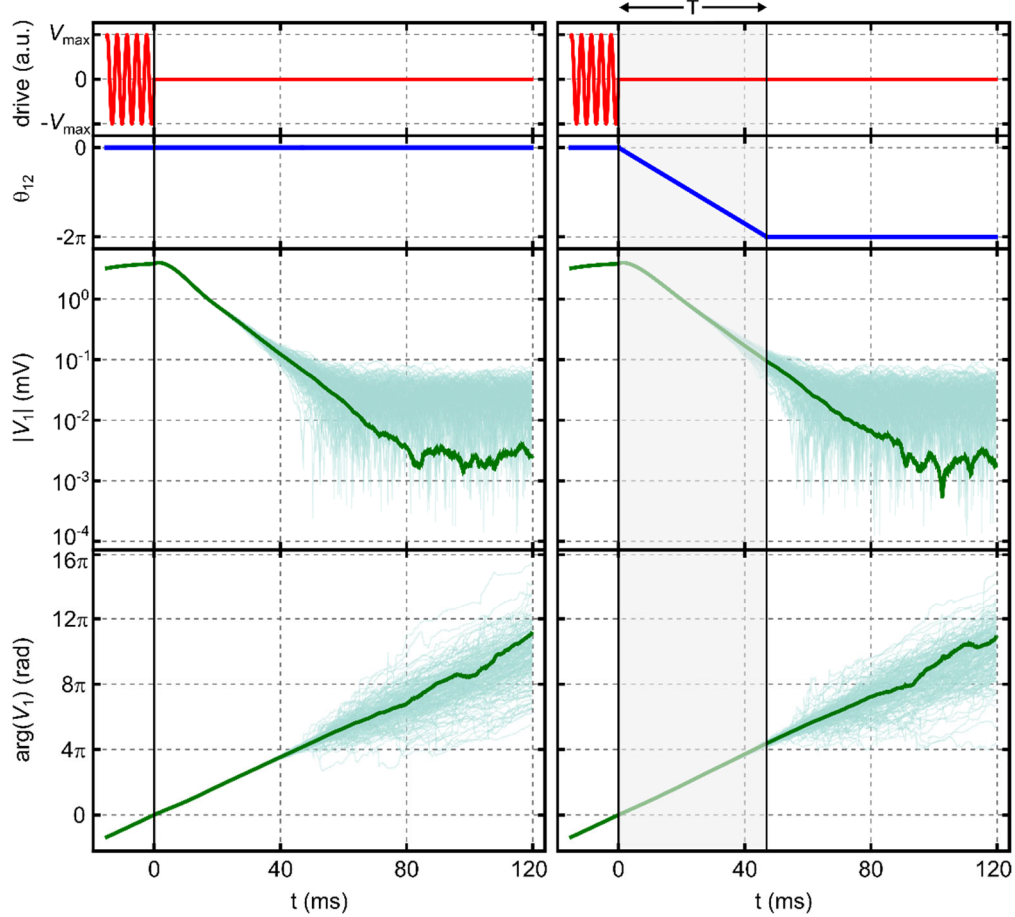


Figure S3: Averaging multiple records. Left column: measurements with no control loop. Right column: measurements with the control loop. Red: a schematic illustration of the driving force applied to the membrane, which is switched off at $t = 0$. Blue: a plot of the beatnote phase $\theta_{12}(t)$. Green: the magnitude and phase of the heterodyne signals. For each individual trace (faint green lines) the phase of the heterodyne signal is set to 0 for $t = 0$ (when the drive turns off). This ensures that the average of multiple traces (solid green line) reveals motion that results from the drive. The phase is referenced at the same point ($t = 0$) for both the simple ringdown measurement (left column) and control path measurement (right column), so that the $\vec{c}^{(a)}(0)$ and $\vec{c}^{(a)}(T)$ have a common phase reference (and equivalently for $\vec{c}^{(b)}(0)$ and $\vec{c}^{(b)}(T)$).

Prior to performing this measurement sequence, we measure the Brownian motion spectrum with the control tones off to obtain the bare mechanical frequencies ($\omega_1^{(0)}$ and $\omega_2^{(0)}$, see §3.1). We then perform a measurement of the membrane's susceptibility with the control tones on to extract the frequencies Λ_{ij} . This static spectroscopy is also performed intermittently during a measurement

sequence to track any drift in the setup’s parameters that may occur during data acquisition. A typical measurement of $\beta(T)$ for a given control loop (see for example main text Fig. 2F) lasts ~ 4 hours, during which time the static spectroscopy measurement is performed every 15 minutes. The drive and demodulation frequencies (discussed in the following paragraphs) are updated based on these measurements.

The values of Λ_{ij} gleaned from these measurements are used to set the drive frequency ω_d and the demodulation frequencies ω_1^{mod} and ω_2^{mod} . Specifically, we choose ω_d to be the real part of one of the four Λ_{ij} . Any choice of the four values of $\text{Re}(\Lambda_{ij})$ results in a distinct initialization of the mechanical state vector. However, to reconstruct the propagator matrix $U(T)$ for a control path of duration T , we measure initial and the final state vectors for two linearly independent initializations of the state vector; these are the $\vec{c}^{(a)}(0)$ and $\vec{c}^{(b)}(0)$ introduced above in Steps 2 & 8. To ensure that $\vec{c}^{(a)}(0)$ and $\vec{c}^{(b)}(0)$ are linearly independent to a degree sufficient to accurately determine the propagator, we initialize $\vec{c}^{(a)}(0)$ with $\omega_d = \text{Re}(\Lambda_{1j}) \sim \omega_1^{(0)}$ and $\vec{c}^{(b)}(0)$ with $\omega_d = \text{Re}(\Lambda_{2j}) \sim \omega_2^{(0)}$.

The frequencies of the demodulation oscillators are also chosen from among the four $\text{Re}(\Lambda_{ij})$ with one being equal to ω_d . Specifically, we choose $\omega_1^{\text{mod}} = \text{Re}(\Lambda_{1j}) \sim \omega_1^{(0)}$ and $\omega_2^{\text{mod}} = \text{Re}(\Lambda_{2j}) \sim \omega_2^{(0)}$.

When averaging multiple records of the heterodyne signal $V(t)$ (with the i th record denoted as $V_i(t)$), it is important to account for the phase of $V_i(t)$. For each $V_i(t)$, we reference the phase at the end of the drive to zero, i.e. we set $\arg[V_i(0)] = 0$. This ensures that, upon averaging, coherent motion of the membrane induced by the drive is in phase for all i , while incoherent noise will tend to average to zero. It is also important to choose the same reference time (i.e., the end of the drive) for both the “free ringdown” measurement and the “control path” measurement, as this ensures that the state vectors $\vec{c}^{(a)}(0)$ and $\vec{c}^{(a)}(T)$ have a common phase reference. The averaging is illustrated in Fig. S3, where individual measurements (faint lines) are plotted along with the averaged result (thick green line).

§4.2 Extracting the state vector from ringdown measurements

When the control parameters are held fixed and the drive is off, the free ringdown of the mechanical modes may be written in the lab frame as a solution $\vec{c}_{\text{lab}}(t)$ to Eq. S3. For simplicity, we first solve for $\vec{c}(t)$ in the rotating frame \mathcal{R} and then apply a unitary transformation ($S_{\mathcal{R}}^{-1}$) to convert motional amplitudes in the frame \mathcal{R} to the lab frame (see §2.2).

To solve $\vec{c}(t)$ in the frame \mathcal{R} , we rewrite Eq. S2 as:

$$i\dot{\vec{c}}_{\mathcal{D}}(t) = H_{\mathcal{D}}\vec{c}_{\mathcal{D}}(t) \quad (\text{S18})$$

where we introduce the diagonal frame state vector $\vec{c}_{\mathcal{D}}(t) = (\bar{c}_+(t), \bar{c}_-(t))^T = S_{\mathcal{D}}^{-1}\vec{c}(t)$ and Hamiltonian

$$H_D = \begin{pmatrix} \lambda_+ & 0 \\ 0 & \lambda_- \end{pmatrix} = S_D^{-1} H S_D \quad (\text{S19})$$

where λ_+ and λ_- are the eigenvalues of the system in frame \mathcal{R} and the columns of S_D (rows of S_D^{-1}) are composed of the normalized right (left) eigenvectors of H . We emphasize that H, H_D, S_D, S_D^{-1} are time independent because the control parameters are held fixed before the start of the loop (for state initialization), and at the end of the loop (for post-control-loop ringdown).

The solution of Eq. S18 is:

$$\vec{c}_D(t) = \begin{pmatrix} \bar{c}_+ e^{-i\lambda_+ t} \\ \bar{c}_- e^{-i\lambda_- t} \end{pmatrix} \quad (\text{S20})$$

where \bar{c}_i is the complex motional amplitude of normal mode $i \in \{+, -\}$ at the instant when the radiation pressure drive is turned off. Writing

$$S_D = \begin{pmatrix} u_{11} & u_{12} \\ u_{21} & u_{22} \end{pmatrix} \quad (\text{S21})$$

gives

$$\vec{c}(t) = S_D \vec{c}_D(t) = \begin{pmatrix} u_{11} \bar{c}_+ e^{-i\lambda_+ t} + u_{12} \bar{c}_- e^{-i\lambda_- t} \\ u_{21} \bar{c}_+ e^{-i\lambda_+ t} + u_{22} \bar{c}_- e^{-i\lambda_- t} \end{pmatrix} \quad (\text{S22})$$

and

$$\vec{c}_{\text{lab}}(t) = S_R^{-1}(t) \vec{c}(t) = S_R^{-1}(t) S_D \vec{c}_D(t) = \begin{pmatrix} u_{11} \bar{c}_+ e^{-i(\lambda_+ + \omega_1^{(0)} + \frac{\eta}{2})t} + u_{12} \bar{c}_- e^{-i(\lambda_- + \omega_1^{(0)} + \frac{\eta}{2})t} \\ u_{21} \bar{c}_+ e^{-i(\lambda_+ + \omega_2^{(0)} - \frac{\eta}{2})t} + u_{22} \bar{c}_- e^{-i(\lambda_- + \omega_2^{(0)} - \frac{\eta}{2})t} \end{pmatrix} \quad (\text{S23})$$

Or, more succinctly via Eq. S12:

$$\vec{c}_{\text{lab}}(t) = \begin{pmatrix} u_{11} \bar{c}_+ e^{-i\Lambda_1 t} + u_{12} \bar{c}_- e^{-i\Lambda_1 t} \\ u_{21} \bar{c}_+ e^{-i\Lambda_2 t} + u_{22} \bar{c}_- e^{-i\Lambda_2 t} \end{pmatrix} \quad (\text{S24})$$

This motion is transduced onto the optical field, converted into an electronic signal, and measured by the LIA as $\rho \chi_c(\omega) \vec{g} \cdot \vec{c}_{\text{lab}}(t)$, where ρ is the transduction gain, $\chi_c(\omega)$ is the cavity susceptibility and $\vec{g} = (g_1, g_2)$ is the vector of optomechanical coupling strengths and \cdot is the

usual dot product. This signal is then demodulated by the LIA at frequencies ω_1^{mod} and ω_2^{mod} and passed through a low-pass filter with bandwidth $BW \ll |\omega_1^{(0)} - \omega_2^{(0)}|$. The complex demodulated signals at ω_1^{mod} and ω_2^{mod} are:

$$\begin{aligned} V_1(t) &= \rho \chi_c(\omega_1^{\text{mod}}) g_1 (W(\Lambda_{1+}, \omega_1^{\text{mod}}) u_{11} \bar{c}_+ e^{-i\Lambda_{1+}t} + W(\Lambda_{1-}, \omega_1^{\text{mod}}) u_{12} \bar{c}_- e^{-i\Lambda_{1-}t}) e^{i\omega_1^{\text{mod}}t} \\ V_2(t) &= \rho \chi_c(\omega_2^{\text{mod}}) g_2 (W(\Lambda_{2+}, \omega_2^{\text{mod}}) u_{21} \bar{c}_+ e^{-i\Lambda_{2+}t} + W(\Lambda_{2-}, \omega_2^{\text{mod}}) u_{22} \bar{c}_- e^{-i\Lambda_{2-}t}) e^{i\omega_2^{\text{mod}}t} \end{aligned} \quad (\text{S25})$$

respectively, where $W(\lambda, \omega) = (1 + i(\text{Re}(\lambda) - \omega)\tau_{\text{BW}})^{-n}$ is the low-pass filter function for a signal at frequency $\text{Re}(\lambda)$ that is demodulated by an oscillator at ω with a low-pass filter whose bandwidth, time-constant, and order are denoted as BW , τ_{BW} and n respectively. For the measurements in this manuscript, $n = 1$, $BW = 250$ Hz, and $\tau_{\text{BW}} = (2\pi BW)^{-1} = 0.637$ ms.

In addition, the LIA has a settling time τ_{settle} (corresponding to the 99% settling time of the LIA) that depends on n and τ_{BW} . For these measurements, $\tau_{\text{settle}} = 2.934$ ms. To accommodate this, we exclude from any fits the data in an interval τ_{settle} after the start of a ringdown.

Both $V_1(t)$ and $V_2(t)$ contain equivalent information about the complex motional amplitudes \bar{c}_+ and \bar{c}_- , up to known multiplicative factors ($\chi_c(\omega)$, $W(\lambda, \omega)$, g_i , u_{ij}) and an overall scaling factor ρ . As a reminder, the motional eigenstates at $t = 0$ are extracted from measurements of “simple” ringdowns, i.e. ringdowns without a control path. The signals $V_1(t)$ and $V_2(t)$ recorded in such a measurement (Eq. S25) are fit to:

$$\begin{aligned} V_1(t) &= b_1 + A_{11}(t) W(\Lambda_{1+}, \omega_1^{\text{mod}}) e^{-i(\Lambda_{1+} - \omega_1^{\text{mod}})t} + A_{12}(t) W(\Lambda_{1-}, \omega_1^{\text{mod}}) e^{-i(\Lambda_{1-} - \omega_1^{\text{mod}})t} \\ V_2(t) &= b_2 + A_{21}(t) W(\Lambda_{2+}, \omega_2^{\text{mod}}) e^{-i(\Lambda_{2+} - \omega_2^{\text{mod}})t} + A_{22}(t) W(\Lambda_{2-}, \omega_2^{\text{mod}}) e^{-i(\Lambda_{2-} - \omega_2^{\text{mod}})t} \end{aligned} \quad (\text{S26})$$

respectively. Here, λ_{\pm} and b_i, A_{ij} , with $i, j \in 1, 2$ are the 8 complex-valued fit parameters, which denote the system’s eigenvalues, the heterodyne signal’s background, and the amplitudes of the decaying exponentials, respectively (λ_{\pm} appear in Eq. S26 by way of Eq. S12). By comparing Eqs. S25 and S26, the complex amplitudes at $t = 0$ can be written as

$$\begin{aligned} \bar{c}_+(0) &= \frac{A_{11}(0)}{\rho \chi_c(\omega_1^{(0)}) g_1 u_{11}} = \frac{A_{21}(0)}{\rho \chi_c(\omega_2^{(0)}) g_2 u_{21}} \\ \bar{c}_-(0) &= \frac{A_{12}(0)}{\rho \chi_c(\omega_1^{(0)}) g_1 u_{12}} = \frac{A_{22}(0)}{\rho \chi_c(\omega_2^{(0)}) g_2 u_{22}} \end{aligned} \quad (\text{S27})$$

which highlights the fact $V_1(t)$ and $V_2(t)$ contain redundant information about motional amplitudes. In practice, we simply use the fit parameters obtained from the fit to $V_1(t)$ (i.e. $A_{11}(t)$ and $A_{12}(t)$) to calculate $\bar{c}_+(0)$ and $\bar{c}_-(0)$ (this is justified in the next paragraph).

Expressions similar to Eqs. S27 may also be used to extract the amplitudes of the normal modes' motion at $t = T$ i.e., $\bar{c}_+(T)$ and $\bar{c}_-(T)$, from the data corresponding to ringdown after a control path. However, for large T , the motion may decay significantly before the completion of the control path, resulting in low SNR and potentially compromising the quality of the fit. In practice, we observe that the signal near $\omega_1^{(0)}$, and correspondingly $V_1(t)$, tends to have a larger SNR than $V_2(t)$ near $\omega_2^{(0)}$ after long loops. Thus, to obtain complex motional amplitudes at the end of the loop, we fit only $V_1(t)$.

Additionally, we use only 3 complex fit parameters $\{b_i, A_{11}(T), A_{12}(T)\}$ in this fit, fixing the eigenvalues λ_1 and λ_2 to values obtained by fitting the corresponding initialization ringdown data. We justify the choice of fixing the eigenvalues during the fit by noting that (a) for all control loops in this manuscript, the eigenvalues at the beginning of the circuit are equal to the eigenvalues at the end of the circuit, and (b) the individual measurements of complex-averaged datasets were interleaved, which reduces the impact of systematic errors caused by temporal drifts.

From this fit, we obtain the complex motional amplitudes at $t = T$ which can be written as

$$\bar{c}_+(T) = \frac{A_{11}(T)}{\rho\chi_c(\omega_1^{(0)})g_1u_{11}} \quad (\text{S28})$$

$$\bar{c}_-(T) = \frac{A_{12}(T)}{\rho\chi_c(\omega_1^{(0)})g_1u_{12}} \quad (\text{S29})$$

§4.3 Measuring the propagator matrix $U(T)$

As described above, in order to reconstruct the full propagator $U(T)$ for a control path of duration T , we measure initial and the final state vectors for two linearly independent initializations of the state vector $\vec{c}^{(a)}(0)$ and $\vec{c}^{(b)}(0)$. Thus, for every value of T , we measure $\{\bar{c}_+^{(a)}(0), \bar{c}_-^{(a)}(0), \bar{c}_+^{(a)}(T), \bar{c}_-^{(a)}(T)\}$ and $\{\bar{c}_+^{(b)}(0), \bar{c}_-^{(b)}(0), \bar{c}_+^{(b)}(T), \bar{c}_-^{(b)}(T)\}$. The matrix equation that connects the initial and final complex amplitudes is given by:

$$\begin{pmatrix} \bar{c}_+(T) \\ \bar{c}_-(T) \end{pmatrix} = U(T) \begin{pmatrix} \bar{c}_+(0) \\ \bar{c}_-(0) \end{pmatrix} \quad (\text{S30})$$

where $U(T)$ is the complex valued propagator matrix. Explicitly,

$$U(T) = \begin{pmatrix} U_{++}(T) & U_{+-}(T) \\ U_{-+}(T) & U_{--}(T) \end{pmatrix} \quad (\text{S31})$$

The two initializations $\bar{c}^{(a)}(0)$ and $\bar{c}^{(b)}(0)$ result in four linearly independent equations relating the initial and final complex amplitudes:

$$\begin{aligned} \bar{c}_+^{(a)}(T) &= U_{++}(T)\bar{c}_+^{(a)}(0) + U_{+-}(T)\bar{c}_-^{(a)}(0) \\ \bar{c}_+^{(b)}(T) &= U_{++}(T)\bar{c}_+^{(b)}(0) + U_{+-}(T)\bar{c}_-^{(b)}(0) \\ \bar{c}_-^{(a)}(T) &= U_{-+}(T)\bar{c}_+^{(a)}(0) + U_{--}(T)\bar{c}_-^{(a)}(0) \\ \bar{c}_-^{(b)}(T) &= U_{-+}(T)\bar{c}_+^{(b)}(0) + U_{--}(T)\bar{c}_-^{(b)}(0) \end{aligned} \quad (\text{S32})$$

These four equations are sufficient to solve for $U(T)$, whose elements are given by:

$$\begin{aligned} U_{++}(T) &= \frac{\bar{c}_+^{(a)}(T)\bar{c}_-^{(b)}(0) - \bar{c}_+^{(b)}(T)\bar{c}_-^{(a)}(0)}{\bar{c}_+^{(a)}(0)\bar{c}_-^{(b)}(0) - \bar{c}_+^{(b)}(0)\bar{c}_-^{(a)}(0)} \\ U_{+-}(T) &= \frac{\bar{c}_+^{(a)}(T)\bar{c}_+^{(b)}(0) - \bar{c}_+^{(b)}(T)\bar{c}_+^{(a)}(0)}{\bar{c}_-^{(a)}(0)\bar{c}_+^{(b)}(0) - \bar{c}_-^{(b)}(0)\bar{c}_+^{(a)}(0)} \\ U_{-+}(T) &= \frac{\bar{c}_-^{(a)}(T)\bar{c}_-^{(b)}(0) - \bar{c}_-^{(b)}(T)\bar{c}_-^{(a)}(0)}{\bar{c}_+^{(a)}(0)\bar{c}_-^{(b)}(0) - \bar{c}_+^{(b)}(0)\bar{c}_-^{(a)}(0)} \\ U_{--}(T) &= \frac{\bar{c}_-^{(a)}(T)\bar{c}_+^{(b)}(0) - \bar{c}_-^{(b)}(T)\bar{c}_+^{(a)}(0)}{\bar{c}_-^{(a)}(0)\bar{c}_+^{(b)}(0) - \bar{c}_-^{(b)}(0)\bar{c}_+^{(a)}(0)} \end{aligned} \quad (\text{S33})$$

Using the relation between the motional amplitude and the amplitudes of the heterodyne signal (Eqs. 27 – 29), these expressions can be simplified to:

$$\begin{aligned} U_{++}(T) &= \left(\frac{A_{11}^{(a)}(T)A_{12}^{(b)}(0) - A_{11}^{(b)}(T)A_{12}^{(a)}(0)}{A_{11}^{(a)}(0)A_{12}^{(b)}(0) - A_{11}^{(b)}(0)A_{12}^{(a)}(0)} \right) \cdot \frac{u_{11}(0)}{u_{11}(T)} \\ U_{+-}(T) &= \left(\frac{A_{11}^{(a)}(T)A_{11}^{(b)}(0) - A_{11}^{(b)}(T)A_{11}^{(a)}(0)}{A_{12}^{(a)}(0)A_{11}^{(b)}(0) - A_{12}^{(b)}(0)A_{11}^{(a)}(0)} \right) \cdot \frac{u_{12}(0)}{u_{11}(T)} \end{aligned}$$

$$\begin{aligned}
U_{-+}(T) &= \left(\frac{A_{12}^{(a)}(T)A_{12}^{(b)}(0) - A_{12}^{(b)}(T)A_{12}^{(a)}(0)}{A_{11}^{(a)}(0)A_{12}^{(b)}(0) - A_{11}^{(b)}(0)A_{12}^{(a)}(0)} \right) \cdot \frac{u_{11}(0)}{u_{12}(T)} \\
U_{--}(T) &= \left(\frac{A_{12}^{(a)}(T)A_{11}^{(b)}(0) - A_{12}^{(b)}(T)A_{11}^{(a)}(0)}{A_{12}^{(a)}(0)A_{11}^{(b)}(0) - A_{12}^{(b)}(0)A_{11}^{(a)}(0)} \right) \cdot \frac{u_{12}(0)}{u_{12}(T)}
\end{aligned} \tag{S34}$$

where the $A_{ij}^{(k)}$ are the amplitudes of motion at $t = 0$ or $t = T$ returned by fitting the ringdown of the heterodyne signal (see §4.2) and the u_{ij} are given in Eq. S21.

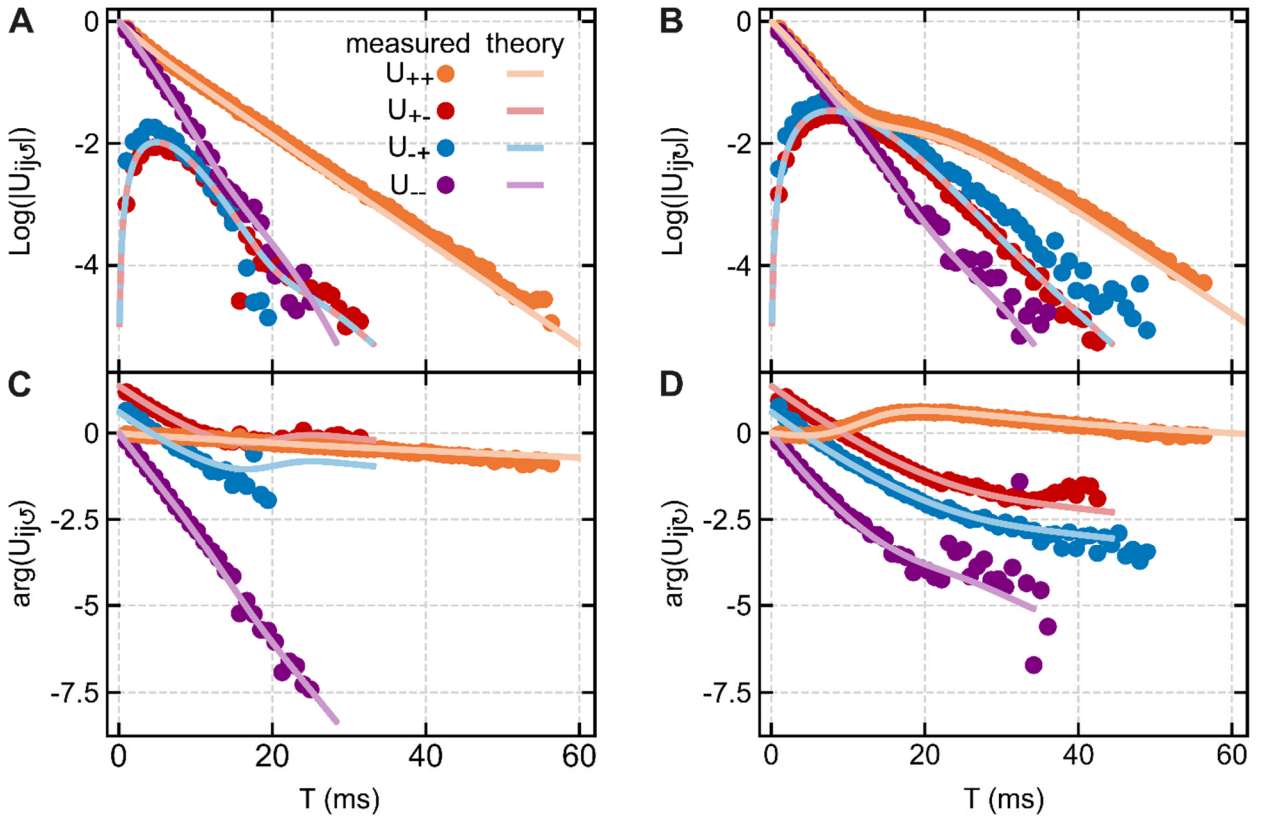


Figure S4: Measurements of the full propagator. The amplitude (A,B) and phase (C,D) of all four components of the propagator matrix $U(T)$ for the “simple” control loops with $P_1 = P_2 = 15 \mu W$, $\delta/2\pi = -1$ MHz, $\eta = -50$ Hz. Points: data, lines: no-free-parameters simulations. (A,C): The “forward” version of the loop, defined by $\theta_{12}(t) = 2\pi t/T$. (B,D): the “backward” version of the loop, defined by $\theta_{12}(t) = -2\pi t/T$. Data is shown only for $|U_{ii}(T)| > 5 \times 10^{-3}$.

Notably, the propagator matrix $U(T)$ depends only on the $A_{ij}^{(k)}$ and the choice of gauge for the eigenvectors that compose S_D^{-1} . Since the adiabatic theorem is only applicable to the mode with least loss (42), only the diagonal component corresponding to the least-damped mode (denoted by subscript + +) contains information about the geometric phase. For closed loops, we

choose $u_{ij}(0) = u_{ij}(T)$ (since $t = 0$ and $t = T$ correspond to the same point in parameter space), with the result that $U_{++}(T)$ and $U_{--}(T)$ (Eq. S34) are independent of the u_{ij} .

While only $U_{++}(T)$ is relevant to the main focus of this paper, for completeness Fig. S4 shows an example measurement of all four propagator matrix elements for control loops with $P_1 = P_2 = 15 \mu\text{W}$, $\delta/2\pi = -1 \text{ MHz}$, $\eta/2\pi = -50 \text{ Hz}$, and $\theta_{12}(t) = \pm 2\pi t/T$ (as also used in Fig. 2 of the main text). The off-diagonal elements $U_{+-}(T)$ and $U_{-+}(T)$ use the u_{ij} calculated from the optomechanical model, and in a gauge where $u_{ij} \in \mathbb{R}$.

The absence of an adiabatic limit for the more-damped mode is evident in the fact that $U_{--}(T) \ll U_{+-}(T)$ for large T . This is visible in data and theory Fig. S4B, and in the theory in Fig. S4A.

§5 The propagator matrix and the geometric phase

This section briefly summarizes some important features of the phase that is accumulated by a state when it is adiabatically transported. In particular, we review the representation of this phase as a power series in $1/T$; the impact of reversing the direction in which a given control path is traversed; and important features related to the definition of (real) phases modulo 2π .

§5.1 The asymptotic form of the accumulated phase

We start with a time dependent (potentially with non-zero trace) Hamiltonian $H(t)$ which is diagonalized by a time dependent change of basis $S_D(t)$, i.e. $H_D(t) = S_D^{-1}(t)H(t)S_D(t)$ where

$$H_D(t) = \begin{pmatrix} \lambda_+(t) & 0 \\ 0 & \lambda_-(t) \end{pmatrix}. \quad (\text{S35})$$

We require the column vectors of $S_D(t)$ to be normalized (see discussion in §7) and that $S_D(t)$ is T -periodic. In this diagonal basis, Eq. S8 becomes

$$i\epsilon \partial_s \vec{c}(s) = (H_D(s) - \epsilon \mathcal{A}(s)) \vec{c}(s) \quad (\text{S36})$$

where $s = t/T$, and we have defined $\epsilon = 1/T$ and $\mathcal{A}_{ij} = \vec{\xi}_i(s) \cdot i \partial_s \vec{\psi}_j(s)$ for $i, j = +, -$ where $\vec{\xi}_i$ and $\vec{\psi}_j$ are the left- and right-eigenvectors of H , respectively.

Now, consider a closed path through the space of Hamiltonian parameters where $\text{Im}[\lambda_+(s)] < \text{Im}[\lambda_-(s)]$ for all $s \in [0,1]$, i.e., $\vec{\psi}_+(s)$ decays more slowly than $\vec{\psi}_-(s)$. The adiabatic theorem for non-Hermitian Hamiltonians then guarantees that if a state is initialized in $\vec{\psi}_+(0)$ it will remain in $\vec{\psi}_+(s)$ for all $s \in [0,1]$ as $\epsilon \rightarrow 0$ (42). Therefore, as $\epsilon \rightarrow 0$, we may use time-independent perturbation theory to find the eigenvalue $\lambda'_+(s)$ of $H_D(s) - \epsilon \mathcal{A}(s)$ at every s . Note that $\lambda'_+(s) \rightarrow \lambda_+(s)$ as $\epsilon \rightarrow 0$. In this case, the phase accumulated by a state vector

$\vec{c}(T) = e^{-i\phi_{\mathcal{U}}}\vec{c}(0)$ (with $\vec{c}(0) = \vec{\Psi}_+$) can be expressed as a power series in ϵ :

$$\begin{aligned}\phi_{\mathcal{U}} &= \frac{1}{\epsilon} \int_0^1 ds \lambda'_+(s) \\ &= \int_0^1 ds \left[(1/\epsilon)\lambda_+(s) - i\vec{\xi}_+(s) \cdot \partial_s \vec{\Psi}_+(s) \right. \\ &\quad \left. - \epsilon \frac{(\vec{\xi}_-(s) \cdot \partial_s \vec{\Psi}_+(s))(\vec{\xi}_+(s) \cdot \partial_s \vec{\Psi}_-(s))}{\lambda_+(s) - \lambda_-(s)} + \mathcal{O}(\epsilon^2) \right].\end{aligned}\tag{S37}$$

The first term in this expression is the dynamical phase ϕ_D ; the second term is the geometric phase ϕ_B ; and the subsequent terms approach 0 in the adiabatic limit $\epsilon \rightarrow 0$. In general, the N^{th} term is proportional to ϵ^{N-2} and to a sum of products involving $N - 1$ components of \mathcal{A}_{ij} (i.e., containing $N - 1$ derivatives).

To consider the phase $\phi_{\mathcal{V}}$ accumulated by a time reversed loop, replace $\vec{\Psi}_i(s), \vec{\xi}_i(s), \lambda_i(s)$ respectively by $\vec{\Psi}_i(1 - s), \vec{\xi}_i(1 - s), \lambda_i(1 - s)$ in the preceding formulae. In each term, each derivative acquires a factor (-1) but otherwise is unchanged. Thus, the *odd* order (in ϵ) terms of $\phi_{\mathcal{V}}$ will be equal to the corresponding terms of $\phi_{\mathcal{U}}$, while the *even* order terms of $\phi_{\mathcal{V}}$ will be equal to the corresponding terms of $\phi_{\mathcal{U}}$ multiplied by -1 .

As a result, in the large T limit we may write the phases accumulated along each direction of a control path as

$$\phi_{\mathcal{U}} = 2\pi n_{\mathcal{U}} + q_D T - \phi_B + \frac{q_1}{T} + \frac{q_2}{T^2} + \mathcal{O}(T^{-3})\tag{S38}$$

$$\phi_{\mathcal{V}} = 2\pi n_{\mathcal{V}} + q_D T + \phi_B + \frac{q_1}{T} - \frac{q_2}{T^2} + \mathcal{O}(T^{-3})\tag{S39}$$

In these expressions, $n_{\mathcal{U}}$ and $n_{\mathcal{V}}$ are arbitrary integers, reflecting the fact that phases are defined modulo 2π . Equivalently, the choice of $n_{\mathcal{U},\mathcal{V}}$ corresponds to the choice of a branch of the logarithm in $\tilde{\phi}(T) = -i\log(U_{++}(T))$. We describe our convention for this choice in the following.

The quantity $\beta(T) = (\phi_{\mathcal{V}} - \phi_{\mathcal{U}})/2$ contains only terms of even order in ϵ (and hence in T). The first three terms in the large- T (small- ϵ) expansion of $\beta(T)$ are of the form

$$\beta(T) = \pi(n_{\mathcal{V}} - n_{\mathcal{U}}) + \phi_B - \frac{q_2}{T^2} + \mathcal{O}(T^{-4})\tag{S40}$$

Ignoring the first term, this is the fit function used to determine ϕ_B from the data (as described in the main text, cf. Fig. 2F) using the complex coefficients q_2 and ϕ_B as fit parameters. This shows that without further processing, ϕ_B can only be estimated modulo π from $\beta(T)$.

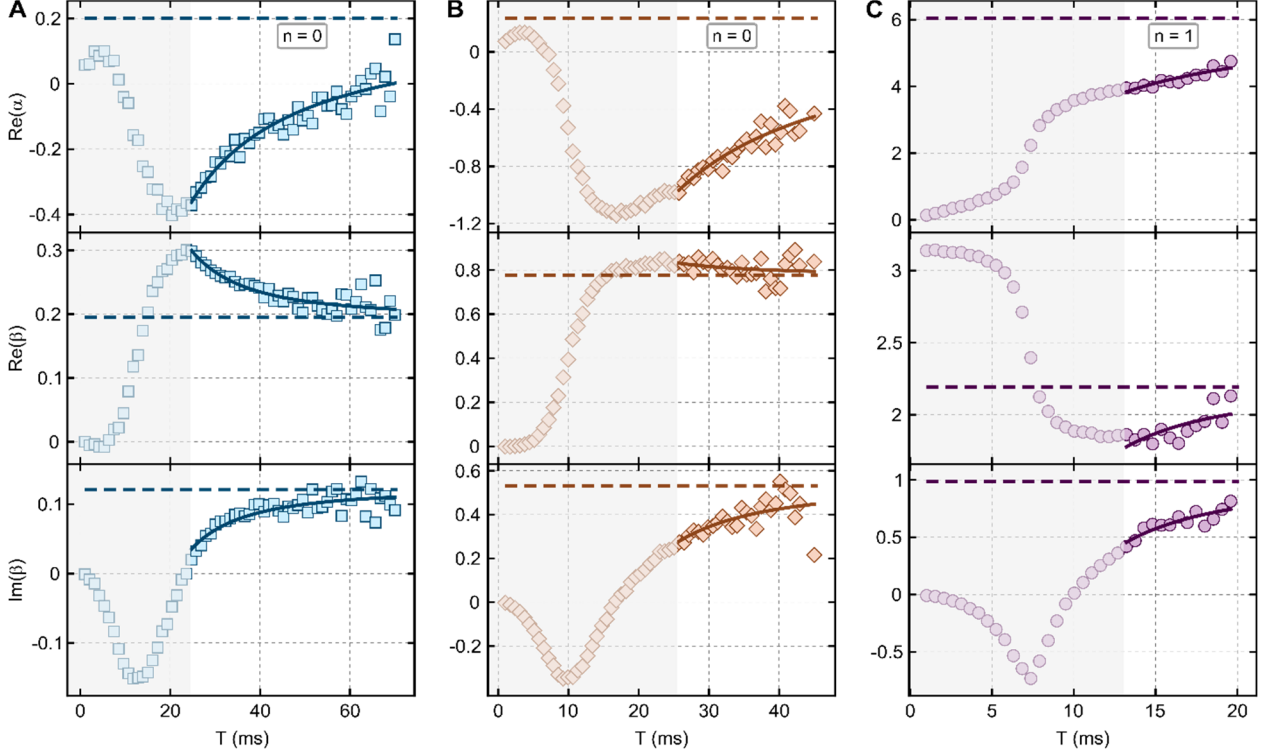


Figure S5: Examples of fits to the asymptotic behavior of $Re(\alpha(T))$ and $\beta(T)$, and the determination of ϕ_B . Shaded region: data excluded from the fit. **(A)** An example of a measurement in which 2/3 of the data was included in the fit. This is Option (3) of §5.2. **(B)** An example of a measurement in which data were excluded for $T < 8/(|\lambda_+ - \lambda_-|)$. This is Option (1) of §5.2. **(C)** An example of a measurement in which 1/3 of the data was included in the fit. This is Option (2) of §5.2. Top row: $Re(\alpha(T))$, Middle and bottom rows: $Re(\beta(T))$ and $Im(\beta(T))$ respectively. Points: data, solid curve: fit, dashed line: fitted asymptote, which is used to calculate ϕ_B . For $Re(\alpha(T))$, this asymptote is binned to determine the integer n (Fig. S6). The data in panels A, B, C were taken for control loops with $(P, \delta, \eta) = (17.5 \mu\text{W}, -1.5 \text{ MHz}, -50 \text{ Hz})$, $(17.5 \mu\text{W}, -0.75 \text{ MHz}, -50 \text{ Hz})$, $(20 \mu\text{W}, -0.25 \text{ MHz}, -50 \text{ Hz})$ respectively. All of these control loops used $\theta_{12}(t) = \pm 2\pi t/T$.

However, ϕ_B may be determined modulo 2π by inspecting the quantity $\alpha(T) = \phi_U + \phi_S$, which contains only terms of odd order in T :

$$Re(\alpha(T)) = 2\pi(n_U + n_S) + 2Re(q_D)T + \frac{2q_1}{T} + \mathcal{O}(T^{-3}) \quad (\text{S41})$$

For every data set that we use to determine $\beta(T)$, we also determine $\alpha(T)$. We then fit $Re(\alpha(T))$ at large T to $q_0 + 2Re(q_D)T + 2q_1/T$ where q_0 and q_1 are real fitting parameter (and

$q_D = -\int_0^1 ds \lambda_+(s)$ is known). The measured $\text{Re}(\alpha(T))$ and the corresponding fits are shown in the top row of Fig. S5.

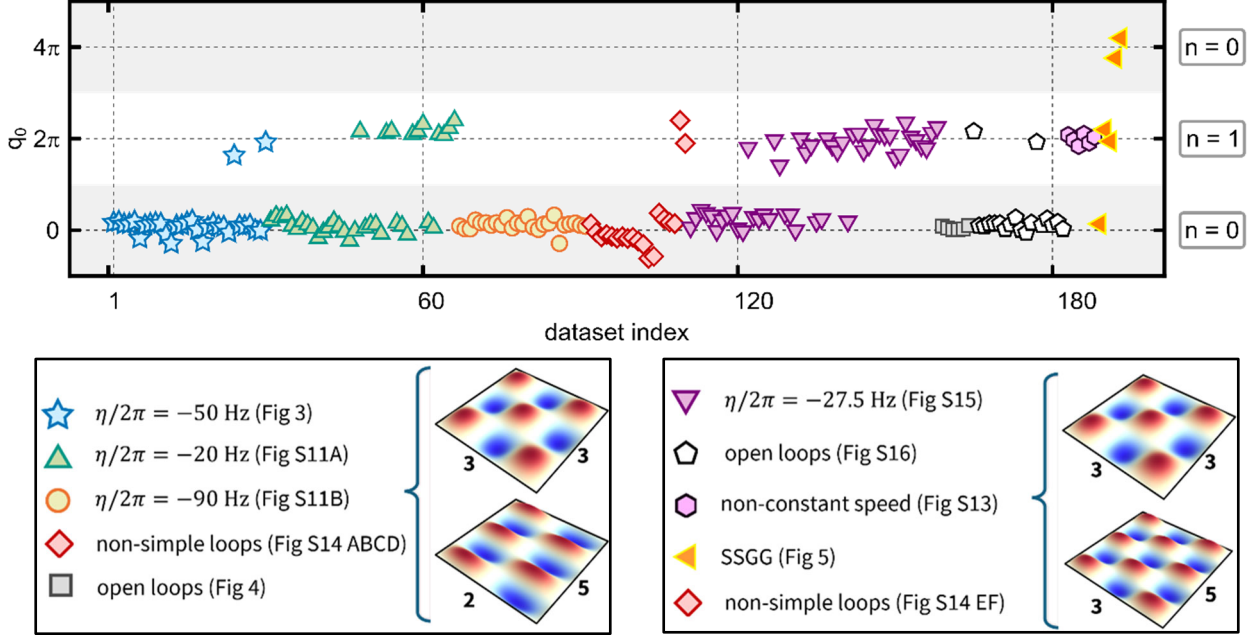


Figure S6: Upper panel: the real part of the fit parameter q_0 . This quantity is used to determine the integer n in §5.1. Specifically, we take $n = 0$ for $-\pi < q_0 \leq \pi$ and $3\pi < q_0 \leq 5\pi$ (the gray bands) and $n = 1$ for $\pi < q_0 \leq 3\pi$. Lower panels: the legend for the upper panel. Indicating which pair of membrane modes was used, the value of η , and whether the data was taken with simple or non-simple loops

Rounding the best-fit value of $q_0/2\pi$ to the nearest integer then provides $(n_{\mathcal{V}} + n_{\mathcal{U}})$. Since $(n_{\mathcal{V}} + n_{\mathcal{U}})$ and $(n_{\mathcal{V}} - n_{\mathcal{U}})$ have the same parity, we define $n = (n_{\mathcal{V}} + n_{\mathcal{U}}) \bmod 2$. All values of the complex Berry phase ϕ_B shown here are equal to πn plus the T -independent fit coefficient of $\beta(T)$.

Figure S6 shows the best-fit value of q_0 resulting from fitting $\text{Re}(\alpha(T))$ for every measurement in this manuscript. As described in §5.1, these values are binned into $n = 0$ (for $-\pi < q_0 \leq \pi$ and $-3\pi < q_0 \leq 5$, gray regions) or $n = 1$ ($3\pi < q_0 \leq 5\pi$, white region).

§5.2 Determining the large- T asymptote of the data

For the power series expansions described above to be valid, the data used for fitting must be sufficiently far into the adiabatic regime (corresponding to large T). However, for most control loops \mathcal{C} , the membrane's motion decays. In practice this sets an upper limit to T (beyond which the membrane's motion is indistinguishable from its thermal fluctuations) which we denote T_{SNR} . The value of T_{SNR} depends upon \mathcal{C} , as the normal modes' decay rate depends upon the control tones' powers and detuning.

To address this, for each \mathcal{C} we perform the asymptotic fits to $\alpha(T)$ and $\beta(T)$ for $T_{\text{min}} <$

$T < T_{\text{SNR}}$ using one of three possible options for T_{min} :

Option (1): $T_{\text{min}} = 8(|\lambda_+ - \lambda_-|)^{-1}$. Here, $(|\lambda_+ - \lambda_-|)^{-1}$ is a typical time scale associated with adiabaticity in non-Hermitian systems.

Option (2): For those \mathcal{C} in which Option (1) leaves insufficient data for the asymptotic fit, we instead use $T_{\text{min}} = \frac{2}{3}T_{\text{SNR}}$.

Option (3): For those \mathcal{C} in which Option (1) results in $T_{\text{min}} < \frac{1}{3}T_{\text{SNR}}$, we instead use $T_{\text{min}} = \frac{1}{3}T_{\text{SNR}}$.

Examples of these fits are shown in Fig. S5. In Fig. S5A the fits use Option (3); in Fig. S5B the fits use Option (1), and in Fig. S5C they use Option (2).

§6 Calculating the geometric phase

This section reviews the calculation of the geometric phase ϕ_{B} , both for cases in which there are simple analytic expressions, and for which it must be evaluated numerically. We also describe an easily visualizable relationship between ϕ_{B} and the shape of the “simple” control loops pictured in main text Fig. 2B.

§6.1 Geometric phase for “simple” control loops

The eigenvalues of the traceless part of H (see Eq S13) are $\lambda_{\pm} = \pm\sqrt{L^2 + MN}$, and the corresponding right (left) eigenvectors $\vec{\Psi}_{\pm}(\vec{\xi}_{\pm})$ are, up to an overall complex scaling factor, given by

$$\vec{\Psi}_{\pm} = \begin{pmatrix} Me^{i\theta_{12}} \\ \pm\lambda - L \end{pmatrix}, \quad (\text{S42})$$

$$\vec{\xi}_{\pm} = \pm \frac{1}{2\lambda Me^{i\theta_{12}}} \begin{pmatrix} \pm\lambda + L \\ Me^{i\theta_{12}} \end{pmatrix}. \quad (\text{S43})$$

Note that this choice of eigenvectors satisfies the normalization condition $\vec{\xi}_i \cdot \vec{\Psi}_j = \delta_{ij}$ (the dot product between two vectors is defined as $\vec{v} \cdot \vec{w} = v_1 w_1 + v_2 w_2$). For the “simple” control loops considered in the main text (which correspond to main text Fig. 2B), we only need consider the Berry connection along the θ_{12} direction of parameter space, which may be readily computed to be (2,32)

$$\mathcal{A}_{\pm, \theta_{12}} = i \vec{\xi}_{\pm} \cdot \partial_{\theta_{12}} \vec{\Psi}_{\pm} = -\frac{1}{2}(1 \pm L/\lambda) \quad (\text{S44})$$

and the geometric phase for a circuit in which we ramp $\theta_{12}: 0 \rightarrow x$ is simply given by

$$\Phi_{B, \pm} = \int_0^x d\theta_{12} \mathcal{A}_{\pm, \theta_{12}} = -\frac{x}{2}(1 \pm L/\lambda) \quad (\text{S45})$$

i.e. the accumulated geometric phase is proportional to the integrated change in the beatnote phase. For a complete phase winding $\theta_{12}: 0 \rightarrow 2\pi$, we have

$$\Phi_{B, \pm} = -\pi(1 \pm L/\lambda) = \pm \pi(1 - L/\lambda) \quad (\text{S46})$$

where in the last equality we have used the fact that $\Phi_{B, \pm}$ is defined mod 2π . Note that here, the eigenvector $\vec{\Psi}_{\pm}$ need not refer to the least-damped eigenmode. Indeed, we have made no choice of the principal branch of λ in the derivation above. In practice, we choose $+\lambda$ to be the eigenvalue with the largest imaginary component, which draws analogy to the Hermitian case in the limit $\text{Im}(\lambda) \rightarrow 0$. For all data presented in this manuscript, this also fixes $+\lambda$ as the eigenvalue of the least-damped mode, and so for notational simplicity we define $\Phi_B \equiv \Phi_{B, +}$.

§6.2 Geometric intuition for the complex Berry phase

The parameterization of H in terms of L, M, N, θ_{12} is convenient for computing the geometric phase accumulated in most of the experiments presented here, and in particular for the “simple” control loops illustrated in main text Fig. 2B. However, when considering more general loops it can be convenient to parameterize H (up to its trace) in complex spherical coordinates (56)

$$H = \lambda \begin{pmatrix} \cos(\nu) & \sin(\nu) e^{-i\theta} \\ \sin(\nu) e^{i\theta} & -\cos(\nu) \end{pmatrix} = \vec{B} \cdot \vec{\sigma} \quad (\text{S47})$$

$$\vec{B} = \lambda \begin{pmatrix} \sin(\nu) \cos(\theta) \\ \sin(\nu) \sin(\theta) \\ \cos(\nu) \end{pmatrix} \quad (\text{S48})$$

with $\lambda, \theta, \nu \in \mathbb{C}$. In these coordinates, the eigenvalues are $\pm\lambda$, and the corresponding eigenvectors are given by

$$\begin{aligned}\vec{\Psi}_+ &= \begin{pmatrix} \cos(\nu/2) \\ \sin(\nu/2)e^{i\theta} \end{pmatrix}, \vec{\Psi}_- = \begin{pmatrix} \sin(\nu/2)e^{-i\theta} \\ -\cos(\nu/2) \end{pmatrix}, \\ \vec{\xi}_+ &= \begin{pmatrix} \cos(\nu/2) \\ \sin(\nu/2)e^{-i\theta} \end{pmatrix}, \vec{\xi}_- = \begin{pmatrix} \sin(\nu/2)e^{i\theta} \\ -\cos(\nu/2) \end{pmatrix}.\end{aligned}\tag{S49}$$

The Berry connection may be readily computed to be

$$\vec{\mathcal{A}}_{\pm} = i\vec{\xi}_{\pm} \cdot \nabla \vec{\Psi}_{\pm} = \mp \frac{1}{2}(1 - \cos(\nu))\hat{\theta}.\tag{S50}$$

Note that the Berry connection $\vec{\mathcal{A}}_{\pm}$ is a vector in Hamiltonian parameter space, and ∇ is the gradient operator in this space. Thus, when considering a generic path in parameter space, we need only to consider the projection of the path to the complex θ plane.

For the loops considered in the main text, the experimental parameter θ_{12} maps onto $-\text{Re}(\theta)$, meaning that only the real part of θ is varied by 2π . In practice, the Hamiltonians accessible in these measurements have $\text{Im}[\theta] \approx 0$, and thus for the remainder of this discussion we consider $\theta = -\theta_{12} \in \mathbb{R}$ (though the results remain unchanged for a closed circuit through arbitrary complex θ). Thus, for the paths considered in the main text, we have (for the least-damped mode):

$$\begin{aligned}\phi_B &= \int_0^{2\pi} d\theta_{12} \mathcal{A}_{+, \theta_{12}} = \pi(1 - \cos(\nu)) \\ &= \pi(1 - \cos(\nu_{\text{re}})\cosh(\nu_{\text{im}}) + i\sin(\nu_{\text{re}})\sinh(\nu_{\text{im}}))\end{aligned}\tag{S51}$$

where we have written $\nu = \nu_{\text{re}} + i\nu_{\text{im}}$. It was noted in Ref. (32) that the line integral of $\vec{\mathcal{A}}_{\pm}$ over a closed circuit \mathcal{C} may be converted, via Stokes' theorem, into the surface integral of a curvature over the area bounded by \mathcal{C} . Indeed, in complete analogy to the Hermitian Berry curvature, this curvature may be written (in \mathbb{C}^3) as the field strength tensor associated with a ‘‘magnetic field’’:

$$\vec{R}_{\pm} = \mp \frac{\vec{B}}{2B^3}\tag{S52}$$

where \vec{B} is the complex vector defined above (see Ref. (56)), Eq. 45). Therefore, the complex

geometric phase can be interpreted as a flux enclosed by \mathcal{C} in the presence of a “magnetic monopole” that is located at $\vec{B} \cdot \vec{B} = 0$ (i.e., where H is degenerate).

In spite of this algebraic analogy between the Hermitian and non-Hermitian case, there are also important differences. In the Hermitian case, the space of \vec{B} is \mathbb{R}^3 , with the only degeneracy occurring at the point $\vec{B} = 0$. However, in the non-Hermitian case the space of \vec{B} is six (real) dimensional and the degeneracy (i.e., $\vec{B} \cdot \vec{B} = 0$) occurs in a four-dimensional subspace, making the relationship between \mathcal{C} and ϕ_B challenging to visualize.

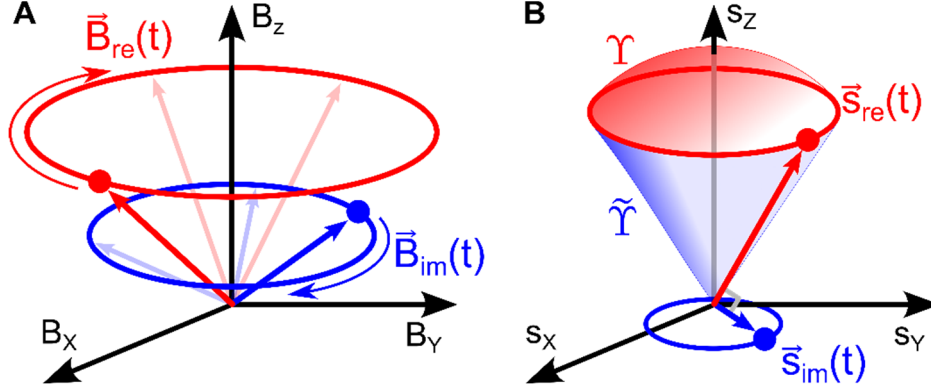


Figure S7: Two ways of visualizing “simple” control loops. **(A)** In terms of a real magnetic field and an imaginary magnetic fields, as in Fig. 2B of the main text. **(B)** In terms of the vectors \vec{s}_{re} and \vec{s}_{im} .

We may visualize the situation by decomposing

$$\vec{B}/\lambda = \cosh(v_{im}) \begin{pmatrix} \sin(v_{re})\cos(\theta) \\ \sin(v_{re})\sin(\theta) \\ \cos(v_{re}) \end{pmatrix} + i\sinh(v_{im}) \begin{pmatrix} \cos(v_{re})\cos(\theta) \\ \cos(v_{re})\sin(\theta) \\ -\sin(v_{re}) \end{pmatrix} = \vec{s}_{re} + i\vec{s}_{im} \quad (\text{S53})$$

where \vec{s}_{re} and \vec{s}_{im} are vectors in \mathbb{R}^3 . It may be readily verified that $\vec{s}_{re} \cdot \vec{s}_{im} = 0$. For loops of the type shown in Fig. 2B and in the limit $|\vec{B}_{im}| \ll |\vec{B}_{re}|$ (i.e. $v_{im} \ll 1$) which is relevant for many of the measurements in this manuscript, the real component of the geometric phase

$$\text{Re}(\phi_B) = \pi(1 - \cos(v_{re})) + \mathcal{O}(v_{im}^2) = \frac{\Upsilon}{2} + \mathcal{O}(v_{im}^2) \quad (\text{S54})$$

is approximately equal to one-half the solid angle Υ subtended by the \vec{s}_{re} vector – a result familiar from the Hermitian case.

In addition, by noting that $|\vec{s}_{re}| = \cosh(v_{im}) = 1 + \mathcal{O}(v_{im}^2)$ and $|\vec{s}_{im}| = |\sinh(v_{im})| =$

$|v_{\text{im}}| + \mathcal{O}(v_{\text{im}}^3)$, we see that area of the mantle of the cone (see Fig. S7B) swept out by \vec{s}_{re} is $\tilde{Y} = \pi \sin(v_{\text{re}}) + \mathcal{O}(v_{\text{im}}^2)$, and thus

$$\text{Im}(\phi_{\text{B}}) = \pi(\sin(v_{\text{re}})\sinh(v_{\text{im}})) = \tilde{Y}|\vec{s}_{\text{im}}| + \mathcal{O}(v_{\text{im}}^2). \quad (\text{S55})$$

In the limit of $v \in \mathbb{R}$, (i.e. $|\vec{s}_{\text{im}}| = 0$) this reduces to the standard (real) Hermitian Berry phase, even for Hamiltonians with complex λ .

§6.3 Numerical method for calculating the geometric phase

For “non-simple” control loops (i.e., not corresponding to Fig. 2B) there is no simple expression for ϕ_{B} , so we calculate it numerically as follows. First, we discretize the loop into N equal steps, each starting at $s_k = k/N$ with $k = 0, 1, 2, \dots, N$. In analogy to the Hermitian case (Eq. 4 in Ref. (57)), the non-Hermitian ϕ_{B} can then be expressed as

$$\phi_{\text{B},\pm} \approx -i \log \left(\prod_{k=0}^{N-1} \vec{\xi}_{\pm}(s_{k+1}) \cdot \vec{\Psi}_{\pm}(s_k) \right). \quad (\text{S56})$$

Thus, we calculate the geometric phase by computing the left and right eigenvectors at each step s_k (while ensuring there is a consistent choice of gauge between all N steps) and multiplying the chain of inner products above. For closed loops, this formulation is invariant to gauge choice, as $\vec{\Psi}_{\pm} \rightarrow e^{i\alpha}\vec{\Psi}_{\pm}$ and $\vec{\xi}_{\pm} \rightarrow e^{-i\alpha}\vec{\xi}_{\pm}$ for all $\alpha \in \mathbb{R}$. The calculations presented here use $N = 20,000$.

§7 Gauge-invariance of the imaginary part of the Berry connection

Figure 4 shows measurements of the imaginary component of the geometric phase for open paths (i.e. paths that do not start and end at the same point in parameter space). In this section, we show that the imaginary part of the Berry connection is gauge invariant, from which it follows that the imaginary part of the geometric phase is also gauge independent, regardless of whether or not the path is closed. This discussion is similar to that of Ref. (2).

To begin, consider a choice of right and left eigenvectors $\vec{\Psi}_{1,2}, \vec{\xi}_{1,2}$ that obey the joint normalization condition:

$$\vec{\xi}_i \cdot \vec{\Psi}_j = \delta_{ij} \quad (\text{S57})$$

An arbitrary state \vec{d} may be decomposed as $\vec{d} = d_1\vec{\Psi}_1 + d_2\vec{\Psi}_2$ with complex coefficients $d_{1,2} =$

$\vec{\xi}_{1,2} \cdot \vec{d}$. In this case, a state \vec{d} that is proportional to the eigenmode $\vec{\Psi}_i$ has population $|d_i|^2$.

Now, consider a different choice of right eigenvectors $\vec{\Psi}'_{1,2} = x_{1,2} \vec{\Psi}_{1,2}$ with nonzero constants $x_{1,2}$. To satisfy the normalization condition above, the corresponding left eigenvectors must be $\vec{\xi}'_{1,2} = \vec{\xi}_{1,2}/x_{1,2}$. However, upon making this choice, the population of \vec{d} in eigenmode $\vec{\Psi}'_i$ is

$$|d'_i|^2 = |\vec{\xi}'_i \cdot \vec{d}|^2 = \left| \frac{\vec{\xi}_i}{x_i} \cdot \vec{d} \right|^2 = |d_i|^2 / |x_i|^2 \quad (\text{S58})$$

i.e. the population depends explicitly on $|x_i|$. Since the population of a mode encodes an absolute physical quantity (in this case, it is proportional to the energy stored in the oscillator), it must be independent of the choice of gauge (i.e. the choice of $\vec{\Psi}_{1,2}, \vec{\xi}_{1,2}$). This is ensured by imposing an additional normalization condition:

$$|\vec{\Psi}_{1,2}^* \cdot \vec{\Psi}_{1,2}|^2 = 1 \quad (\text{S59})$$

Thus, any choice of right eigenvectors (i.e. choice of gauge) obeys $\vec{\Psi}'_{1,2} = x_{1,2} \vec{\Psi}_{1,2}$, with $|x_i| = 1$. Put another way, to preserve the gauge independence of populations, the only allowed gauge transformations of right eigenmodes $\vec{\Psi}_{1,2}$ are unitary complex numbers, just as in the Hermitian case.

Under such gauge transformations, the real part of the Berry connection $\mathcal{A}_i = \vec{\xi}_i(s) \cdot i \partial_s \vec{\Psi}_i(s)$ changes, but the imaginary part does not. It follows that the imaginary component of the geometric phase is gauge invariant for any path (including open ones). When calculating the eigenvector amplitudes \bar{c}_i from ringdown measurements (at both the beginning and the end of the circuit), the normalized eigenvectors that we use to construct S_D (Eq. S19) satisfies this restriction.

§8 Steady-state geometric gain

This section discusses two main points: the definition of SSGG, and the range of parameters over which it can be realized. To emphasize the broad applicability of SSGG, these questions are addressed in terms of a generic two-mode non-Hermitian system, rather than for any specific realization¹.

¹ This discussion can be translated directly to the present optomechanical device via Eq. S13 *et sequentia*.

§8.1 Defining SSGG

Figure 5 of the main text shows that a collection of linear, lossy elements can produce continuous gain if the elements' parameters are varied slowly. While the flow of energy into or out of a system with a time-dependent Hamiltonian can be conceptualized in various ways, the behavior described here is conveniently described in terms of the complex geometric phase. We refer to this mechanism as steady-state geometric gain (SSGG). Here we provide a concrete platform-independent definition of SSGG.

To focus the discussion, we consider systems that consist of two harmonic modes whose parameters are repeatedly tuned around a control loop \mathcal{C}_{amp} , with each traversal using the same time dependence $s(t/T)$ and the same duration T . It is straightforward to generalize the concept of SSGG to a larger number of modes and to more complicated control paths.

We take the following four conditions as defining SSGG:

- (1) There is a mode that is the least-damped mode for all of \mathcal{C}_{amp} .
- (2) When the system is prepared in this least-damped mode, its state after a single traversal of \mathcal{C}_{amp} using $s(t/T)$ with duration T is well-approximated as the initial state multiplied by $e^{-i\phi(T)}$ where the complex phase $\phi(T)$ is given by Eq. 2.
- (3) For each such traversal, this mode's dynamical phase contributes loss: $\text{Im}(\phi_D) < 0$.
- (4) For each such traversal, this mode's total gain $\text{Im}[\phi(T)]$ lies in Γ , the shaded region of Figure S8.

When Condition (1) is met, the adiabatic theorem (42) guarantees that Condition (2) is also met for sufficiently large T . We take $T > T_{\text{ad}}$ as the threshold for this condition, where $T_{\text{ad}} = \max_c (|\lambda_+(s) - \lambda_-(s)|^{-1})$.

Condition (3) requires that the system's dynamical phase contributes loss. This condition is included because otherwise the system can serve as steady-state amplifier without the geometric phase (i.e., just by using large T and relying on the dynamical phase).

Condition (4) identifies the features that $\text{Im}(\phi(T))$ must exhibit (upon a single traversal of \mathcal{C}_{amp} using time dependence s and duration T) for the system's gain to be attributed to the geometric phase. These are:

- (4a) $T > T_{\text{ad}}$
- (4b) $\text{Im}[\phi(T)] > 0$
- (4c) $\text{Im}[\phi(T)] < -\text{Im}(\phi_B)$
- (4d) $\text{Im}[\phi(T)] < \text{Im}(\phi_D) - 2\text{Im}(\phi_B)$

Each of the Conditions (4a – 4d) has a straightforward physical interpretation.

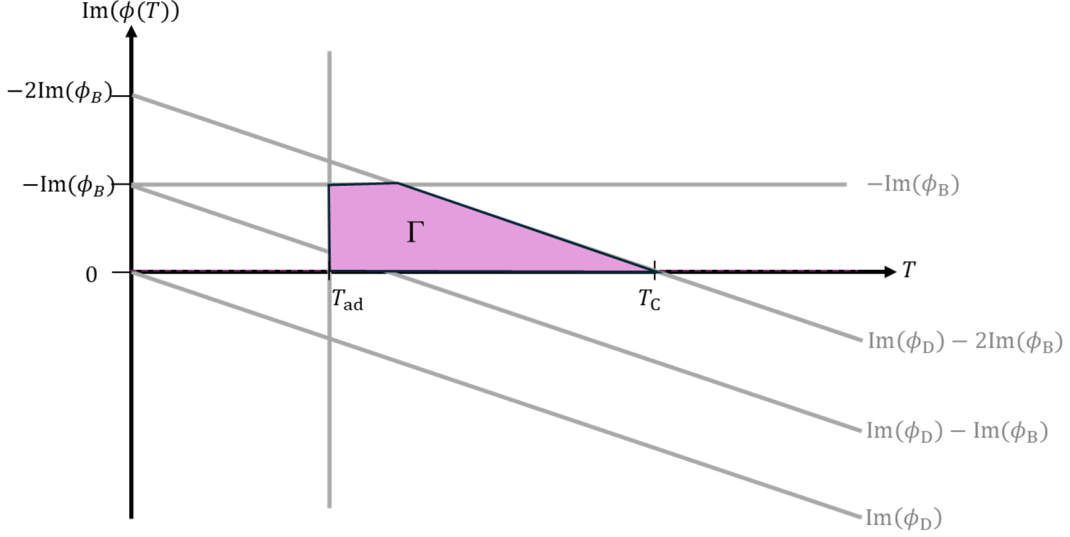


Fig. S8: The conditions for achieving steady-state geometric gain (SSGG). For a given control loop \mathcal{C}_{amp} time dependence s , and loop duration T , SSGG occurs if $\text{Im}[\phi(T)]$ lies in the shaded region Γ .

Condition (4a) ensures that the system's dynamics are compatible with the notion of adiabaticity, and hence are described by Eq. 2.

Condition (4b) ensures that the mode experiences net gain upon each traversal of \mathcal{C}_{amp} .

Conditions (4c) and (4d) ensure that the net gain can be attributed to the geometric gain. Specifically, Condition (4c) requires that the net gain would be negative without the contribution from the geometric gain. Condition (4d) requires that the geometric gain accounts for the majority of the difference between the dynamical loss $\text{Im}(\phi_D)$ and the net gain; this ensures that the net gain is not attributable to the higher-order terms [i.e., $\mathcal{O}(T^{-1})$] in Eq. 2.

For a given \mathcal{C}_{amp} and s , Conditions (4a – 4d) can be visualized by noting that they each bisect the plane spanned by $\text{Im}[\phi(T)]$ and T (Fig. S8, dashed lines). Together, they define a region (Γ) with the following interpretation: for this \mathcal{C}_{amp} and $s(t/T)$, SSGG results if and only if T is chosen so that $\text{Im}[\phi(T)]$ lies within Γ .

§8.2 Identifying control loops that produce SSGG

Conditions (1 – 3) depend only on the “static” or “instantaneous” properties of the system (e.g., its eigenvalues at each value of s). As a result, for a given physical system and control loop, it is relatively straightforward to determine whether they are satisfied.

In contrast, Condition (4) depends on the system's dynamics as governed by Eq. 1. For a specific \mathcal{C}_{amp} and s , numerical integration of Eq. 1 (for various choices of T) can be used to determine whether or not $\text{Im}[\phi(T)]$ passes through Γ . In practice, this approach was used to identify the \mathcal{C}_{amp} used in Fig. 5 of the main paper.

In addition to explicit numerical integration, it would be helpful to also have a simple criteria that could be used to identify which \mathcal{C}_{amp} and s can produce SSGG. As a practical

matter, this would facilitate the design of SSGG devices. More abstractly, it could also provide a useful measure of how common such loops are.

We are not aware of any simple criteria that determines whether an arbitrary \mathcal{C}_{amp} and s can meet Condition (4). However, we can instead consider particular families of loops that are parameterized by a few variables, and determine the range of these variables that satisfy Condition (4). In §8.3 and §8.4 we consider two such families, and find that in both cases a wide range of loops satisfy Condition (4).

§8.3 SSGG with simple loops

In this section we consider a class of loops for which Eq. 1 has an analytic solution, and we show that this solution gives analytic expressions for the loops that satisfy Conditions (1 – 4). Specifically, we consider the “simple” loops of Fig. 2B, for which H can be written as:

$$H(t) = \begin{pmatrix} \mathcal{T} + L & M e^{-2\pi i t/T} \\ N e^{2\pi i t/T} & \mathcal{T} - L \end{pmatrix} \quad (\text{S60})$$

where \mathcal{T} , M , N , and L are complex constants.

For $H(t)$ of this form, the eigenvalues are time-independent and are given by $\lambda_{\pm} = \mathcal{T} \pm \lambda_0$, where $\lambda_0 = \sqrt{L^2 - MN}$. Since we are interested in the less-damped mode, we take $\text{Im}(\lambda_0) \geq 0$. In this discussion, the trace \mathcal{T} plays an important role, as its imaginary part contributes to the system’s loss (in particular, to $\text{Im}(\phi_D)$).

Solving Eq. 1 with $H(t)$ of this form gives

$$\phi(T) = \mathcal{T}T + \sqrt{\lambda_0^2 T^2 - 2\pi L T + \pi^2} - \pi \quad (\text{S61})$$

It is straightforward to show that in the $T \rightarrow \infty$ limit, $\phi(T) \rightarrow \phi_D - \phi_B$, where $\phi_D = q_D T = (\mathcal{T} + \lambda_0)T$ and $\phi_B = \pi \left(\frac{L}{\lambda_0} + 1 \right)$.

These loops always meet Condition (1), and always meet Condition (2) in the large- T limit. Meeting Condition (3) amounts to the simple constraint $\text{Im}(\mathcal{T} + \lambda_0) < 0$. As a result, identifying the loops that can produce SSGG amounts to finding the values of \mathcal{T} , λ_0 , and L that meet Condition (4).

Condition (4) requires that the function $\text{Im}(\phi(T))$ passes through Γ , which in turn requires that $\text{Im}(\phi(T))$ intersects² at least one of the boundaries of Γ . Here we derive an analytic

² This intersection must be non-tangential.

expression for the loops that intersect the lower boundary of Γ . Similar expressions can be derived for the other boundaries of Γ .

$\text{Im}(\phi(T))$ intersects the lower boundary of Γ if there is a loop duration T_* such that the following two conditions hold:

$$(A) \quad T_{\text{ad}} < T_* < T_c$$

$$(B) \quad \text{Im}(\phi(T_*)) = 0$$

where $T_c = 2\text{Im}(\phi_B)/\text{Im}(q_D)$.

Considering (B) first, we rewrite it as

$$\text{Im}(\phi(T_*)) = 0 \tag{S62}$$

$$\text{Im}\left(\mathcal{J}T_* + \sqrt{\lambda_0^2 T_*^2 - 2\pi L T_* + \pi^2 - \pi}\right) = 0 \tag{S63}$$

$$\text{Im}\left(\sqrt{\lambda_0^2 T_*^2 - 2\pi L T_* + \pi^2}\right) = \text{Im}(-\mathcal{J}T_*) \tag{S64}$$

$$\sqrt{\lambda_0^2 T_*^2 - 2\pi L T_* + \pi^2} = -\mathcal{J}T_* + r \tag{S65}$$

where r is a real number. This is equivalent to:

$$\lambda_0^2 T_*^2 - 2\pi L T_* + \pi^2 = \mathcal{J}^2 T_*^2 - 2\mathcal{J}T_* r + r^2 \tag{S66}$$

The imaginary part of Eq. S66 is

$$T_*^2 \text{Im}(\lambda_0^2 - \mathcal{J}^2) - 2\pi T_* \text{Im}(L) + 2T_* r \text{Im}(\mathcal{J}) = 0 \tag{S67}$$

For any value of r , one solution of this equation is $T_* = 0$ (which is also obviously a solution of Eq. S63). For $T_* \neq 0$ and $\text{Im}(\mathcal{J}) \neq 0$ we have

$$r = \frac{T_*^2 \text{Im}(\mathcal{J}^2 - \lambda_0^2) + 2\pi T_* \text{Im}(L)}{2T_* \text{Im}(\mathcal{J})} = \frac{T_*(\mathcal{J}_r \mathcal{J}_i - \lambda_r \lambda_i) + \pi L_i}{\mathcal{J}_i} \quad (\text{S68})$$

where $\mathcal{J} = \mathcal{J}_r + i\mathcal{J}_i$, $\lambda_0 = \lambda_r + i\lambda_i$, and $L = L_r + iL_i$. Inserting this into the real part of Eq. S66 gives:

$$T_*^2 \text{Re}(\lambda_0^2 - \mathcal{J}^2) - 2\pi T_* \text{Re}(L) + 2T_* r \text{Re}(\mathcal{J}) + \pi^2 - r^2 = 0 \quad (\text{S69})$$

$$\frac{(\mathcal{J}_i^2 - \lambda_i^2)(\mathcal{J}_i^2 + \lambda_r^2)}{\mathcal{J}_i^2} T_*^2 + 2\pi \left(\frac{L_i \lambda_r \lambda_i}{\mathcal{J}_i^2} - L_r \right) T_* + \pi^2 \left(1 - \frac{L_i^2}{\mathcal{J}_i^2} \right) = 0 \quad (\text{S70})$$

$$(\mathcal{J}_i^2 - \lambda_i^2)(\mathcal{J}_i^2 + \lambda_r^2) T_*^2 + 2\pi (L_i \lambda_r \lambda_i - \mathcal{J}_i^2 L_r) T_* + \pi^2 (\mathcal{J}_i^2 - L_i^2) = 0 \quad (\text{S71})$$

This is a quadratic equation for T_* which we write as

$$aT_*^2 + bT_* + c = 0 \quad (\text{S72})$$

with a, b, c all real numbers. Its two solutions

$$T_* = T_{\pm} = \frac{-b \pm \sqrt{b^2 - 4ac}}{2a} \quad (\text{S73})$$

are real for $b^2 > 4ac$, a condition that corresponds to

$$(L_i \lambda_r \lambda_i - \mathcal{J}_i^2 L_r)^2 > (\mathcal{J}_i^2 - \lambda_i^2)(\mathcal{J}_i^2 + \lambda_r^2)(\mathcal{J}_i^2 - L_i^2) \quad (\text{S74})$$

Thus, (B) is satisfied for $T_* = T_{\pm}$ (together with the constraint given by Eq. S74). To produce SSGG, a loop must also satisfy (A), which amounts to the requirement that either $T_{\text{ad}} < T_+ < T_c$ or $T_{\text{ad}} < T_- < T_c$. These two conditions define the range of the five parameters $\mathcal{J}_i, \lambda_r, \lambda_i, L_r, L_i$ over which SSGG occurs (note that \mathcal{J}_r does not appear in any of these expressions).

This range is shown in Fig. S9, from which it is clear that SSGG can be produced by a wide range of simple loops.

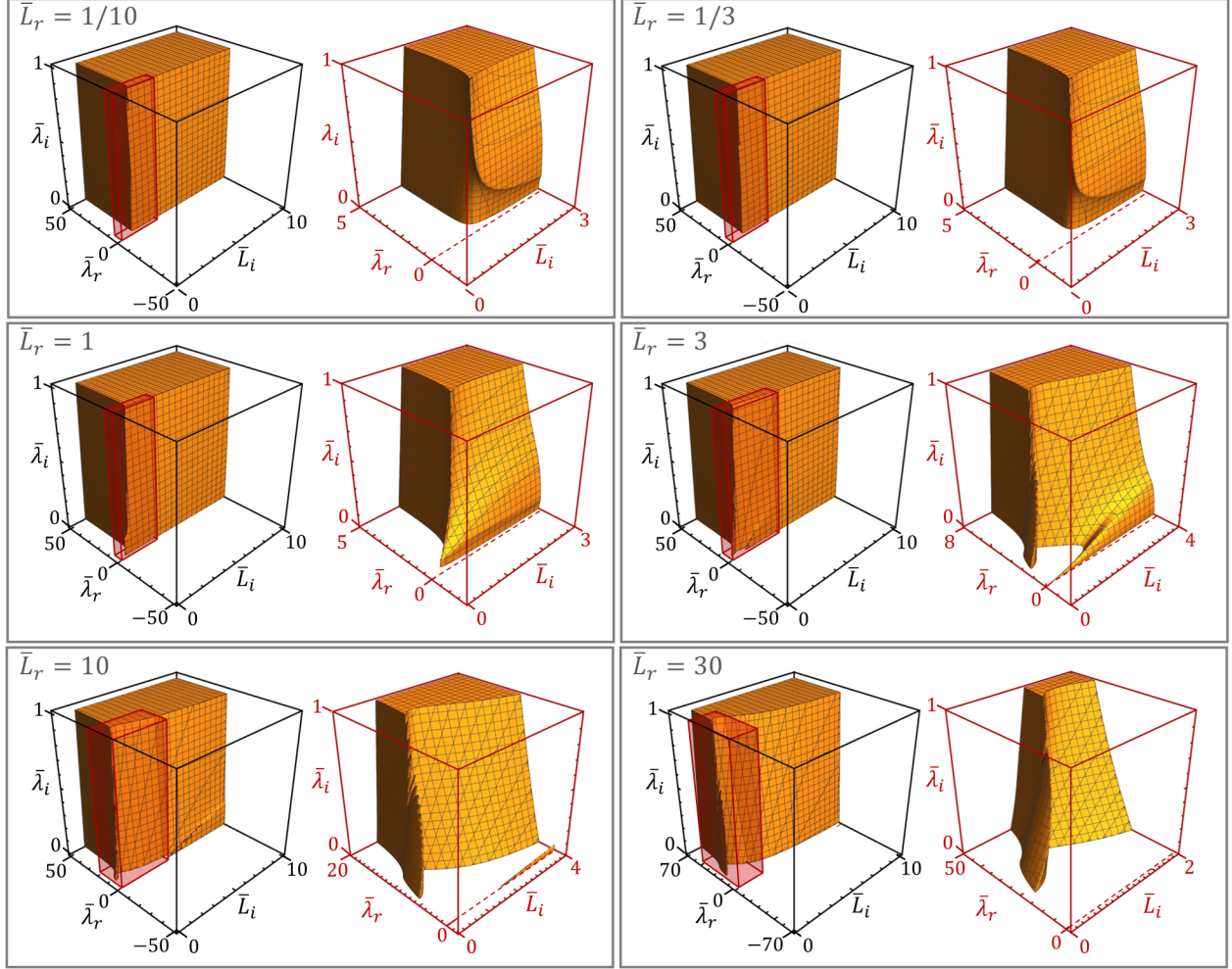


Fig. S9: The “simple” loops that result in SSGG. The orange regions correspond to the range of parameters $\bar{\lambda}_r, \bar{\lambda}_i, \bar{L}_r, \bar{L}_i$ (where an overbar indicates normalization by $|\mathcal{T}_i|$) that can produce SSGG. Each panel corresponds to a different value of \bar{L}_r . The range of $\bar{\lambda}_i$ shown in the plot is $[0,1)$ which is the full range of values that satisfy Condition (3). In each panel, the righthand plot shows a magnified view of the region shown as a red box in the lefthand plot.

As mentioned above, the region shown in Fig. S9 represents only a subset of the loops that realize SSGG, as it does not include loops for which $\text{Im}[\phi(T)]$ does not intersect the bottom boundary of Γ , but does intersect the other boundaries. These additional loops can be identified by repeating the same approach as above. This results in a quartic polynomial equation for T_* (rather than quadratic as in Eq. S71), and hence more cumbersome expressions. It would nevertheless be straightforward to add these solutions to the region shown in Fig. S9.

§8.4 SSGG with a class of non-simple loops

For a family of control loops without an analytic solution, the range of parameters satisfying Condition (4) can be identified by solving Eq. 1 numerically. Here, we consider a family of loops

that may be regarded as representative of smooth (but non-simple) loops. They are qualitatively similar to the loop used in main text Fig. 5, and are given by

$$H(s) = \vec{B}(s) \cdot \vec{\sigma} + \mathcal{I}\mathbb{1}_2 \quad (\text{S75})$$

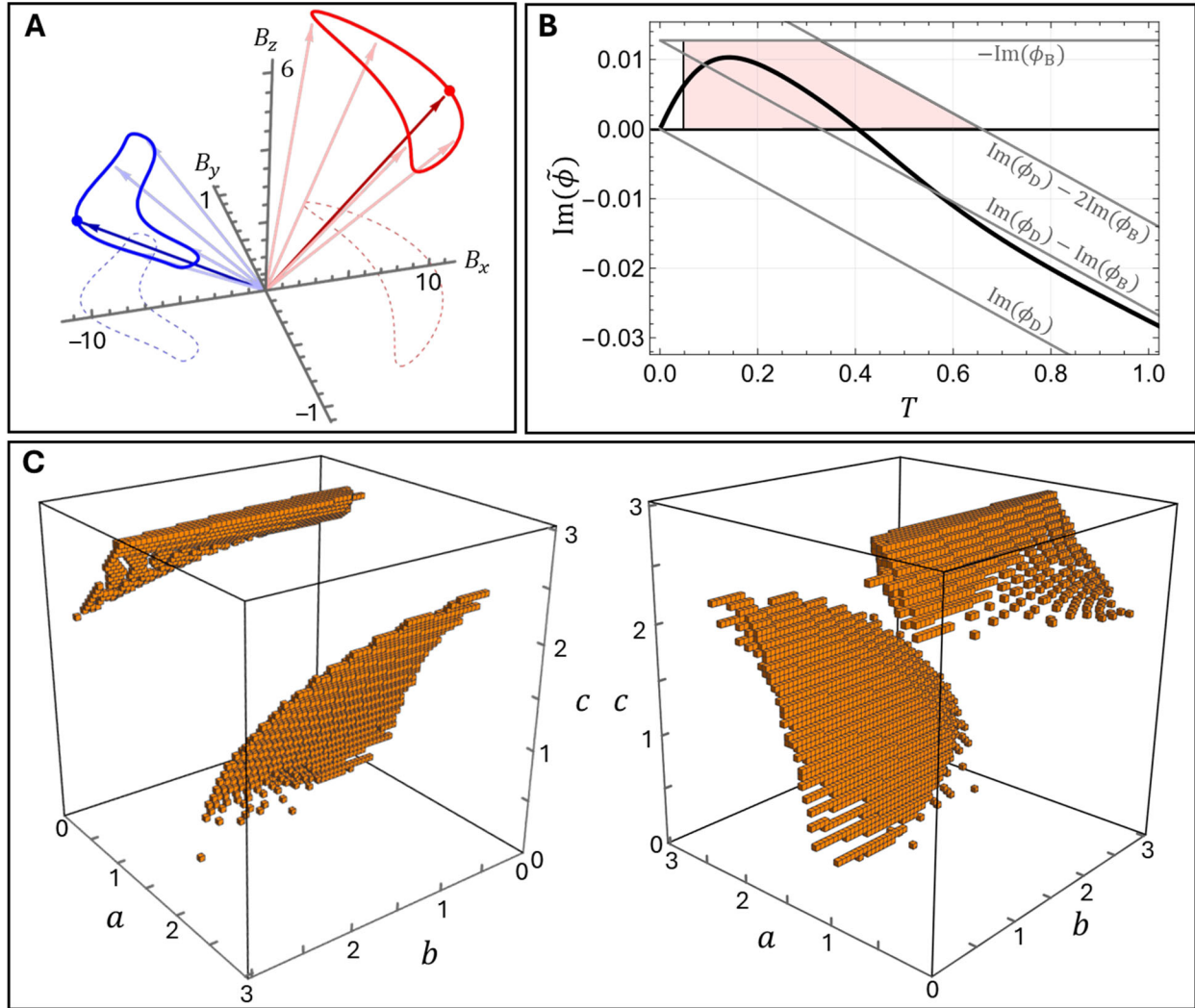


Fig. S10: Non-simple loops and SSGG. **(A)** The loop shape parameterized by Eq. S76 with $(a, b, c) = (1.7, 0.4, 1.3)$. The red and blue curves are $\text{Re}[\vec{B}(s)]$ and $\text{Im}[\vec{B}(s)]$, respectively. The dashed curves show their projection on the B_x - B_y plane. The circles indicate the start and stop of the loop, i.e., $\vec{B}(s = 0, 1)$. **(B)** Black curve: $\text{Im}[\tilde{\phi}(T)]$ for the loop with $(a, b, c) = (0.6, 0.6, 2.7)$. The region Γ is defined as in Fig. S8 ($T_{\text{ad}} = 0.047$ for these parameters). **(C)** Orange: the values of (a, b, c) that produce SSGG. The two panels show different views of the same results.

with

$$\begin{aligned}
B_x(s) &= a \left[4 + \cos(2\pi s) + \cos(4\pi s) - i \left(4 + \cos(2\pi s) + \frac{4}{5} \cos(4\pi s) + \frac{3}{10} \cos(8\pi s) \right) \right] \\
B_y(s) &= b \left[2\sin(2\pi s) + \frac{3i}{2} \left(\frac{1}{5} + \sin(2\pi s) \right) \right] \\
B_z(s) &= c \left[4 + \frac{1}{6} (\sin(2\pi s) - \cos(4\pi s)) + i \left(2 + \frac{1}{7} \sin(2\pi s) - \frac{1}{7} \cos(4\pi s) \right) \right] \\
\mathcal{T} &= 20 - 5i
\end{aligned} \tag{S76}$$

Here a, b, c are the parameters used to vary the loop's shape. An example of one such loop is shown in Fig. S10A.

It is straightforward to solve Eq. 1 numerically for loops with various a, b, c . A typical example of $\text{Im}[\tilde{\phi}(T)]$ resulting from one such solution is shown in Fig. S10B. In this particular case, $\text{Im}[\tilde{\phi}(T)]$ is within Γ for $0.047 < T < 0.41$, and so produces SSGG over this range of s .

Figure S10C shows the result of performing this analysis for values of (a, b, c) ranging from 0.05 to 3 in increments of 0.05. Each value of (a, b, c) that satisfies Conditions (1 – 4) (and hence, for which $\text{Im}[\tilde{\phi}(T)]$ passes through Γ) is represented by an orange block in the figure. As with the simple loops considered in §8.3, SSGG occurs over a substantial range of the loop parameters.

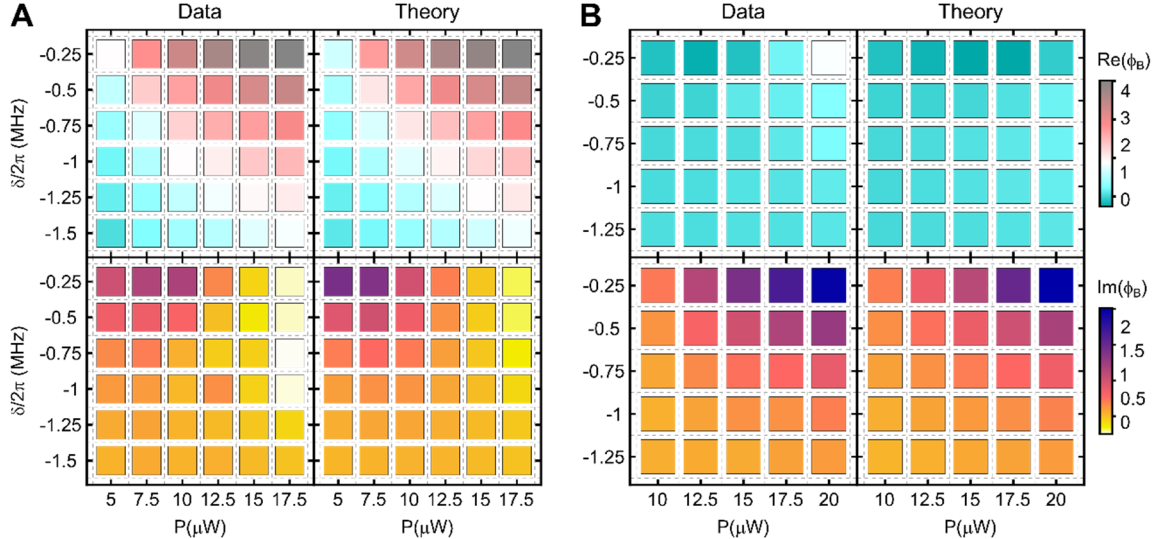


Figure S11: The geometric phase for additional control loops. **(A)** The same parameters as main text Fig. 3C, except that $\eta/2\pi = -20$ Hz. **(B)** The same parameters as main text Fig. 3C, except that $\eta/2\pi = -90$ Hz. The color scale applies to both (A) and (B).

§9 Extended data

This section presents additional measurements that use different types of control loops and different mechanical modes.

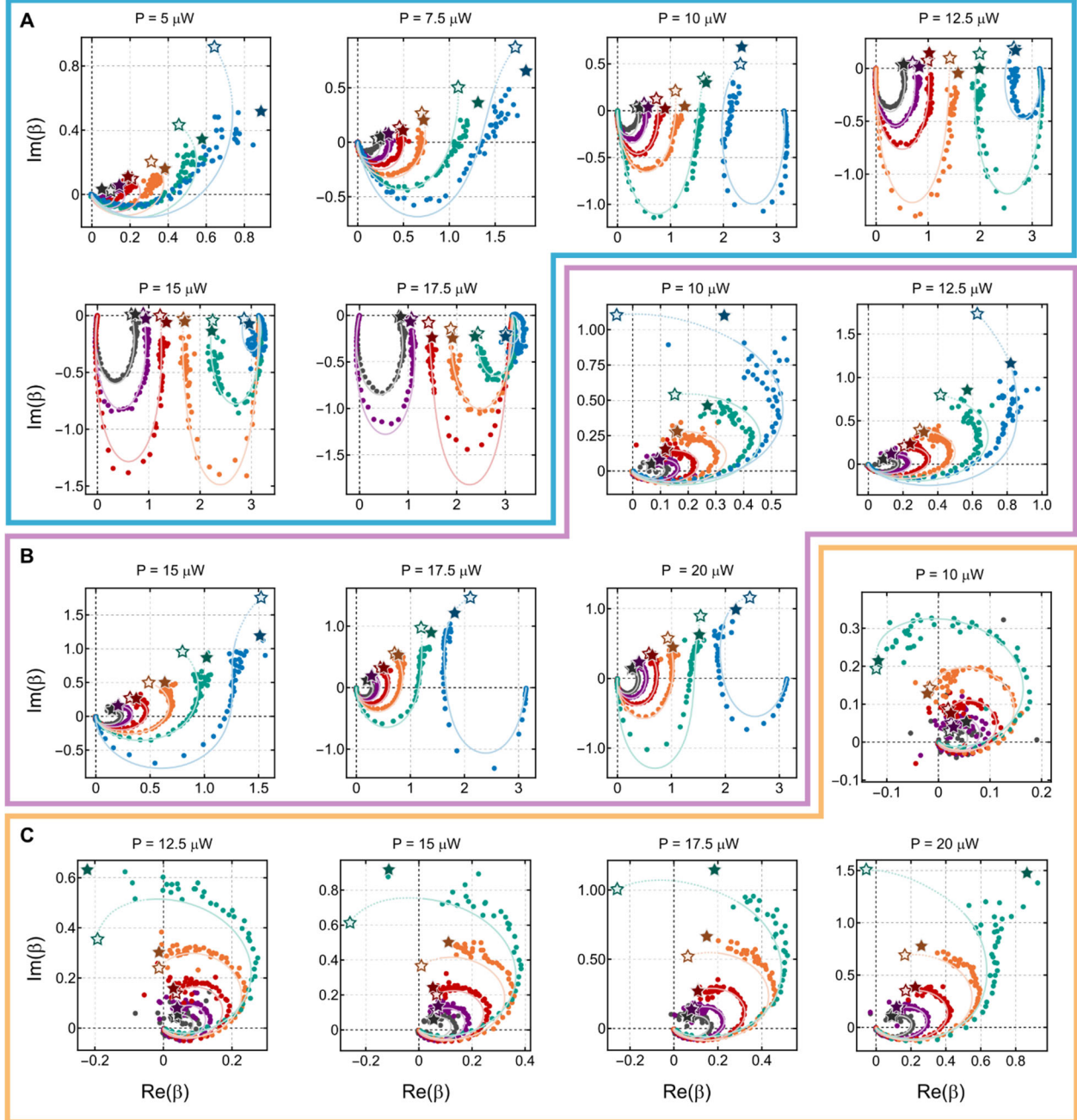


Figure S12: Parametric plots of $\beta(T)$ for all “simple” loops, i.e. for those defined by $\theta_{12}(t) = \pm 2\pi t/T$. **(A)** The data corresponding to Fig. S11A (for which $\eta/2\pi = -20$ Hz). **(B)** The data corresponding to main text Fig. 3C (for which $\eta/2\pi = -50$ Hz). **(C)** The data corresponding to Fig. S11B (for which $\eta/2\pi = -90$ Hz). For every measurement for which the fit to $Re(\alpha)$ returns $n = 1$, we have added π to all data points in $\beta(T)$ as described in §5.1 and Fig. S6.

§9.1 Additional measurements using “simple” control loops

In addition to the measurements presented in main text Fig. 3C (for which $\eta/2\pi = -50$), we have performed similar measurements over the (P, δ) plane for $\eta/2\pi = -90$ Hz and $\eta/2\pi = -20$ Hz. As in Fig. 3C, for each P, δ, η , we measure $\beta(T)$ and $\alpha(T)$, and fit the data at large T to extract the asymptote (i.e., the complex geometric phase ϕ_B) as detailed in §5.

Figure S11 shows the geometric phases extracted from these measurements, along with the predicted values of ϕ_B . We note that some loops in Fig. S11A have almost entirely real ϕ_B , and that some loops in Fig. S11B have almost entirely imaginary ϕ_B .

Additionally, Fig. S12 shows $\beta(T)$ as a function of (P, δ) for $\eta/2\pi = -20$ Hz, -50 Hz, and -90 Hz, similar to Fig. 3, A and B. Note that for every measurement in which the fit to $\text{Re}(\alpha(T))$ gives $n = 1$, we have shifted the entire data set by π to reflect the different choice of branch (see §5.1 and Fig. S6).

§9.2 Control loops with non-constant speed

The data shown in main text Figs. 2 – 4 all use loops in which (P_1, P_2, δ, η) are fixed while the beat note phase is varied so that $\theta_{12}(t) = \pm 2\pi t/T$. However, it is straightforward to realize other types of loops. In this section, we describe measurements using loops in which (P_1, P_2, δ, η) are fixed but the choice of $\theta_{12}(t)$ varies. This provides a demonstration of one of the key features of geometric phase: that it is determined entirely by the shape of \mathcal{C} , and does not depend on the time-dependence used to traverse \mathcal{C} . These measurements used the membrane’s (3,3) and (5,3) modes, and $(P_1, P_2, \Delta/2\pi, \eta/2\pi) = (21 \mu\text{W}, 21 \mu\text{W}, -1.6 \text{ MHz}, -27.5 \text{ Hz})$.

Listed below are five functional forms for $\theta_{12}(t)$ that vary monotonically from 0 to $\pm 2\pi$ as t increases from 0 to T :

- (A) $\theta_{12}(t) = \pm 2\pi(t/T)^2$
- (B) $\theta_{12}(t) = \pm 2\pi\sqrt{t/T}$
- (C) $\theta_{12}(t) = \pm 2\pi \sin(\pi t/2T)$
- (D) $\theta_{12}(t) = \pm 2\pi(6(t/T)^5 - 15(t/T)^4 + 10(t/T)^3)$
- (E) $\theta_{12}(t) = \pm 2\pi(t/T + \sin(\pi t/T)^2/4)$

These functions are plotted in the left column of the corresponding panels of Fig. S13, A to E.

While ϕ_B is predicted to be independent of $\theta_{12}(t)$, the manner in which $\beta(T)$ approaches ϕ_B for large T does depend on $\theta_{12}(t)$. The central and right columns of Fig. S13, A to E demonstrate that $\beta(T)$ indeed changes with $\theta_{12}(t)$, but that for large T it approaches the predicted ϕ_B . This is shown explicitly in Fig. S13F, which plots the asymptotic values of $\beta(T)$ (extracted as in §5) along with the predicted ϕ_B .

§9.3 “Non-simple” control loops

In this section we describe measurements that use “non-simple” control loops, by which we mean loops that involve varying the control tones’ powers and detunings (in addition to θ_{12}).

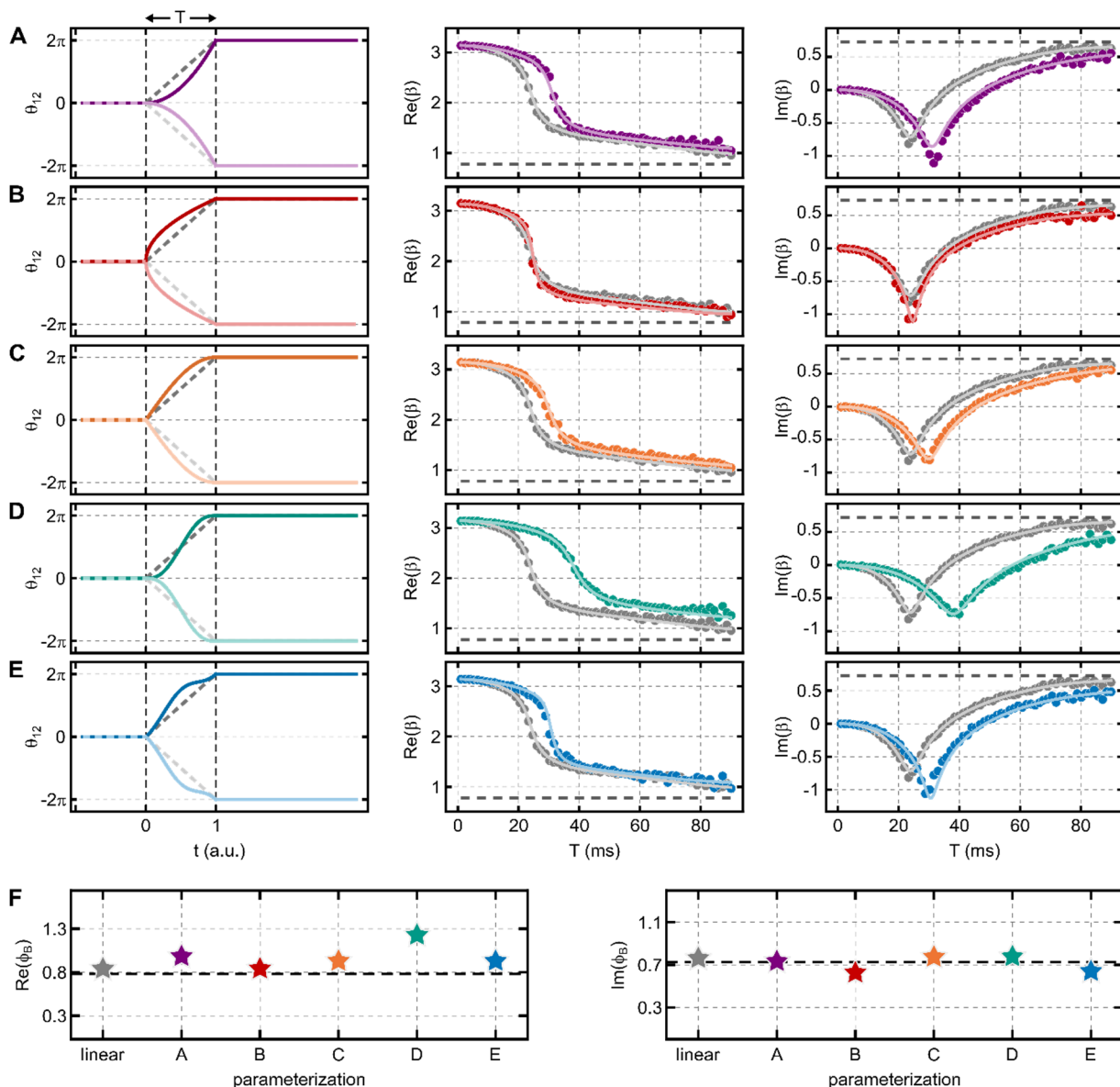


Figure S13: Control loops with various $\theta_{12}(t)$. (A-E) Left column: the five $\theta_{12}(t)$ described in the text (solid). For comparison, the dashed line shows the “linear ramp” $\theta_{12}(t) = \pm 2\pi t/T$ (which is used for the measurements shown in main text Fig. 3). Center column: real part of $\beta(T)$ measured for the corresponding $\theta_{12}(t)$ (colored circles) along with no-free-parameters simulations (colored lines). The dashed line shows the predicted ϕ_B . For comparison, the results for the linear ramp are shown in gray (circles: data, curves: simulation). Right column: the same as the center column, but showing the imaginary part of $\beta(T)$. (F) The real (left) and imaginary (right) components of ϕ_B , extracted from asymptotic fits to $\beta(T)$ for each $\theta_{12}(t)$. The horizontal axis indicates the various $\theta_{12}(t)$. Dashed line: predicted value. These measurements used the membrane’s (3,3) and (5,3) modes, and $(P_1, P_2, \Delta/2\pi, \eta/2\pi) = (21 \mu\text{W}, 21 \mu\text{W}, -1.6 \text{ MHz}, -27.5 \text{ Hz})$.

For these measurements, we modify the setup shown in Fig. S1 to vary δ and P_2 (in addition to θ_{12}) in real time. Control loops realized in this way can be parameterized as: $\vec{X}(s) = (P_1, P_2(s), \delta(s), \eta, \theta_{12}(s))$. Note that for all three of the $\vec{X}(s)$ described here, one mode has lower damping during the entire loop, so that the adiabatic theorem applies for large T .

The first set of non-simple loops that we study are of the form:

$$\vec{X}_1(s) = \left(P_1, P_{2,\text{start}} + P_a \sin(2\pi s), \frac{\delta_{\min} + \delta_{\max}}{2} + \frac{\delta_{\min} - \delta_{\max}}{2} \cos(2\pi s), \eta, 2\pi s \right)$$

where $s = \pm t/T$, $t \in [0, T]$, and the loop parameters are: $P_1 = 15 \mu\text{W}$, $\eta/2\pi = -50 \text{ Hz}$, $P_{2,\text{start}} = 15 \mu\text{W}$, $P_a = 5 \mu\text{W}$, and $\delta_{\min}/2\pi = -1.5 \text{ MHz}$.

Loops with $\delta_{\max}/2\pi = -1.5, -1.25, -1.0, -0.75, -0.5, -0.25 \text{ MHz}$ are illustrated in Fig. S14A. Measurements using these loops were carried out in the manner described in the main text, i.e., traversing each loop both “forward” and “backward” (corresponding to the choice of sign for $s(t)$) and taking the difference of the accumulated phases β for a range of T . These measurements were made using the membrane modes (3,3) and (5,2), and are shown in Fig. S14B.

The second set of non-simple loops are of the form:

$$\vec{X}_2(s) = \left(P_1, P_{2,\text{start}} + P_a \sin(2\pi s), \frac{\delta_{\min} + \delta_{\max}}{2} + \frac{\delta_{\min} - \delta_{\max}}{2} \cos(2\pi s), \eta, \theta_{12,\text{max}} \sin^2(\pi s) \right)$$

where $s = \pm t/T$, $t \in [0, T]$, and the loop parameters are: $P_1 = 15 \mu\text{W}$, $\eta/2\pi = -50 \text{ Hz}$, $P_{2,\text{start}} = 15 \mu\text{W}$, $P_a = 10 \mu\text{W}$, $\delta_{\min}/2\pi = -1.5 \text{ MHz}$, and $\delta_{\max}/2\pi = -0.25 \text{ MHz}$.

These loops differ qualitatively from the ones described by \vec{X}_1 in that θ_{12} is not “wrapped” by 2π in completing the loop. Loops with $\theta_{12,\text{max}} = (0, 2\pi/5, 4\pi/5, 6\pi/5, 8\pi/5, 2\pi)$ are illustrated in Fig. S14C. Measurements using these loops were carried out in the same fashion (and using the same modes) as for the \vec{X}_1 loops, and are shown in Fig. S14D.

The third set of non-simple loops are of the form:

$$\vec{X}_3(s) = \left(P_1, P_{2,\text{start}} + P_{2,a} \left| \sin(\pi s) + \frac{1}{4} \sin^2(2\pi s) \right|, \delta, \eta, \theta_{12,a} \sin \left[2\pi s + \frac{1}{2} \sin(2\pi s) \right] \right)$$

where $s = \pm t/T$, $t \in [0, T]$, and the loop parameters are: $P_1 = 21 \mu\text{W}$, $P_{2,\text{start}} = 5 \mu\text{W}$, $P_{2,a} = 22 \mu\text{W}$, $\delta/2\pi = -0.95 \text{ MHz}$, and $\eta/2\pi = -30 \text{ Hz}$. This is the form of the loop used as \mathcal{C}_{amp} in the demonstration of SSGG (Fig 5), and also uses the third control tone described in Fig. 5A. Loops with $\theta_{12,a} = (\pi/6, \pi/3, \pi/2, 2\pi/3, 5\pi/6, \pi)$ are illustrated in Fig. S14E. Measurements using these loops carried out in the same fashion as for the \vec{X}_1 loops (but using the membrane

modes (3,3) and (5,3)) are shown in Fig. S14F.

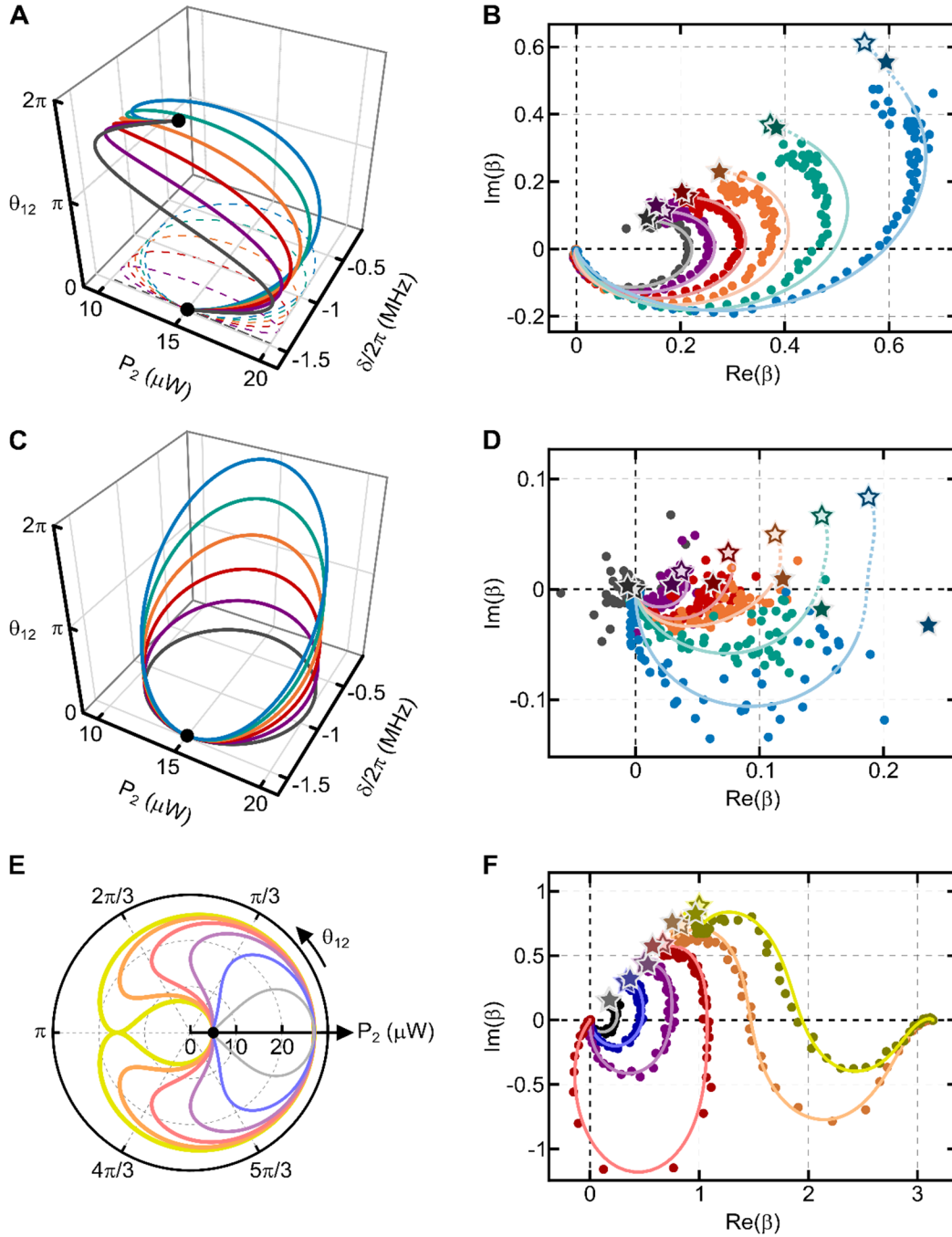


Figure S14: Non-simple control loops. **(A)** Loops of the form \vec{X}_1 , plotted in the 3D space of the parameters θ_{12}, P_2, δ . The solid lines are the actual loop, and the dashed lines show the loop projected onto the (P_2, δ) plane. Black dots are the start/stop point. **(B)** β and ϕ_B for the loops in (A). Circles: measurements of β . Curves: predicted β (solid for the range of T corresponding to the data; dashed for T beyond the measured range). Solid stars: ϕ_B extracted from fitting the $\beta(T)$ for large T . Open stars: predicted ϕ_B . The colors in (B) correspond to the loops in (A). **(C)** Loops of the form \vec{X}_2 . **(D)** β and ϕ_B for the loops in (C). **(E)** Loops of the form \vec{X}_3 . **(F)** β and ϕ_B for the loops in (E).

§9.4 Measurements using a different mechanical mode

The measurements presented in Figs. 2 – 4 (and Figs S4, S5, S11, S12, S14 B and D) used the membrane's (3,3) and (5,2) normal modes. In contrast the measurements in Fig. 5 (and Fig. S12, S13, S14F, S15, S16) used the (3,3) and (5,3) normal modes.

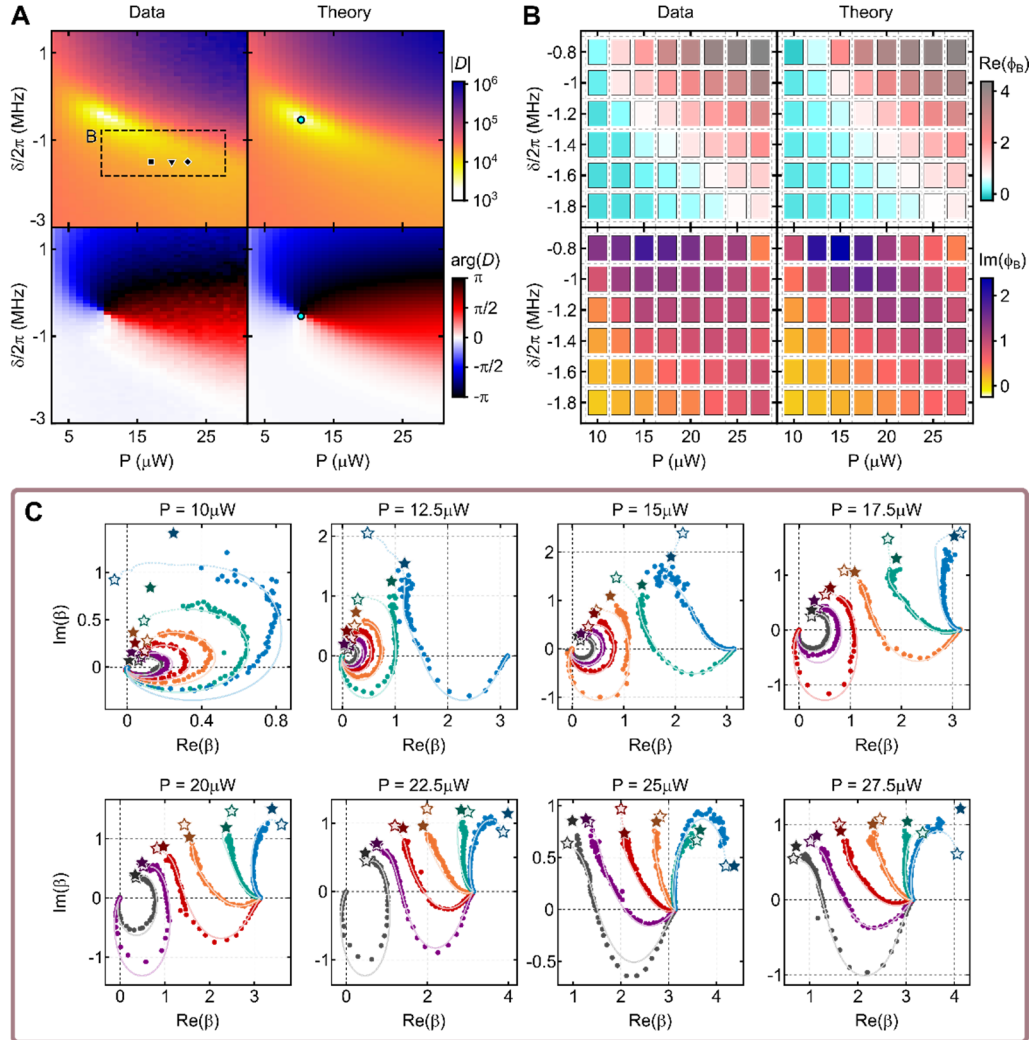


Figure S15: Measurements using the membrane's (3,3) and (5,3) modes. **(A)** Absolute value and argument of the complex discriminant D as a function of the laser power P and detuning δ for $\eta/2\pi = -27.5$ Hz (similar to main text Fig. 1D). The square, triangle, and diamond show the parameters used for the measurements described in Fig. S16. **(B)** Left: geometric phase ϕ_B extracted from fits to $\beta(T)$ for control loops with P , δ drawn from the dashed box shown in (A). Right: predicted ϕ_B (similar to main text Fig. 3C). **(C)** Parametric plots of $\beta(T)$ for all the measurements shown in (B) (similar to main text Fig. 3, A and B).

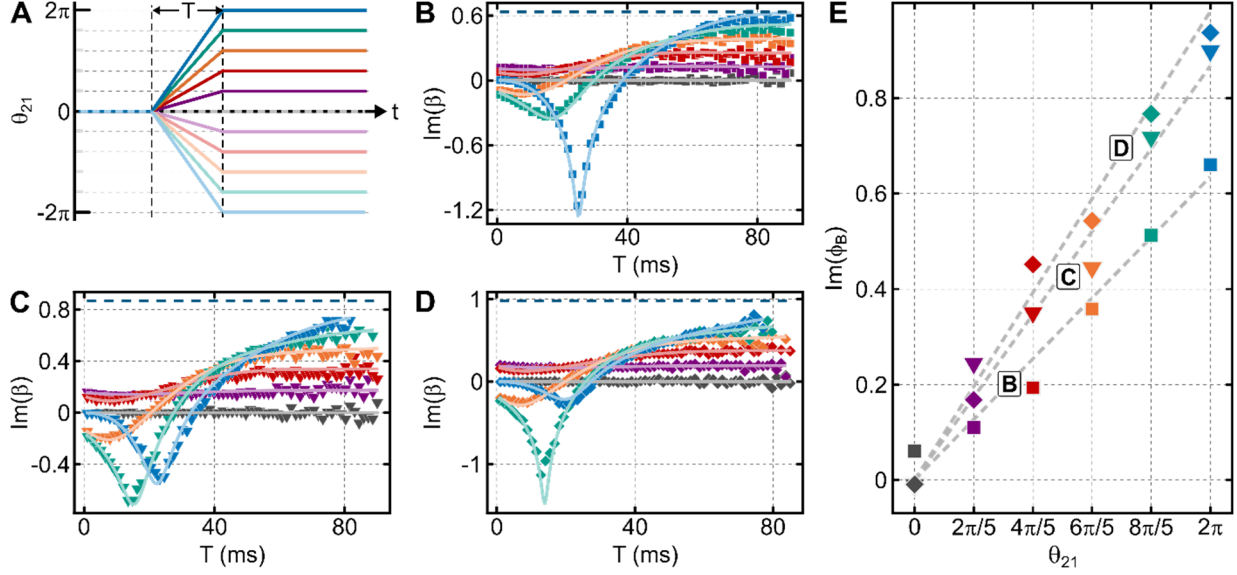


Figure S16: Measurements of open control paths using the membrane’s (3,3) and (5,3) modes. **(A)** Control paths with $\theta_{12}(t) = \pm(N/5)2\pi t/T$ (where $N = 0,1,2,3,4,5$) and fixed $P_1 = P_2 = P, \delta, \eta$ (similar to main text Fig. 4). **(B to D)** Measurements of $\beta(T)$ (circles) for the control paths from **(A)** with $\delta/2\pi = -1.5$ MHz and $\eta/2\pi = -27.5$ Hz for **(B)** to **(D)**, and with $P = (17 \mu W, 20 \mu W, 23 \mu W)$ for **(B)**, **(C)**, and **(D)** respectively (these are the points marked as the square, triangle, and diamond respectively in Fig. S15A). **(E)** The value of $Im(\phi_B)$ determined from each data set in **(B – D)** as a function of N .

To illustrate that the phenomena studied here are generic (rather than specific to a particular pair of modes), here we describe measurements that are analogous to those in main text Figs. 2 – 4, but which use the (3,3) and (5,3) normal modes.

The parameters of the (5,3) mode are given in Table S1. To couple the (3,3) and (5,3) modes, we redefine the control tones’ common and differential detunings: $\Delta_1 = -\omega_1^{(0)} + \delta$ and $\Delta_2 = -\omega_3^{(0)} + \delta + \eta$ such that $(\omega_3^{(0)} - \omega_1^{(0)}) - (\Delta_1 - \Delta_2) = \eta$.

Figure S15A shows measurements of these modes’ discriminant $D = (\lambda_+ - \lambda_-)^2$ as a function of (P, δ) . As in main text Fig. 1C, the eigenvalues λ_{\pm} of this coupled system are determined from measurements of the mechanical susceptibility. Also shown in Fig. S15A is a fit to $D(\delta, P)$ as described in §3.

The left-hand column of Fig. S15B shows measurements of ϕ_B for “simple” control loops (i.e., with $\theta_{12}(t) = \pm 2\pi t/T$) for values of (P, δ) lying in the dashed rectangle of Fig. S15A. The right-hand column shows the calculated values of ϕ_B for each of these loops.

Figure S15C shows parametric plots of $\beta(T)$ for each of these loops. The solid star shows the value of ϕ_B determined by fitting $\beta(T)$ for large T (as described in §5.2), and the hollow star shows the calculated value of ϕ_B .

Figure S16 shows measurements of $Im(\phi_B)$ for control paths that are not closed loops (similar to main text Fig. 4).

-
- ⁵⁴ H. Xu, L. Jiang, A. A. Clerk, J. G. E. Harris, Nonreciprocal control and cooling of phonon modes in an optomechanical system. *Nature* **568**, 65 – 69 (2019).
- ⁵⁵ L. Jiang. Nonreciprocal dynamics in a cryogenic optomechanical system. Ph.D. thesis, Yale University (2020).
- ²³ Y.S.S. Patil, J. Höller, P.A. Henry, C. Guria, Y. Zhang, L. Jiang, N. Kralj, N. Read, J.G.E. Harris, Measuring the knot of non-Hermitian degeneracies and non-commuting braids. *Nature* **607**, 271–275 (2022).
- ⁴⁴ M. Aspelmeyer, T. J. Kippenberg, F. Marquardt, Cavity optomechanics. *Reviews of Modern Physics* **86**, 1391 – 1452 (2014).
- ⁴² G. Nenciu, G. Rasche, On the adiabatic theorem for nonself-adjoint Hamiltonians. *Journal of Physics A* **25**, 5741 – 5751 (1992).
- ² M. V. Berry, Quantal phase factors accompanying adiabatic changes. *Proceedings of the Royal Society of London Series A* **392**, 45 – 57 (1984).
- ³² J. C. Garrison, E. M. Wright, Complex geometrical phases for dissipative systems. *Physics Letters A* **128**, 177 – 181 (1988).
- ⁵⁶ A. I. Nestorov, F. Aceves de la Cruz, Complex magnetic monopoles, geometric phases and quantum evolution in the vicinity of diabolic and exceptional points. *Journal of Physics A* **41**, 485304 (2008).
- ⁵⁷ R. Resta, Manifestations of Berry’s phase in molecules and condensed matter. *Journal of Physics: Condensed Matter* **12**, R107 – R143 (2000).